Spring 3-28-2019

Compact Optical Frequency Standards for Future Applications Beyond the Laboratory

Kyle Martin
University of New Mexico - Main Campus

Kyle William Martin

Candidate

Physics and Astronomy

Department

This dissertation is approved, and it is acceptable in quality and form for publication:

Approved by the Dissertation Committee:

Francisco Elohim Becerra-Chavez , Chairperson

Ivan Deutsch

Nathan Lemke

Andrew J. Metcalf

Compact Optical Frequency Standards for Future Applications Beyond the Laboratory

by

Kyle W. Martin

M.S., University of New Mexico, 2012
B.S., University of New Mexico, 2010

DISSERTATION

Submitted in Partial Fulfillment of the
Requirements for the Degree of

Doctorate of Philosophy
Physics

The University of New Mexico

Albuquerque, New Mexico

May, 2019

Dedication

To my family, for their loving support and encouragement.

Acknowledgments

I have met many people whom have aided my research direction and efforts whether professionally or personally. I would like to first thank Dr. Nathan Lemke, along with others, he encouraged me to finish my PhD. He also became my advisor at AFRL directing the research and giving helpful advice when needed. In no particular order I need to thank Dr. Gretchen Phelps, Dr. Benjamin Stuhl, Jordan Armstrong, and Dr. Matthew Bigelow. These colleges helped me with my research goals, and also allowed me to witness different approaches to solving similar problems. I also need to thank Dr. Francisco Elohim Becerra-Chavez, my UNM advisor. He graciously took upon himself the responsibility of my dissertation committee chair. I also need to thank my entire dissertation committee, the remaining members: Dr. Ivan Deutsch and Dr. Andrew J. (A.J.) Metcalf.

I would to thank Dr. Brian Kasch, Dr. Matthew Squires, Dr. Spencer Olson, and Dr. Maxwell Gregoire for their many useful discussions, mostly on subject. I would also like to thank Applied Technology Associates for assisting me in my educational goals.

Finally I need to thank my family. My brother Dr. Paul Martin for his useful conversations about our research projects, he shares with me the pain/joy of being an experimental physicist. My parents for their loving support. My beautiful wife Allison for her encouragement, love, support and for reading this entire dissertation, she truly is a wonderful partner. Also my children, Joshua and Samuel. They remind me every day that learning is a wonderful thing and that the pursuit of knowledge is something that should be tackled each day with vigor.

Compact Optical Frequency Standards for Future Applications Beyond the Laboratory

by

Kyle W. Martin

M.S., University of New Mexico, 2012
B.S., University of New Mexico, 2010

PhD, Physics, University of New Mexico, 2019

Abstract

Atomic clocks provide one of the fundamental building blocks upon which modern telecommunications systems are constructed. Since the invention of the frequency comb in the early 2000s, laboratory frequency standards have quickly outpaced their compact counterparts. Compact clocks, however, have continued to leverage microwave transitions not yet exploring the advantages of an optical atomic clock. With the recent development of robust frequency combs compact optical clocks can now be realized. In this dissertation two atomic species are investigated for a compact atomic frequency standards. Both of these clocks are in different development stages but offer unique advantages.

The optical rubidium atomic frequency standard relies on a two-photon transition in rubidium. This dissertation details the design necessary to achieve best clock stabilities to date leveraging this two-photon transition. Calculations and measurements of required environmental instabilities to reach stabilities of 1×10^{-15} at one

day are included. The hardest environmental parameters to suppress are the self collisional shift and the ac-Stark shift. A new approach to reduce ac-Stark shift is discussed as well as a robust thermal design which achieved necessary temperature stabilities.

Calcium provides a much narrower transition then the two-photon rubidium for which to build a clock. A calcium vapor cell could revolutionize experimentation with this species. This dissertation describes a first ever closed calcium vapor cell. I also describe a method for continuous operation of this vapor cell without replenishing calcium or cleaning the optical windows.

The optical rubidium atomic frequency standard has shown fractional frequency instabilities of $4 \times 10^{-13}/\sqrt{\tau(s)}$ for τ from 1 to 10,000 seconds, with potential to achieve instabilities of less then 1×10^{-13} at one second and less then 4×10^{-15} at one day. The calcium clock is still in vapor cell development stages, showing some promise for future fully realized calcium clock based on vapor cell technologies.

Contents

List of Figures

List of Tables

Glossary

AFRL	Air Force Research Labs
UNM	University of New Mexico
NIST	National Institute of Standards and Technology
REP	repetition rate
SNR	signal to noise ratio
LO	local oscillator
GNSS	global navigation satellite System
PMT	photo-multiplier tube
RF	Radio Frequency.
CEO	carrier envelope offset
RAFS	rubidium atomic frequency standard
HFS	hyper fine states
SHG	second harmonic generation
O-RAFS	optical rubidium atomic frequency standard
EOM	electro-optic modulator

VOA	variable optical attenuator
ECDL	external cavity diode laser
RIO	Redfern Integrated Optics
SOA	semi-conducting optical amplifier
RAR	rubidium atomic reference
PPLN	periodically pulsed lithium niobate
ISO	optical isolator
PID	proportional, integral, differential lock mechanism
RAM	residual amplitude modulation
EDFA	erbium doped fiber amplifier
ABCD	the ABCD matrices are used for Gaussian beam propagation calculations
Ti:Sapph	titanium doped sapphire laser
ODR	orthogonal distance regression
BBR	blackbody radiation
VBG	volumetric Bragg grating
ALON	Aluminum oxynitride
AOM	acoustic optical modulator

Chapter 1

Introduction

"A physicist is just an atom's way of looking at itself."

—Niels Bohr

Imagine two horizontal lines spaced about a foot apart. This is an atom drawn on a chalkboard. This is not the cartoon rendering with electron dots whizzing around the proton neutron filled nucleus, but a true representation of an atom. A complete two-level system, fully labeled with $h\nu$ representing the required energy of a photon to excite this atom from the ground state. It is this atom that allows precision measurements of magnetic and electric fields, gravitational gradients, accelerations, and much more. It is this atom that, since 1967, defines a second as 9,192,631,770 oscillations of the frequency required in the transition between the hyperfine components of the ground state of Cesium-133 [135]. It is this atom that continues to produce more accurate and precise clocks. Time itself has been proposed to measure even the most elusive physical properties such as dark matter, single gravitons or even slow changes in the physical constants that describe our world. It is amazing that simply measuring the passage of time can be such a powerful scientific tool.

1.1 Measuring Time

"The trouble is, you think you have time."

—Buddha

Humans have a well documented fascination with time. The Mayans and Aztecs developed astronomical calenders that tracked the phases of the moon, solar eclipses and positions of numerous stars. These calenders were essential to recording the histories and cultures of communities as well as developing agriculture. The ancient Egyptians and Chinese scholars developed sundials and water clocks to break a singular day into smaller fractions. Masterful, tower sized mechanical clocks eventually were invented, followed by the Huygens pendulum clock and spring wheel wristwatch, allowing for never before seen timing accuracies of only a few seconds lost every day.

For over two hundred years, mechanical clocks were improved and refined until they were finally replaced in the 1920s with the quartz clock [90, 91]. These clocks would have a short lived timing supremacy. In 1949, National Institute of Standards and Technology (NIST) built the first atomic clock, starting the golden age of atomic clocks [132]. Since the birth of the atomic clock, modern society has become accustomed to the availability of precise timing sources. Advanced timing is paramount to telecommunications networks and banking transactions as well as useful in precision measurement of gravity gradients, magnetic field strengths and tectonic plate motions. In principle, measurement of time is simple. The measurement only requires a stable oscillator and the ability to count the oscillations. However, nothing is completely disconnected from the environment, and stable oscillators quickly become a metrologist's spherical cow: great in theory, not completely true in practice.

1.2 Allan Variance

"A man with one watch knows what time it is. A man with two watches is never sure."

—Segal's Law

The generation of a stable oscillation is critical for precision timing applications. The instantaneous frequency an oscillator is defined as

$$\nu(t) = \nu_0 + \frac{1}{2\pi}\frac{d\phi}{dt}, \tag{1.1}$$

where ν_0 is the nominal frequency and $\phi(t)$ is the signal's phase deviation. The accuracy of a precision oscillator, how well the oscillator produces a desired frequency, is what distinguishes the primary frequency[1] standards from the secondary frequency standards[2]. The precision of the oscillator, how stable the frequency is from cycle to cycle, is often the metric used to compare clocks. Fractional frequency is a measure of how much the clock varies, as a percentage of its own generated frequency. Two clocks with an instability at the 1 Hz level, initially, appear to generate the same stability. However if one clock generates a fundamental frequency at 1 Hz and the other generates it's frequency at 100 THz the clocks precisions are drastically different.

The fractional frequency of a precision oscillator is defined as

$$y(t) = \frac{1}{2\pi\nu_0}\frac{d\phi}{dt}. \tag{1.2}$$

[1]Primary standards, produce a frequency that can be precisely calculated from fundamental physical principles, examples include the cesium fountain [135], strontium lattice and ytterbium lattice [27, 47, 60].

[2]Secondary standards, produce a frequency whose connection to fundamental physics is often more complicated, thus the output frequency is calibrated using a primary standard. Examples include quartz oscillators and the rubidium frequency standard [30]

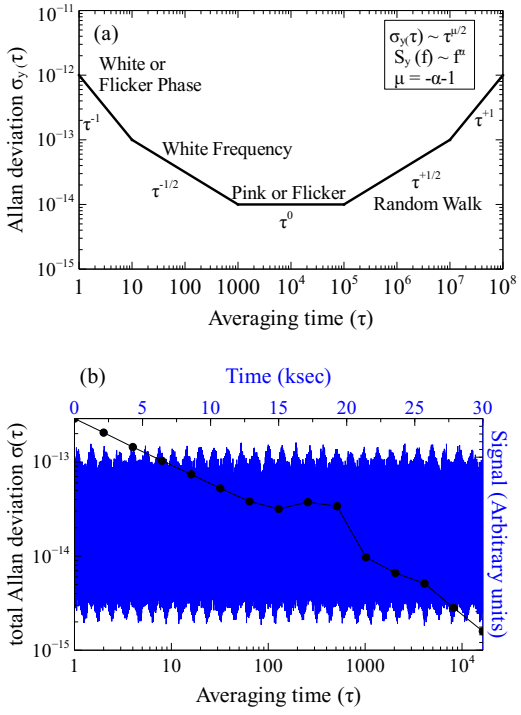

Figure 1.1: The instability of most frequency sources can be modeled with combinations of noise where the spectral density follows a power law, $S_y(f) \propto f^{\alpha}$. The Allan deviation slope, $d\sigma_y/d\tau$, has a characteristic value for specific noise sources, as shown in (a). This figure was originally found in [113]. Shown in (b) is a signal generated with a time varying white noise source, $f = 1$ mHz, as well as the Allan deviation of the generated data. The bump at $\tau = 500$ s could be used to identify and suppress clock instability.

Generic frequency taken at a regular gate window is divided by the average frequency and then normalized (normalization here refers to subtraction of the mean). The standard variance for a normalized fractional frequency data set containing N samples is then,

$$s^2 = \frac{1}{N-1}\sum_{i=1}^{N} y_i^2. \tag{1.3}$$

Typically, deviation from the mean of a generated signal is described by the standard variance. Unfortunately, this analysis is not suitable for analysis of frequency stability for a few reasons. Primarily, the standard variance only compares each measurement

with the mean of the system, inherently biasing the analysis towards white noise sources. For other common noise sources the standard deviation analysis will diverge, most notably pink, flicker, or $1/f$ noise. Secondly, the standard variance has no time dependence. If a generated signal has noise features that oscillate in time, without affecting the mean, this analysis technique would not generate any specific indicators to help an experimentalist identify and suppress the noise source. Rather, the precision at which a clock frequency is generated is characterized with the Allan variance. Leveraging these statistics, the stability of multiple frequency sources can be compared. Introduced in 1966, the Allan variance [4] is better suited to analyze common clock frequency instabilities than the classic variance and has become the standard analysis tool. The definition of the Allan variance presented here follows closely to the work found in [113].

The Allan Variance is defined as

$$\sigma_y^2(\tau) = \frac{1}{2(M-1)} \sum_{i=1}^{M-1} \left[y_{i+1} - y_i\right]^2, \tag{1.4}$$

where y_i is the i^{th} of M fractional frequency elements averaged over a time τ. Since bins of data points are compared to neighbors, time dependent noise frequency fluctuations are readily apparent as the data bin time is varied (see Figure 1.1 (b)). The Allan deviation also distinguishes between noise sources of different colors(see Figure 1.1 (a)).

Although there exist many variations on the simple Allan variance, historically either the Allan variance or the total Allan variance are utilized to analyze stable oscillators. The total Allan variance is given by,

$$\sigma_y^2(\tau) = \frac{1}{2(M-1)} \sum_{i=1}^{M-1} \left[y^*_{i+j+1} - y^*_{i+j}\right]^2. \tag{1.5}$$

The total Allan variance manufactures a larger data set from the measured data points. The measured data of length N is concatenated with reflections about each endpoint generating a new vector y^* of length $3N-2$ (see Figure 1.2).

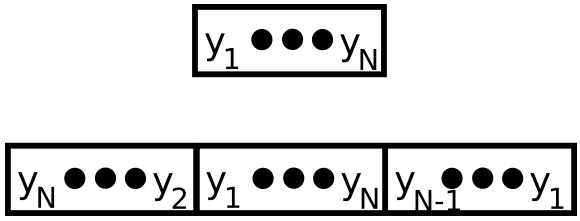

Figure 1.2: Data for the total Allan deviation is generated by mirroring the collected data vector about its endpoints creating a vectors approximately three times the original length. Figure originally found in [113].

1.3 Atomic Clocks

"Nothing exists except atoms and empty space, everything else is opinion."

—Democritus

The first atomic clocks utilized microwave cavities around a cloud of hot atoms or molecules. The atoms act as a frequency detector, feeding back to the local oscillator (LO) to force the LO to maintain a stable frequency. These first microwave clocks were born at the intersection of high frequency radio communications and the atomic age around 1950. However, the invention of the laser provided three new clock architectures to be studied: the *laser cooled microwave clock*, the *optical clock* and the *optical lattice clock* (see Figure 1.3). A sacrifice of simplicity for improved stability results in each clock design. Inclusion of a broadband laser for cooling the atoms to reduce Doppler and collisional effects results in the *laser cooled microwave clock*. Introduction of a narrow linewidth laser for probing the clock state to increase the fundamental frequency of the system as well as the introduction of a frequency comb resulted in the *optical atomic clock*. The choice to sacrifice all simplicity and simultaneously control the thermal environment of the atoms as well as probe the optical clock transition results in the *optical lattice clock*. Although the design is

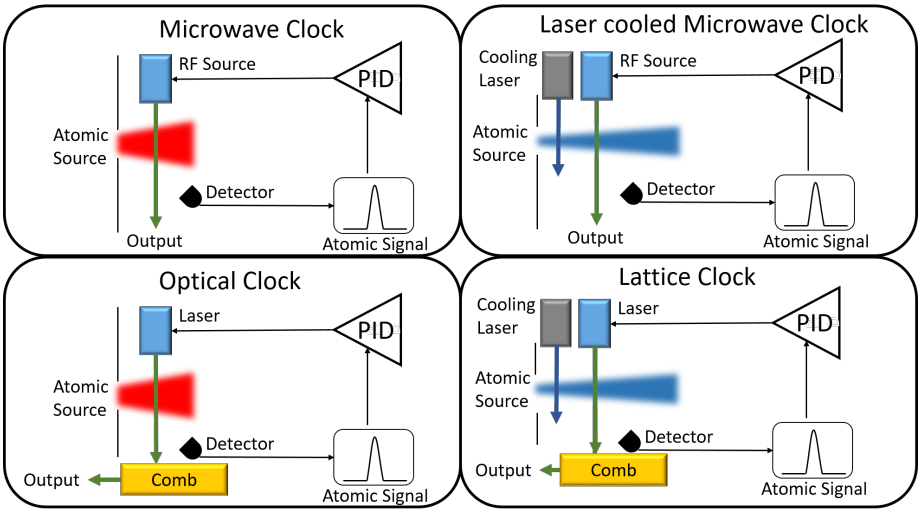

Figure 1.3: Shown above are four classes of atomic clocks: the *microwave clock*, the *optical clock*, the *laser cooled microwave clock* and the *optical lattice clock*. The diagrams give a simple picture of the major components involved briefly described in the text.

different, the final desired goal for all four architectures is to generate a stable output frequency.

Every clock within each class has unique features. An example would be the rubidium atomic frequency standard (RAFS) pictured shown in Figure 1.4. A high quality microwave cavity surrounds the target Rb vapor cell. This cavity is tuned to the hyperfine ground state transition for ^{87}Rb of ≈ 6.835 GHz. If the system was simply this, half the atoms would be in the $F = 2$ state and half would be in the $F = 1$ state with no ability to distinguish the quality of the resonance transition. The atoms in the target cell need to be polarized. A Rb lamp is utilized to generate a broad spectrum of light on resonance with the D1 and D2 transitions. An atomic filter, a vapor cell with ^{85}Rb and a buffer gas, is utilized to filter out the $5S_{1/2}(F = 2) \rightarrow 5P_{3/2,1/2}$ transition. Light from the lamp/filter is then sent to the final ^{87}Rb vapor cell. The remaining lamp light excites the atoms from the $F = 1$ ground state to the $5P$ states. The microwave cavity is tuned to ≈ 6.835 GHz exciting the atoms

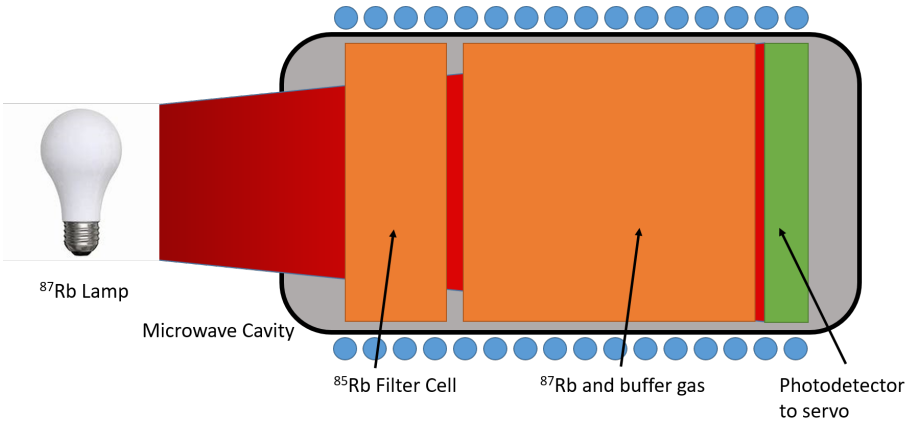

Figure 1.4: Shown above is a simple picture of the rubidium atomic frequency standard. From left to right a ^{87}Rb and a ^{85}Rb filter cell generate light that polarizes the atoms in the final vapor cell. The entire system is integrated inside a microwave cavity. Adapted from [30].

from $F = 1 \rightarrow F = 2$ ground state. At the appropriate tuning of the microwave cavity, less light is transmitted through the cavity as detected by a photodiode [30], (see Figure 1.4) . Alternatively, the lamp/filter could be replaced with a narrowband coherent light source in a pulsed-optically-pumped rubidium clock [95]. Both clocks are fundamentally microwave rubidium clocks but the design is very different.

Probing atoms to generate a stable frequency is a measured gamble. Although the idea of a stable two-level system is achievable, in practice this can require substantial work. The simple hydrogen atom picture soon gets lost while accounting for internal atomic and environmental frequency shifts, as well as the presence of other superfluous states. Each clock design is robust to some of these frequency instabilities, however, precise control over other environmental parameters is required for other instability generators. The best clocks are ones that use the atomic signal as a measure of the instabilities and generate a signal to eliminate them.

1.4 Compact Atomic Clocks

"Anything will lase if you hit it hard enough"

—Arthur L. Schawlow

High stability clocks and oscillators play an integral role in many modern technologies such as navigation and communications [89]. Laboratory-based primary frequency standards, which utilize microwave transitions between atomic hyperfine levels, provide the highest degree of timing accuracy and are used to form international timescales [59, 103, 142]. However, applications beyond timekeeping require clocks that are deployed outside the laboratory setting. One well-known case is that of global navigation satellite systems (GNSS), which employ space-qualified frequency standards aboard satellites in medium earth orbit and/or geosynchronous orbit [89,94]. While portable clocks are typically outpaced by their laboratory counterparts in terms of stability and accuracy, they nonetheless offer very low levels of frequency instabilities; in the case of rubidium atomic frequency standards, clocks are commercially available with a fractional drift rate below 10^{-13}/day and a fractional frequency noise floor less than 10^{-14} [54].

In the photon shot noise limit, clock stability can be described by [28],

$$\sigma_y \approx \frac{1}{Q}\frac{1}{\sqrt{N}}\frac{1}{\sqrt{\tau}} \tag{1.6}$$

where the Q factor is the ratio of atomic linewidth to excitation frequency, $Q = \nu/\delta\nu$, and N is the number of detected photons and τ is the averaging time. While the RAFS clock can have a Q factor as high as 300 million optical transitions offer very large Q factors, larger than 1 billion, and as shown in Equation 1.6 large Q factors reduce clock instability. Optical frequency standards have rapidly surpassed the capabilities of microwave clocks in both stability [21, 67] and systematic uncertainty [33, 70, 100]. Efforts to reduce the size and increase the portability and autonomy

of these systems form an active research area [66, 81, 85, 87, 121, 126]. Of particular interest from the standpoint of deployable clocks is an optical frequency standard that can surpass existing commercial clocks by one factor of 10 in both short- and long-term stability, which translates to an Allan deviation of $\sim 1 \times 10^{-13}$ at 1 s and $\sim 1 \times 10^{-15}$ at 1 day, without significantly increased volume ($\lesssim 10$ L) or power consumption ($\lesssim 20$ W). However, a fully automated, portable, and compact optical atomic clock has yet to be realized. Much of the difficulty in developing compact and environmentally robust optical frequency standards lies with the complicated laser sources and optical systems required for laser cooling and interrogating an atomic sample. Moreover, given the high quality factor (i.e. narrow spectral linewidth) of typical optical clock transitions, laser pre-stabilization to a high-finesse Fabry-Pérot cavity is generally required, which adds significant complexity and volume to the system. Finally, optical frequency combs have, until recently, not been sufficiently compact or robust to warrant an effort toward deployment of an optical clock.

1.4.1 Frequency Combs

A desire for high resolution spectroscopy across a wide breadth of frequencies spanning from the ultraviolet to the infrared coupled with accurate measures of the involved frequencies led to the invention of the frequency comb. Predating combs, precise measurement of optical frequencies was difficult, requiring a harmonic frequency chain, starting with a Cesium fountain clock and generating higher frequencies with non-linear mixing processes [13, 49, 120, 122, 137]. The advent of fully stabilized optical frequency combs in 2000 [44,68,74] was a catalyst for the recent rapid optical clock development. While the operation of na optical frequency standard is independent of a frequency comb, one is necessary in the final design to coherently divide the clock signal for counting with current state of the art radio frequency (RF) electronics, or for cross-comparison of multiple optical clocks.

Consider an infinite train of phase coherent pulses shown in Figure 1.5 (a) which are periodic with periods $T = 1/f_{rep}$. Each pulse envelope has a full width at half maximum of t_{pulse}, and the pulse to pulse phase shift, or carrier envelope offset (CEO), is given by $\Delta\Phi_{CEO}$. The Fourier transform of such a pulse train is shown in Figure 1.5 (b). Single frequency carriers are displayed spaced by f_{rep}, and the envelope defining the breadth of frequencies has a full-width-half-max of $1/t_{pulse}$. Often the pulse train is generated with a femtosecond laser, yielding a frequency grid whose bandwidth is in the optical regime. Extension of this frequency grid back towards dc yields an offset related to the pulse to pulse phase shift, $f_{CEO} = \Delta\Phi_{CEO}\frac{f_{rep}}{2\pi}$. The grid of generated frequencies resembles a comb or *frequency comb*. The frequency of every tooth can be described as $\nu = f_{CEO} + nf_{rep}$, where n is the tooth number. Stabilizing a comb tooth to a generated clock frequency while simultaneously stabilizing f_{CEO} yields f_{rep}, when detected f_{rep} is a coherent down conversion of the clock signal.

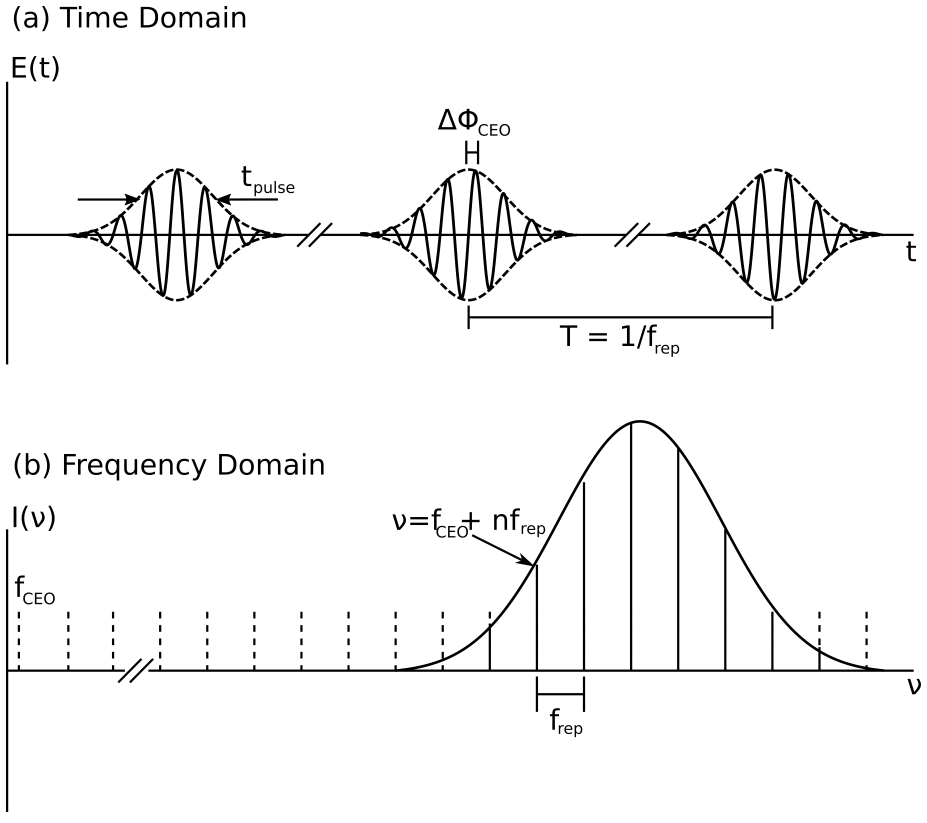

Figure 1.5: A pulse train in the time domain (a) and the resulting Fourier transform (b), described in the text. Figure originally found in [36].

Chapter 2

Two-Photon Transition in Rubidium

The quality of an atomic frequency standard is defined to be the linewidth of the transition divided by the transition frequency, and is directly related to the frequency stability (see Equation 1.6). In an endless pursuit of a more stable oscillator, more narrow transitions and larger transition frequencies are desired. It is these two pursuits that led to the creation of laser cooled microwave clocks and optical clocks, respectively. The simultaneous desire to reduce linewidth and increase the transition frequency led to the relatively new optical lattice clocks [27,47,60]. Compact clocks, however, have yet to leverage these two simple ideas to increase clock stability.

Simply adopting an optical standard, leveraging the increased operational frequency, yields some unfortunate side effects. Doppler broadening occurs in a thermal collection of atoms, as different velocity distributions witness different incident frequencies. Optical lattice clocks employ laser cooling to trap the atoms, cooling them to drastically reduce the atomic velocity distribution. This technique requires multiple lasers, special atomic sources, and ultra high vacuum chambers, and is not currently suitable for a compact clock. Yet another technique to reduce Doppler

broadening is saturated absorption spectroscopy [41, 104, 138]. A strong *pump* beam is incident on the atomic vapor, while a counter-propagating *probe* beam at the same frequency is incident on the same cloud. The beam frequency is modulated and the intensity of the *probe* beam is then measured. Atoms with motion parallel to each beam will absorb detuned light from either the pump or the probe, while atoms moving only perpendicular to beam propagation will be excited by the resonant *pump* beam, leaving a maximum in the *probe* beam detection. This is a velocity selective process, producing a small signal to noise ratio, yet another important parameter in oscillator stability.

Degenerate two-photon spectroscopy [1] [16, 19, 29, 71, 84] provides an alternative method to suppress Doppler effects. The desire to leverage a Doppler free transition, based on existing technology, into a frequency standard with a simple design motivates the interest in two-photon transitions. Employed heavily in the 1970s Doppler free two-photon transitions have been successfully utilized for measuring fine and hyperfine structures [71], Zeeman [20] and Stark [62] splittings as well as hot vapor collisional effects [17, 146]. In particular the $5S_{1/2} \rightarrow 5D_{5/2}$ and $5S_{1/2} \rightarrow 7S_{1/2}$ two-photon transitions in Rb are of interest for optical frequency standards [11, 34, 65, 80, 98, 99, 111]. These transitions leverage existing glass vapor cell technologies, and required lasers could be realized through frequency doubling of existing telecom lasers (1556 nm and 1520 nm respectively) and could be employed in a clock architecture that has the potential to reduce size, weight, power and technical challenges while still maintaining high precision.

Zameroski *et al.* [146] examines the self broadening of each proposed two-photon transition in Rb as well as from various noble gases. The smaller Rb-Rb collisional shift and the narrower natural linewidth make the $5S_{1/2} \rightarrow 5D_{5/2}$ transition in Rb more desirable for a frequency standard, and this chapter focuses on this subject.

[1] Degenerate two photon spectroscopy requires that the two photons used for excitation have the same frequency, oftentime originating from the same source.

2.1 Excitation Rate

Derivation of the excitation rate for a two level atom and a two-photon transition closely follows work presented in [76,130]. Consider a two level atom interacting with a classical field, where the interaction Hamiltonian is the classic dipole $\mathbf{H} = -\mathcal{E} \cdot \mathbf{d}$. The excited and ground state populations can be found through solving the coupled differential equations,

$$\begin{aligned} \left(\frac{\partial^2}{\partial t^2} - i\Delta\frac{\partial}{\partial t} + \frac{\Omega^2}{4}\right) c_g = 0, \\ \left(\frac{\partial^2}{\partial t^2} - i\Delta\frac{\partial}{\partial t} + \frac{\Omega^2}{4}\right) c_e e^{i\omega t} = 0, \end{aligned} \tag{2.1}$$

where the atomic state is described as $|\psi\rangle = c_g|g\rangle + c_e|e\rangle$, $\Omega = -\langle g|\hat{e} \cdot d|e\rangle\mathcal{E}_0/\hbar$ is the Rabi frequency, ω and $\mathcal{E}_0$ are the electric field frequency and amplitude, and Δ is the detuning from resonance. If the initial population is in the ground state the solution is

$$\begin{aligned} c_g(t) &= e^{i\Delta t/2}\left[\cos\left(\frac{1}{2}\tilde{\Omega}t\right) - i\frac{\Delta}{\tilde{\Omega}}\sin\left(\frac{1}{2}\tilde{\Omega}t\right)\right], \\ c_e(t) &= -ie^{i\Delta t/2 - i\omega t}\frac{\Omega}{\tilde{\Omega}}\sin\left(\frac{1}{2}\tilde{\Omega}t\right), \end{aligned} \tag{2.2}$$

where $\tilde{\Omega} = \sqrt{\Omega^2 + \Delta^2}$. The time dependent probability for the atom to be in the excited state can be written as

$$P_e = \frac{\Omega^2}{\tilde{\Omega}^2}\sin^2\left(\frac{1}{2}\tilde{\Omega}t\right). \tag{2.3}$$

Introducing a damping, or spontaneous emission rate Γ, the scattering rate can be written as [130]

$$R = \frac{1}{2\pi}\Gamma\frac{\Omega^2/2}{\Delta^2 + \Omega^2 + \Gamma^2/2}. \tag{2.4}$$

For later calculations the Rabi frequency was calculated using $\Omega = I2\pi c^2/(\hbar\omega^3)$, where I is the intensity of the laser.

For a two-photon transition this model can be extended. In a general two-photon excitation the photon pair ω_1 and ω_2 excites the atom through a virtual intermediate

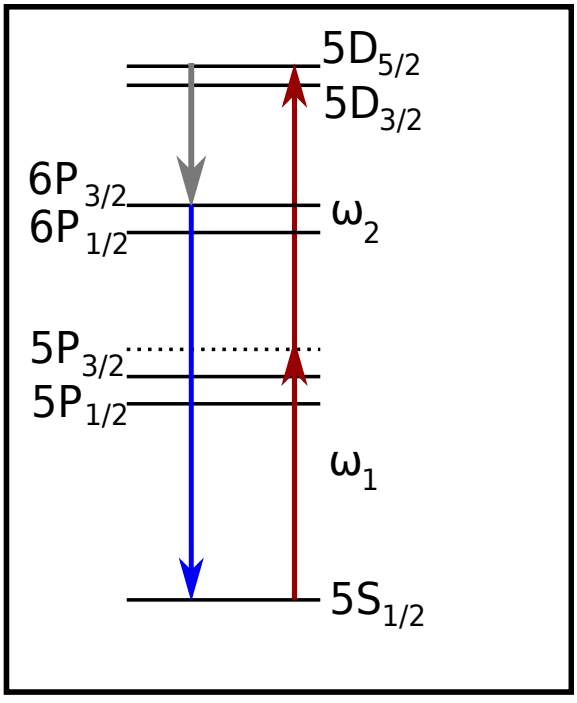

Figure 2.1: The states involved in the two-photon transition in Rb as described in the text.

state, usually providing counter-propagating photons to achieve partial cancellation of the laser $\vec{k}$ vector. Figure 2.1 shows the general case of exciting a Rb atom, $5S_{1/2} \rightarrow 5D_{5/2}$, though a two-photon process. The total electric field can be written,

$$\overrightarrow{\mathcal{E}}(t) = \frac{1}{2}\left[\exp(i\omega_1 t) + \exp(-i\omega_1 t)\right]\mathcal{E}_1\hat{e}_1 + \frac{1}{2}\left[\exp(i\omega_2 t) + \exp(-i\omega_2 t)\right]\mathcal{E}_2\hat{e}_2. \quad (2.5)$$

The counter-rotating terms are usually negligible and can be ignored for simplicity, and the matrix element for an excitation from the ground state $|g\rangle$ to some intermediate state $|k\rangle$ can be written,

$$\langle k|\mathbf{H}|g\rangle = -\mathcal{E}_1\frac{\langle k|\hat{e}_1\cdot\mathbf{d}|g\rangle}{2}\exp(-i\omega_1 t) - \mathcal{E}_2\frac{\langle k|\hat{e}_2\cdot\mathbf{d}|g\rangle}{2}\exp(-i\omega_2 t). \quad (2.6)$$

If the atom is initially in the ground state the time dependent Schrödinger equation

can be integrated, yielding

$$\Psi_{g\to k}(t) = -\frac{1}{2\hbar}\left[\mathcal{E}_1\frac{\langle k|\hat{e}_1\cdot\mathbf{d}|g\rangle}{2}e^{-i\left(\omega_1-\omega_{kg}\right)t} + \mathcal{E}_2\frac{\langle k|\hat{e}_2\cdot\mathbf{d}|g\rangle}{2}e^{-i\left(\omega_2-\omega_{kg}\right)t}\right]. \tag{2.7}$$

The same methodology can be applied to derive the waveform exciting the atoms from the intermediate state to the final excited state, yielding

$$\begin{aligned}\Psi_{g\to f}(t) = \frac{1}{4\hbar^2}\Bigg[&\frac{\mathcal{E}_1^2\langle e|\hat{e}_1\cdot\mathbf{d}|k\rangle\langle k|\hat{e}_1\cdot\mathbf{d}|g\rangle}{\omega_1-\omega_{kg}}\frac{e^{i(\omega_0-2\omega_1)t}-1}{\omega_0-2\omega_1}\\ &+\frac{\mathcal{E}_2^2\langle e|\hat{e}_2\cdot\mathbf{d}|k\rangle\langle k|\hat{e}_2\cdot\mathbf{d}|g\rangle}{\omega_2-\omega_{kg}}\frac{e^{i(\omega_0-2\omega_2)t}-1}{\omega_0-2\omega_2}\\ &+\frac{\mathcal{E}_2\mathcal{E}_1\langle e|\hat{e}_2\cdot\mathbf{d}|k\rangle\langle k|\hat{e}_1\cdot\mathbf{d}|g\rangle}{\omega_1-\omega_{kg}}\frac{e^{i(\omega_0-\omega_2-\omega_1)t}-1}{\omega_0-\omega_2-\omega_1}\\ &+\frac{\mathcal{E}_2\mathcal{E}_1\langle e|\hat{e}_1\cdot\mathbf{d}|k\rangle\langle k|\hat{e}_2\cdot\mathbf{d}|g\rangle}{\omega_2-\omega_{kg}}\frac{e^{i(\omega_0-\omega_2-\omega_1)t}-1}{\omega_0-\omega_2-\omega_1}\Bigg].\end{aligned} \tag{2.8}$$

The first two terms originate from absorbing a photon from one source. The third and forth terms are cases where photons from each source are utilized in excitation. In the case where $\omega_1 \neq \omega_2$ the total frequency is generally off resonance and these two terms can be ignored. The excitation probability for the non-degenerate case (ignoring absorption of two-photons from one source), assuming that ω_1 is much closer to resonance with the $|g\rangle \to |k\rangle$ transition is,

$$W_{g\to e} \approx \frac{1}{4\hbar^4}\frac{\mathcal{E}_2^2\mathcal{E}_1^2|\langle e|\hat{e}_2\cdot\mathbf{d}|k\rangle|^2|\langle k|\hat{e}_1\cdot\mathbf{d}|g\rangle|^2}{\left(\omega_1-\omega_{kg}\right)^2}\frac{\sin^2\left[\left(\omega_0-\omega_1-\omega_2\right)t/2\right]}{\left(\omega_0-\omega_2-\omega_1\right)^2} \tag{2.9}$$

The excitation rate of such a transition can be found by integration over an appropriate spectral distribution [58],

$$R_{2\gamma} = \frac{\pi}{8\hbar^4}\left[\frac{\mathcal{E}_2^2\mathcal{E}_1^2|\langle e|\hat{e}_2\cdot\mathbf{d}|k\rangle|^2|\langle k|\hat{e}_1\cdot\mathbf{d}|g\rangle|^2}{\left(\omega_1-\omega_{kg}\right)^2}\right] f(\omega), \tag{2.10}$$

where

$$f(\omega) = \frac{\gamma/2}{4\delta\omega+\gamma^2/4}. \tag{2.11}$$

An important feature to note is that $R_{2\gamma} \propto I_1 I_2$, an important consideration later in Section 2.6.5 and an important tool to increase clock stability. Other variables in the

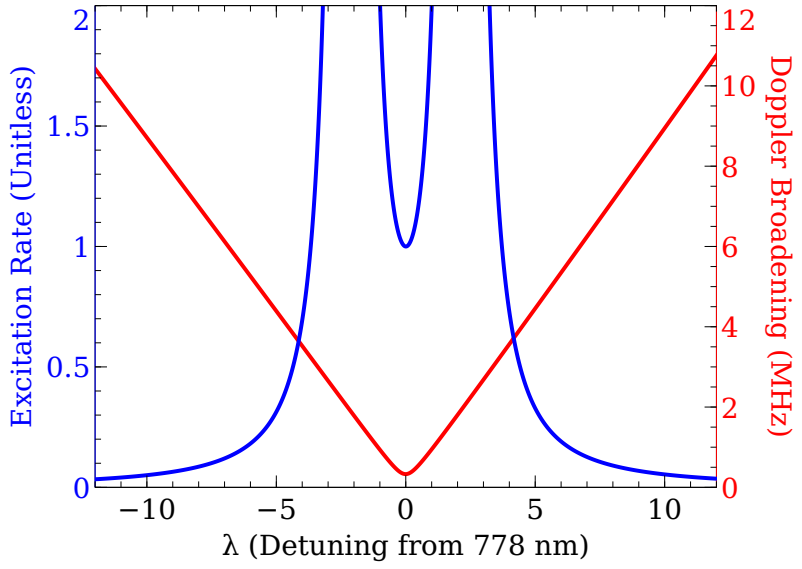

Figure 2.2: The excitation rate (blue) and Doppler broadened linewidth (red) plotted versus detuning of ω_1 from the degenerate case. The second photon ω_2 is constrained such that the sum of the frequencies is on resonance with the final excited state. The excitation rate is normalized by the degenerate rate.

equation include: γ is the decay rate of the excited state, $5D_{5/2}$, and $\delta\omega = \omega_{eg} - \omega_1 - \omega_2$ is the detuning of the combined two-photon frequency from resonance of the final transition. When $\omega_1 \neq \omega_2$ the Doppler broadened linewidth is given by

$$\Delta\nu_D = \sqrt{\Delta_{2\gamma}^2 \frac{2k_B T}{mc^2} + \Delta\nu^2}, \tag{2.12}$$

where $\Delta\nu$ is the natural linewidth, $\Delta_{2\gamma} = |\omega_1 - \omega_2|/2$ is the single photon detuning from the Doppler free case, and m is the mass of a rubidium atom.

Equation 2.10 was evaluated in the special case where $\delta\omega = 0$ as a function of detuning, $\Delta_{2\gamma}$, from the degenerate 778.1 nm pair, and the result is plotted in Figure 2.2 along with the Doppler broadened linewidth. A choise of $\lambda \neq$778.1 nm results in broadening the transition linewidth and decreasing the excitation rate and will

reduce the short term stability ($\tau = 1$ s) of the clock, given by

$$\sigma_y \propto \frac{\Delta\nu_D}{\sqrt{R_{2\gamma}}}. \tag{2.13}$$

Optimizing the clock stability can be achieved by increasing the two-photon excitation rate.

Rather then utilizing degenerate photon pairs one could reduce the required laser power by allowing one photon to approach the $5P_{3/2}$ resonance. The excitation rate reported in 2.10 is proportional to Δ^2 and the Doppler broadening is directly related to Δ. Equation 2.13 shows that the same stability can be achieved with non-degenerate pairs of photons. This two-color two-photon approach has been investigated to further reduce common clock instabilities and required laser power [57, 106, 107]. However, as the virtual state approaches $5P_{3/2}$ the linewidth of the D_2 transition will begin to dominate. When the scattering rate of a single photon process is of the same order as the natural linewidth of the two-photon transition in Rb this extra broadening can become problematic. Figure 2.3 shows the single photon excitation rate calculated with Equation 2.4. The broadening is predicted to become problematic when the virtual state is less than 1 GHz from resonance, because of this Refs. [57, 106, 107] operate their two-color two-photon experiments well outside of this region. However, as the transition linewidth is broadened, there is concern about long term stability. As difficult as it is to stabilize environmental effects, a broader line could put tougher restrictions on the system.

While two arbitrary photons could be used to excite the atom, the case of a single retro-reflected source is of interest for simplicity and in the interest of long-term stability. Here, $\omega_1 = \omega_2 = \omega$ and $\hat{e}_1 = \hat{e}_2 = \hat{e}$. In this case, absorption of two-photons from either the forward going beam or a retro-reflected beam is possible first two terms in Equation 2.8. However, since the laser interacts with a hot atomic vapor and, in this situation, Doppler shifts are important, this absorption is velocity selective and does not excite the entire vapor. Exciting atoms in this manner occurs

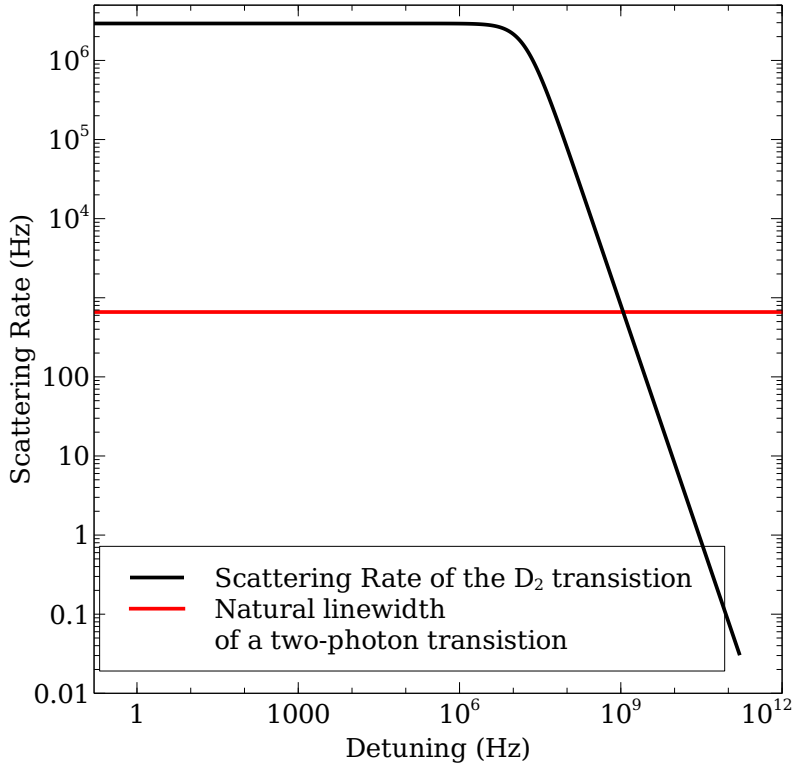

Figure 2.3: Shown above is the calculated (using Equation 2.4) scattering rate of the D_2 line in Rb as a function of detuning (black). In this calculation, the Rabi frequency $\Omega = I 2\pi c^2/(\hbar\omega^3)$, was calculated using a 10 mW beam with a 0.6 mm $1/e^2$ beam waist. If this rate becomes comparable to the natural linewidth of the two-photon transition (red) in Rb there will be residual broadening.

with much lower probability then the Doppler free case and the excitation probability can be written,

$$W_{g\to e} \approx \frac{1}{2\hbar^4}\frac{\mathcal{E}_2^2\mathcal{E}_1^2}{\left(\omega_- - \omega_{kg}\right)^2}\frac{\sin^2\left[\left(\omega_0 - 2\omega\right)t/2\right]}{\left(\omega_0 - 2\omega\right)^2}|\langle e|\hat{e}\cdot\mathbf{d}|k\rangle|^2|\langle k|\hat{e}\cdot\mathbf{d}|g\rangle|^2. \tag{2.14}$$

For generality $\mathcal{E}_1 \neq \mathcal{E}_2$, as there is assuredly loss in the retro-reflective optics. The excitation rate for a degenerate Doppler free two-photon transition is,

$$R_{2\gamma,D} = \frac{\pi}{4\hbar^4}\frac{\mathcal{E}_2^2\mathcal{E}_1^2}{\left(\omega_- - \omega_{kg}\right)^2}|\langle e|\hat{e}\cdot\mathbf{d}|k\rangle|^2|\langle k|\hat{e}\cdot\mathbf{d}|g\rangle|^2 f(\omega), \tag{2.15}$$

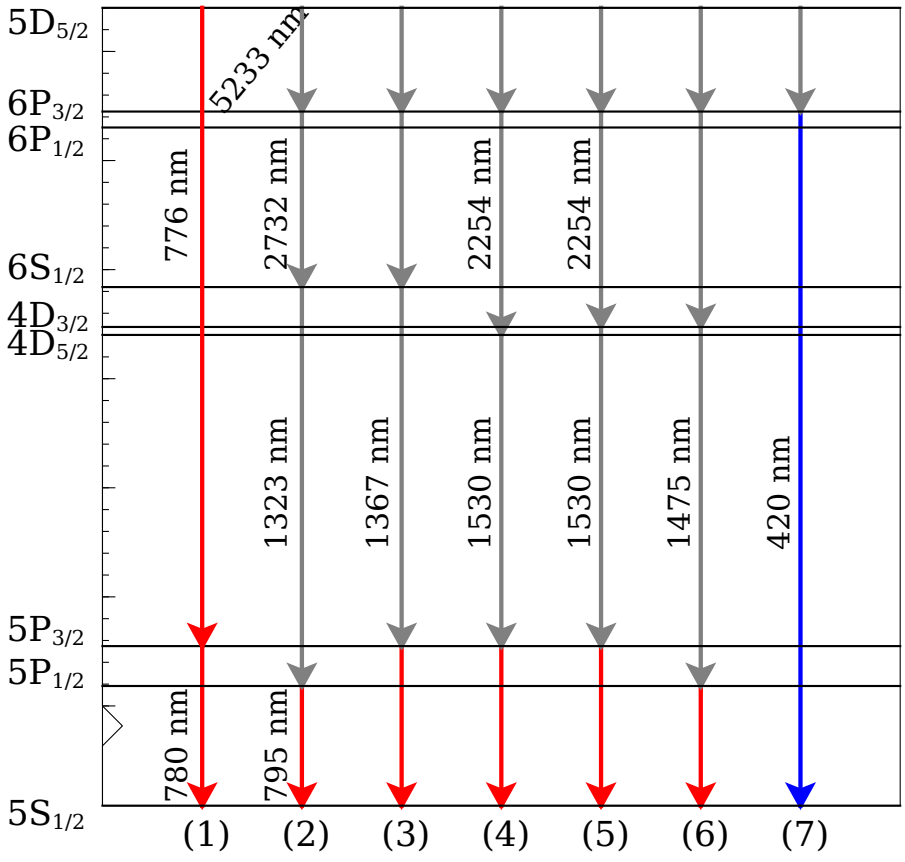

Figure 2.4: All of the possible spontaneous decay channels from the $5D_{5/2}$ excited state.

2.2 Fluorescence Detection

After the atom is excited to the $5D_{5/2}$ state, it will decay through one of a possible seven channels (see Figure 2.4). Detection at 420 nm proposed by Refs. [65,92] is not the only option for fluorescence detection, and does not have the highest probability of occurrence.

Careful consideration into simplicity and manufacturability will drive the fluorescence detection method. Fused silica and Pyrex are common material choices for

the construction of vapor cells. Infrared detection of Rb fluorescence is not ideal as these glasses maintain a large optical depth between 1-3.5 μm and are opaque for wavelengths greater then 3.5 μm [77]. Fluorescence generated in the vapor cell must then travel through Rb vapor in it's ground state before detection. The excitation rates of the resonant $5P_{3/2}$ and $5P_{1/2}$ states make detecting on either 780 nm or 795 nm difficult as Rb vapor still in the ground state will re-absorb and reduce the detected signal, a process called radiation trapping. The only real options are to detect 776 nm or 420 nm light released in the decay channels shown in Figure 2.4 (1) and Figure 2.4 (7). Ideally, the more probabilistic decay should be utilized to maximize the signal to noise ratio.

The decay probability, or branching ratio, can be calculated using the Einstein A coefficient, [35, 45, 64],

$$A_{J,J'} = \frac{2\omega^3(e_c a_0 \langle J|d|J'\rangle)^2}{3\epsilon_0 hc^3(2J+1)}. \tag{2.16}$$

Equation 2.16 calculates the coefficient in SI units where e_c is the electron charge, a_0 is the Bohr radius, ω is the transition frequency, h is planks constant, c is the speed of light, ϵ_0 is the permeability of free space and J is the total angular momentum quantum number. Using the Einstein A coefficients displayed in Appendix A the branching ratio of each of these decays can be calculated. Approximately 74% of the time the atom decays by emitting a 776 nm and a 780 nm photon and in only 6.2% of the time the atomic decay results in a 420 nm photon.

Fluorescence detection at 776 nm is an intriguing option. 776 nm is not on resonance with a transition involving the ground state, so there is no radiation trapping[2] of the fluorescence signal. Coupled with the higher decay probability and the higher

[2]Most of the atoms in the vapor cell are in the ground state. If light generated is on resonance with a transition which includes the ground state the fluoresced light could be re-scattered by the ground state atoms. This phenomenon known as radiation trapping reduces the measured fluoresced signal.

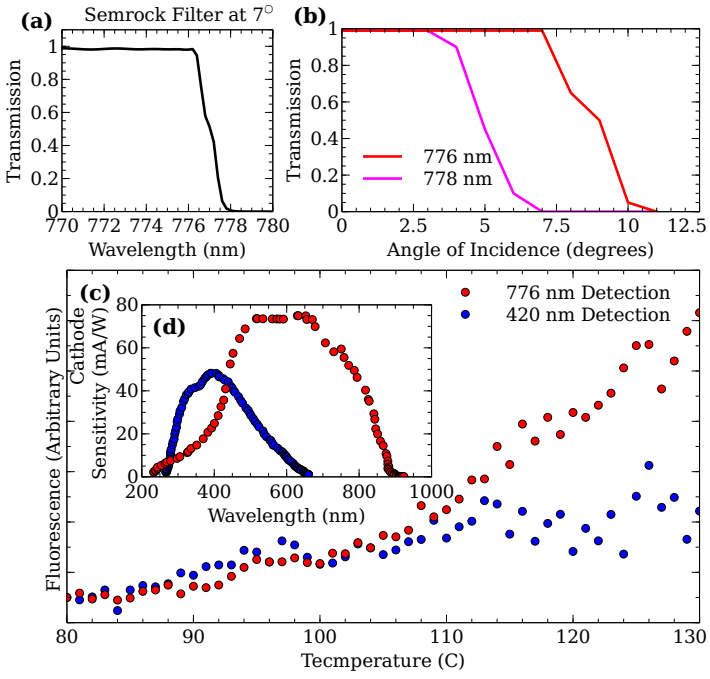

Figure 2.5: (a) Transmission as a function of wavelength of a Semrock Edge filter. An angle of incidence of 7° is necessary to discriminate between the 778 nm noise and the 776 nm signal, quite a narrow band of proper alignment. (b) Transmission of the filter as a function of angle of incidence for for 776 nm and 778 nm light. (c) Fluorescence data from collecting 776 nm (red dots) and 420 nm (blue dots), the blue photons experience radiation trapping as predicted in the text. (d) The cathode efficiency of the photo multiplier tube (PMT) detectors used to detect the 776 nm (red) and 420 nm (blue) fluorescence as a function of wavelength.

quantum efficiencies found in detectors manufactured for red light detection, 776 nm fluorescence seems like an ideal choice for increased signal to noise ratio, see Figure 2.5. Alternatively, detection at 420 nm would experience radiation trapping, and is a much less probabilistic decay channel, over 10× less. However, filtering the 778 nm probe light from the signal becomes problematic when detecting 776 nm photons. Filters whose cutoff frequency is sharp enough often require precise alignment angles to distinguish between light at 778 nm and 776 nm. Considering the fluorescence signal is a line source radiating isotropically, significant efforts to collect and colli-

mate the light would need to be considered to properly increase the signal to noise ratio.

In an attempt to quell these concerns, detection at 776 nm was employed. Increased vapor pressure tends to make radiation trapping more problematic, thus temperature dependent detection at 776 nm was measured (as vapor cell temperature and pressure are related). Figure 2.5 (c) has been normalized to display the temperature (or vapor pressure) dependent behavior of radiation trapping. As predicted, there was no radiation trapping when detecting at 776 nm. Unfortunately, after adding collimation optics and the correct filter there was fifty times less signal detected at 776 nm than at 420 nm. Currently, detection at 420 nm has shown greater signal to noise ration (SNR) levels and a simplified alignment arrangement. For these reasons the clock signal will be detected along the $6P_{3/2} \rightarrow 5S_{1/2}$ decay.

2.3 Magnetic Sensitivities and the Isotope Choice

Magnetic sensitivities coupled with transition strengths drive the isotope decision. Described here is the calculation of the expected magnetic sensitivity of the optical rubidium atomic frequency standard (O-RAFS). To not limit the calculation to the strong or weak field regimes the intermediate or incomplete Paschen-Bach regime was considered. The magnetic field shift in the incomplete Paschen-Bach regime of the $5S_{1/2}$ ground state can be analytically calculated utilizing the Breit-Rabi formula [26]; because the spectroscopic technique does not resolve transitions between specific magnetic sublevels, the final answer is the average over all relevant m_I and m_J magnetic quantum numbers, yielding,

$$\bar{E} = \Delta E_{HFS} \frac{I}{2I+1} + \frac{1}{2} \frac{\mu_B^2 \left(g_J - g_I\right)^2}{\Delta E_{HFS}} \left[\frac{5}{14} - \frac{20}{7\left(2I+1\right)^2}\right] B^2 \qquad (2.17)$$

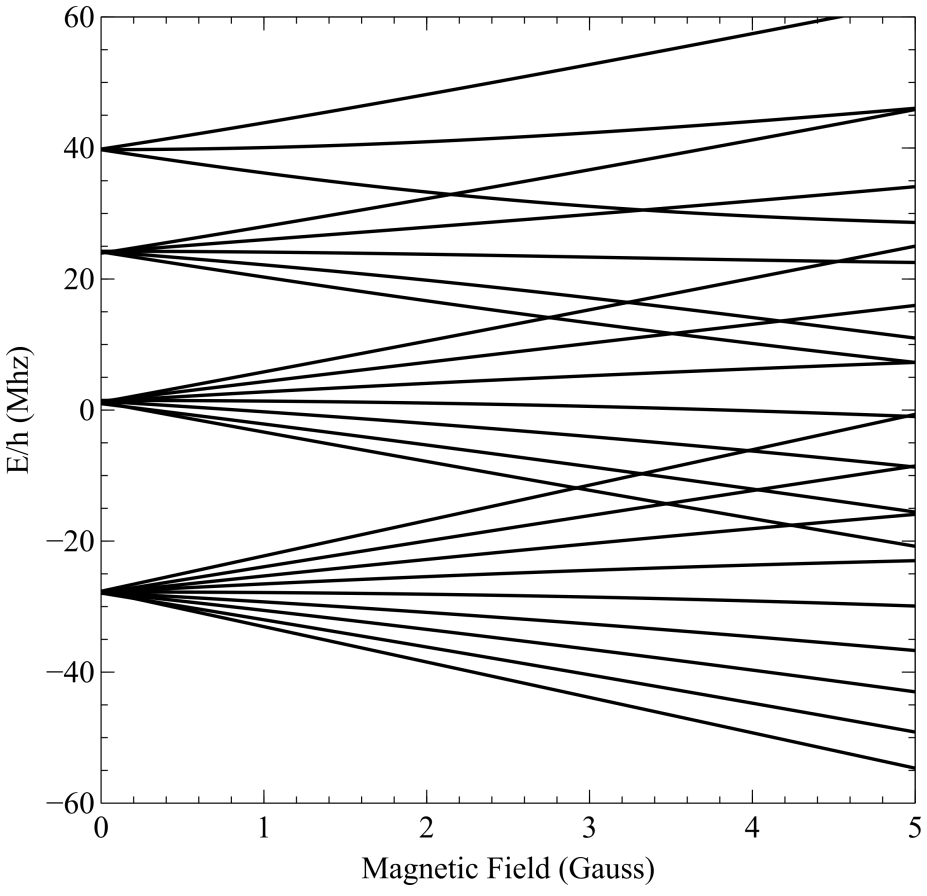

Figure 2.6: Magnetic field splitting for the $5D_{5/2}$ states of of ^{87}Rb, which was determined by numerical diagonalization of the total Hamiltonian as described in the text. Figure from Ref. [92].

for ^{85}Rb and,

$$\bar{E} = \Delta E_{HFS} \frac{I}{2I+1} + \frac{1}{2} \frac{\mu_B^2 \left(g_J - g_I\right)^2}{\Delta E_{HFS}} \left[\frac{3}{10} - \frac{4}{5\left(2I+1\right)^2}\right] B^2 \qquad (2.18)$$

for ^{87}Rb. Here, I is the nuclear spin, μ_B is the Bohr magneton and B is the applied magnetic field, and $\Delta E_{HFS} = A_{HFS}(I + 1/2)$ where A_{HFS} is the magnetic dipole constant. This assumption results in no first-order (linear) dependence of the clock frequency on magnetic field, and is valid for local magnetic fields $\leq$100 mG, which is roughly the field at which Zeeman-induced line-broadening exceeds the natural linewidth of the two-photon transition. Substitution of the Landé g-factors, g_J and

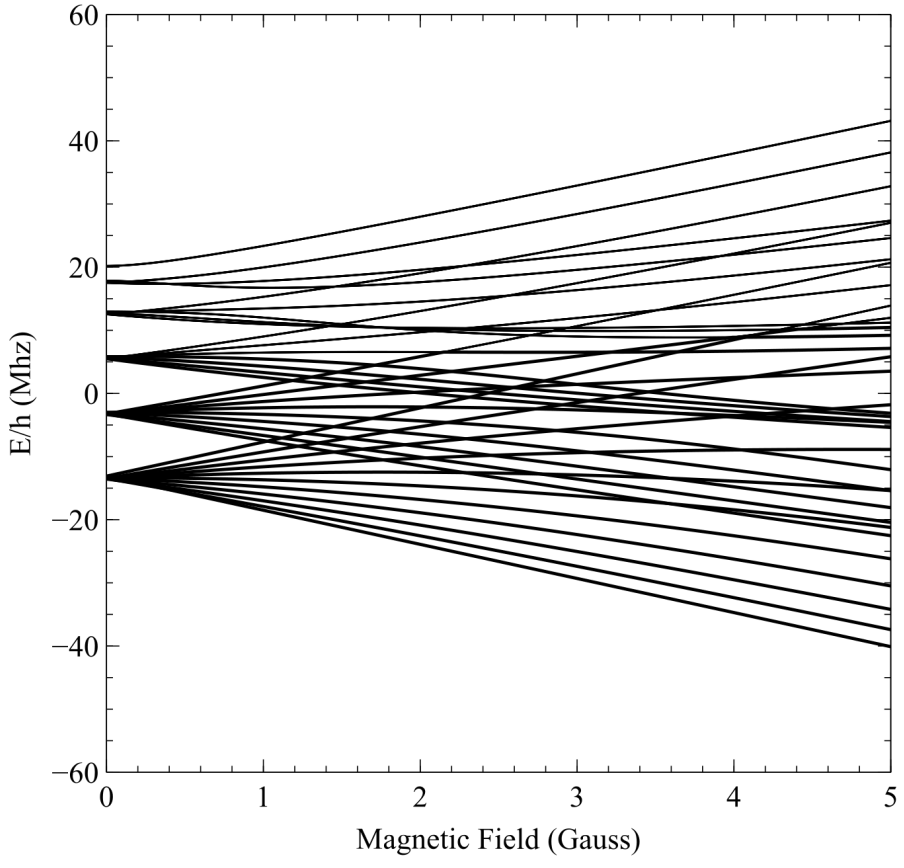

Figure 2.7: Magnetic field splitting for the $5D_{5/2}$ states of of ^{85}Rb, which was determined by numerical diagonalization of the total Hamiltonian as described in the text.

g_I and the magnetic dipole constant collected in Appendix A yields a second order ground state shift of 114 Hz/G^2 for ^{87}Rb (F=2) and 358 Hz/G^2 for ^{85}Rb (F=3).

The clock shift for the $5D_{5/2}$ excited state does not have a simple analytical

solution. The Hamiltonian,

$$\begin{aligned}
&\boldsymbol{H} = \boldsymbol{H}_{hfs} + \boldsymbol{H}_B^{(hfs)}, \\
&\boldsymbol{H}_{hfs} = A_{hfs}\frac{\boldsymbol{I}\cdot\boldsymbol{J}}{\hbar^2} \\
&+ B_{hfs}\frac{\frac{3}{\hbar^2}(\boldsymbol{I}\cdot\boldsymbol{J})^2 + \frac{3}{2\hbar}(\boldsymbol{I}\cdot\boldsymbol{J}) - J(J+1)I(I+1)}{2I(2I-1)J(2J-1)}, \\
&\boldsymbol{H}_B^{(hfs)} = \mu_B(g_J\boldsymbol{J_z} + g_I\boldsymbol{I_Z})B,
\end{aligned}$$

was generated and diagonalized numerically and details can be found in Appendix B. Substituting the magnetic dipole and quadrapole constants, A_{hfs} and B_{hfs}, for the $5D_{5/2}$ level listed in Appendix A results in a state shift of 50 kHz/G^2 for ^{87}Rb (F=4) and 190 kHz/G^2 for ^{85}Rb (F=5). The $5D_{5/2}$ state has a larger shift than the ground state in the presence of magnetic fields, almost 500 times more sensitive, this is because the shift is $\propto B^2/A_{HFS}$.

The final desired clock is one that reduces required laser power and sensitivity to environmental parameters. Table A.1 shows that the relative intensity of the $F_g = 2 \rightarrow F_e = 4$ in ^{87}Rb transition is larger then the $F_g = 3 \rightarrow F_e = 5$ in ^{85}Rb. Less incident laser power is required to achieve the same signal to noise ratio. This coupled with reduced sensitivity to magnetic field fluctuations make ^{87}Rb a more desirable choice. Since ^{87}Rb is less abundant an isotopically enriched cell is required.

2.4 Design

An atomic clock leverages the natural occurrence of stable energy levels present in an atom. This atom is the sensor, which is probed to stabilize a LO to remain on resonance with this natural transition. Frequency or phase modulation techniques are commonly used to probe the transition and keep the LO on resonance. This technique involves either modulating the frequency or the phase of the LO slightly. As the LO moves away from resonance the detected signal will change. In practice

the signal used to modulate the laser is mixed with the detected signal from the atoms, the frequency mixer generates a signal that is the sum and difference of the two frequencies involved. Sweeping the laser over the non-linear lorentzian will only generate the exact frequency of modulation at the maximum (or minimum), allowing the LO to be stabilized around a zero crossing.

The practical noise limit of a frequency standard is the greater of the LO noise and the shot noise associated with detecting the atomic transition, Equation 1.6. Continuously operated (as opposed to pulsed) frequency standards are most sensitive to LO noise at twice the modulation frequency ($f_m = 130$ kHz in this Chapter) [10]. Noise at this frequency (or higher even harmonics) is down-sampled by the demodulation process and remains partially uncompensated, thereby degrading the frequency standard's stability in a manner that is analogous to the Dick effect in pulsed frequency standards [43]. This instability source is known as the Intermodulation Effect [10] and can be calculated as

$$\sigma_y^{(IM)}(\tau) = \frac{S_y^{(LO)}[2f_m]}{2\sqrt{\tau}}, \tag{2.19}$$

where $S_y^{(LO)}[2f_m]$ is the power spectral density of LO frequency noise at $2f_m$.

The signal measured from the atomic source, properly demodulated, is used to correct the LO. A simulated fluorescence and error signal spectrum are shown in Figure 2.8. Because the generated error signal is coupled to the transition frequency of the atoms, clock instability can be thought of in two different time frames: short-term stability, which is dominated by the noise on the LO or detection SNR, and long-term stability, which is dominated by atomic frequency shifts and servo error. This section examines in detail the design of the laser and atomic detection to mitigate clock instability.

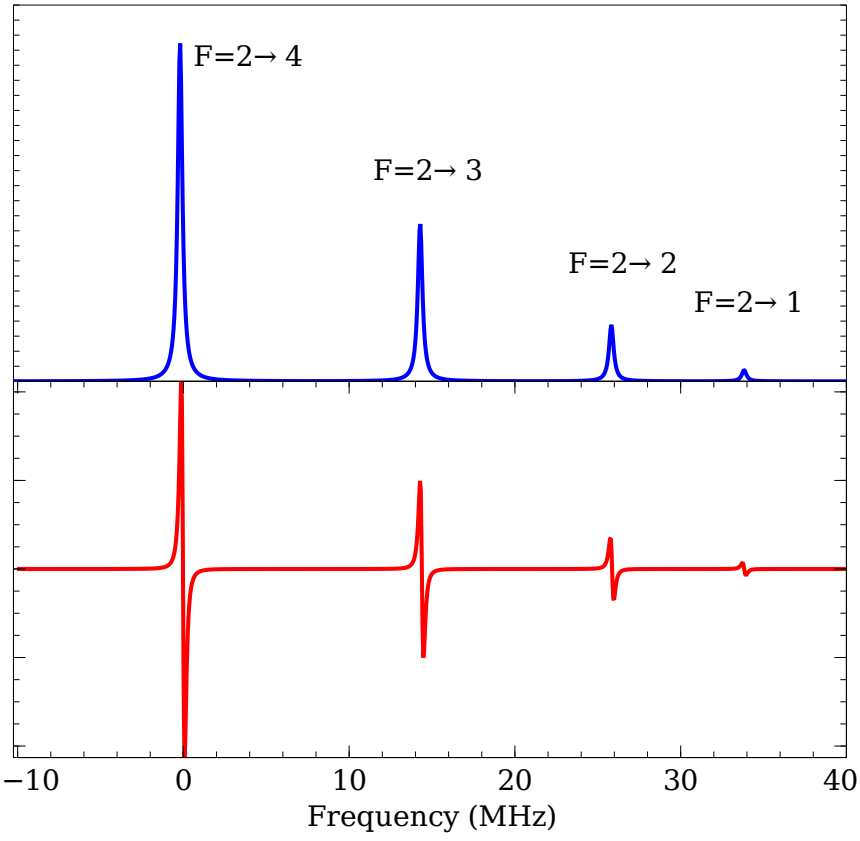

Figure 2.8: Simulated fluorescence (blue) and error signal (red) for ^{87}Rb. The error signal in the above figure was generated by taking the derivative of the simulated signal.

2.4.1 Clock laser design

A suitable laser to excite hot rubidium vapor through a degenerate two-photon transition must provide optical power at the correct frequency, 778.1 nm, and have necessary output frequency noise and optical power to achieve short term fractional frequency instability of 1×10^{-13} at one second. Furthermore, the system must have authority to regulate the final optical output power to suppress ac-Stark effects (see Section 2.6.5). Finally, the laser must allow for phase or frequency modulation, required to generate the error signal seen in Figure 2.8. Three initial independent

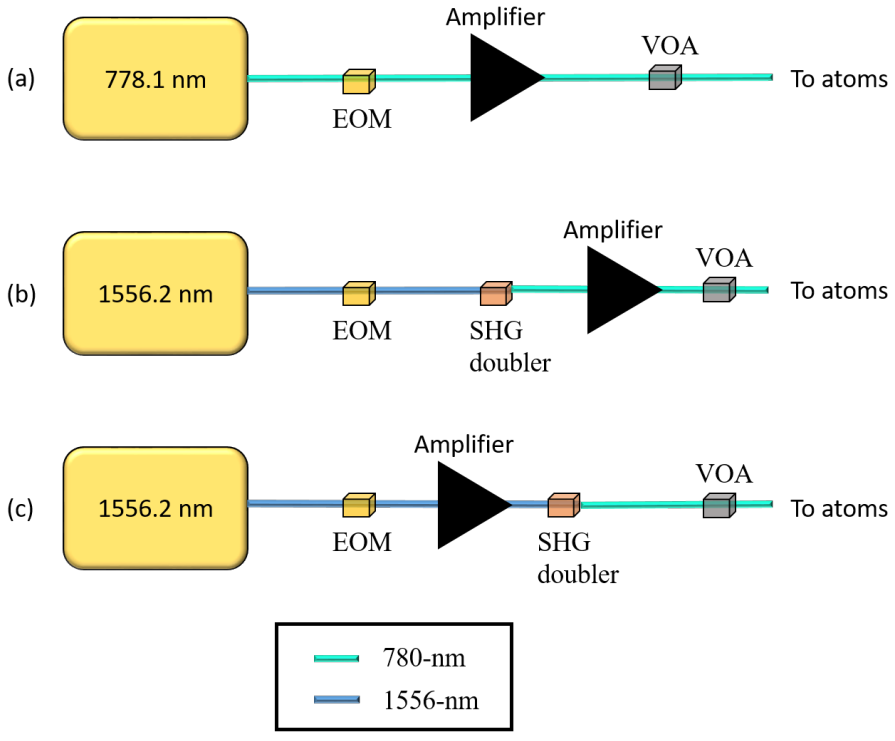

Figure 2.9: Shown above are three purposed designs for the O-RAFS clock laser, each design was tested and design (c) best met the requirements laid out in the text. (a) is the direct diode laser design, (b) and (c) utilize a telecom C-band seed laser the light then undergoes amplification and second harmonic generation (SHG) the difference in design rests in the order of these operations.

clock laser designs were purposed, and Figure 2.9 shows the major components of the laser. Each system was investigated and a final clock laser design (with appropriate seed) was settled on. Each laser system has an amplifier, allowing increase of final optical power necessary to reach short term stability goals in the shot-noise limit and a variable optic attenuator (VOA) to ensure authority over final optical power.

Leveraging a diode at 778.1 nm is the most direct method of producing the required excitation frequency (see Figure 2.9 (a)). The simplified system consists of the seed laser, an electro-optic modulator (EOM) to generate the error signal, an amplifier, and VOA. The seed laser utilized was a AOSense external cavity diode

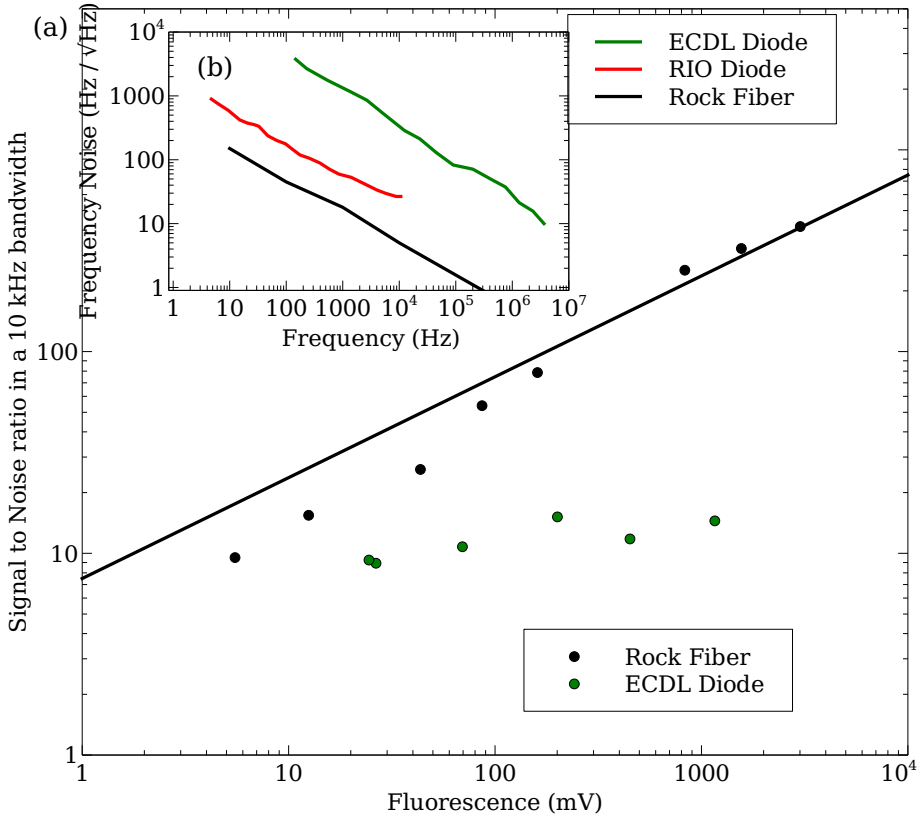

Figure 2.10: (a) Shows the signal to noise ratio of a clock system using the AOSense external cavity diode laser (ECDL) laser and the Rock fiber laser as a function of collected fluorescence (increased optical power). (b) Details the frequency noise of three potential seed laser sources as quoted by manufacture. [7, 101, 129]. Figure adapted from a version originally presented in [15]

laser (ECDL) with a linewidth of < 100 kHz and output power of > 50 mW [7]. This system required substantial use of free space optics thus decreasing overall system wall-plug efficiency, and required the use of several free-space isolators, increasing the magnetic shielding requirements around the Rb vapor cell. It was determined that at fractional frequency instabilities of 6.5×10^{-13} at one second the system was no longer limited by shot-noise, but rather by the intermodulation limit, given by Equation 2.19. In the shot-noise limit greater clock stability (larger SNR) can be achieved by increasing atomic fluorescence (optical power). Figure 2.10 (a) shows

that as the clock laser optical power (atomic fluorescence) was increased the SNR remained constant.

The laser designs shown in Figure 2.9 (b) and (c), require use of telcom c-band components and eventual frequency conversion. Two seed lasers at 1556.2 nm were identified whose frequency noise and spectral linewidth were less the AOSense ECDL source, see Figure 2.10 (b). A NP Photonics Rock fiber laser was integrated into the design shown in Figure 2.9 (c), utilizing a fiber coupled, semiconductor optical amplifier (SOA). This clock is still shot-noise limited while producing fractional frequency instabilities of 1×10^{-13} at one second. Figure 2.10 shows that increasing the optical power of the clock laser results in increased SNR. Ultimately, this seed laser had a high frequency of mode hops (1-2 per week) undermining operation on long timescales. The Redfern integrated optics (RIO) Planex diode seed laser has been integrated into both telecom laser architectures, as the mode hop frequency is much less than the Rock fiber laser (< 1 per year). This laser is an edge waveguide external cavity diode laser [101]. Although the RIO has more frequency noise, each clock laser design has allowed for fractional frequency instabilities of 1×10^{-13} at one second, making it the seed laser of choice for the final design. Subsequently, the clock laser shown in Figure 2.9 (c) was chosen based on available parts, the laser system is described in further detail in Section 2.4.3.

2.4.2 Rubidium Atomic Reference

The physics package of the optical rubidium atomic frequency standard (O-RAFS) allows for the study of environmental impact on clock performance. Figure 2.11 (a) shows the preliminary design of the Rubidium Atomic Reference or RAR. The clock laser enters through a fiber launcher, collimating the incident beam. The beam then propagates through a polarizer and a turning mirror before being sampled and measured with a Thorlabs PDA100A photodetector. The beam then travels through

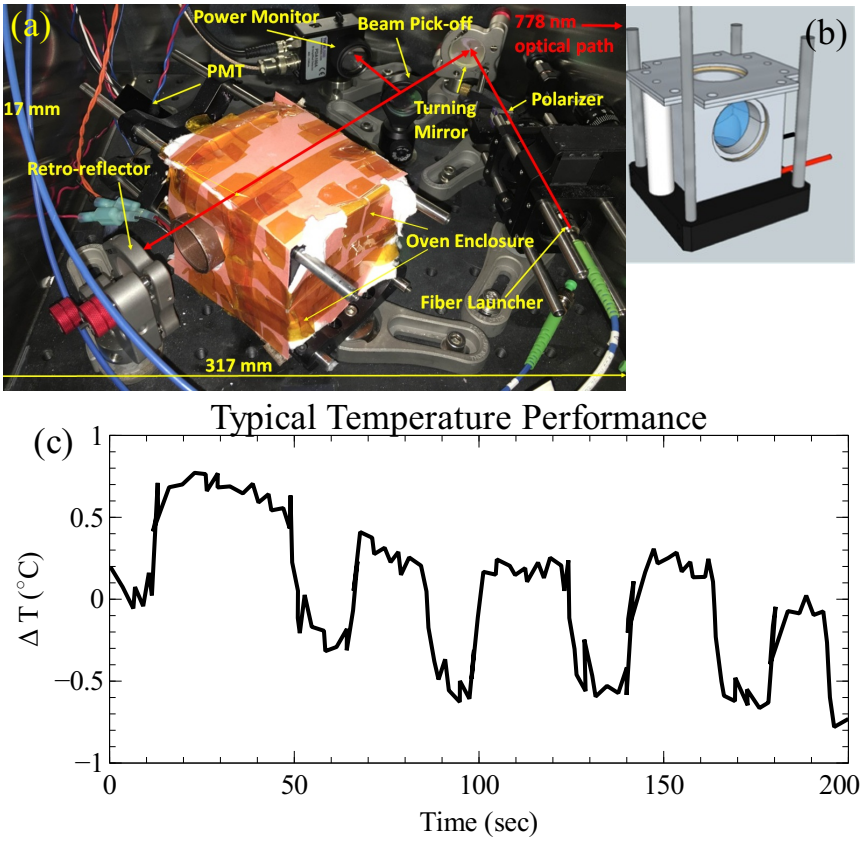

Figure 2.11: Shown in (a) is the original RAR 1.0 design, a computer animated drawing of the vapor cell magnetic shield enclosure (b) and typical temperature profile of the vapor cell (c).

the vapor cell, oriented at Brewster's angle to reduce Fresnel reflection losses, before reflecting off a retro-reflector. The atomic fluorescence is detected with a Hamamatsu high temperature PMT model number H10721-01 through an optical bandpass filter. Opposite the PMT lies a parabolic mirror, designed to increase fluorescence collection efficiency.

Magnetic field broadening of the atomic line represents a serious concern for final clock performance. For this reason, the Rb cell was encased in a mu-metal clamshell, designed for suppression of the static magnetic field by 1000. (see Figure 2.11 (b)).

The heating element, in this case a thermoelectric heater, was placed outside the mu-metal clamshell as well as two thermistors, one to close a temperature servo loop, stabilizing the vapor cell temperature to 100 °C and the other as a temperature witness. Figure 2.11 (c) shows typical temperature control performance. Unfortunately, the temperature performance of the vapor cell assembly was not suitable for clock performance temperature requirements outlined in Refs. [92, 146] and measured in Section 2.6.1. The primary reason for poor temperature control was the temperature controller utilized. The quoted *best case* temperature stability was 0.1 °C with a unidirectional temperature control. Moreover, precision temperature control of mu-metal is difficult. Commonly used for temperature control, copper has a thermal conductivity around 400 W/(K m) and a specific heat of 0.385 J/(g °C), while mu-metal has a thermal conductivity around 19 W/(K m) and a specific heat of 0.46 J/(g °C). An electric circuit equivalent for heat conduction can be exploited for thermal modeling purposes [3]. In this "RC circuit" thermal system the relaxation time constant for mu-metal is 0.024 s/(g m) where copper has a time constant of 0.0007 s/(g m). A system designed around a copper clamshell would be more reactive to changes in input thermal energy and easier to control. A new design was built leveraging water filled heat pipes to conduct the heat generated outside of a mu-metal enclosure to a copper vapor cell clamshell. This design is further described in Section 2.4.3.

2.4.3 Final Design

The design shown in Figure 2.12 begins with a RIO Planex diode laser, producing linearly polarized light at 1556.2 nm. A small portion of the seed laser output is sampled by a fiber splitter to form an optical beat note with a fiber frequency comb based upon the design in [126]. The fully self-referenced frequency comb coherently

[3] A fantastic description of this analog can be found in Ref. [134] applied to the design of thermo-acoustic refrigerators and engines.

divides the 192 THz optical waveform to $\sim$ 200 MHz, which is the comb's pulse repetition rate. After stabilization of the optical beatnote and carrier envelope offset frequency, the comb's repetition rate is photodetected, and a Microsemi 5125A, referenced to a hydrogen maser, is used as a frequency counter. The remaining portion of the 1556 nm laser output enters a fiber-coupled electro-optic phase modulator (EOM) formed in a proton-exchange waveguide embedded in lithium niobate, which is driven at 130 kHz. The drive frequency of the EOM is determined experimentally, choosing a frequency that maximizes the error signal. After the EOM, the light is amplified by an erbium-doped fiber amplifier and undergoes second harmonic generation (SHG) in a periodically poled lithium niobate (PPLN) crystal, outputting as much as 1 W of 778.1 nm light. The output of the SHG crystal, typically around 100 mW , is subsequently sent through a VOA, which is used for laser power stabilization as described below. Typically 30 mW of 778.1 nm light is delivered to the vapor cell assembly.

The vapor cell assembly is enclosed in a 5 mm-thick, single layer mu-metal magnetic shield, to reduce spectral broadening associated with the Zeeman shift. The vapor cell is heated to 100 °C to generate sufficient vapor density for a high stability clock. To avoid local magnetic fields when heating the vapor cell, all heat is generated with resistive and thermo-electric devices located outside the magnetic shielding; water-filled heat pipes protrude through the magnetic shield and provide heat to the dual-zone temperature control stage surrounding the vapor cell. The vapor cell, which is a rectangular prism with dimensions 5 mm $\times$ 5 mm $\times$ 25 mm, containing $>$ 99% isotropically enriched ^{87}Rb, is placed such that it has a 1 K thermal gradient along its length, forcing the cell's cold spot on the pinched-off fill tube of the borosilicate glass cell. The vapor cell is oriented at Brewster's angle with respect to the incident laser beam to reduce stray reflections.

The 778 nm laser output is delivered by polarization-maintaining optical fiber through an opening in the magnetic shield, where it is collimated ($1/e^2$ intensity

radius $w_0 = 0.66$ mm) using a non-magnetic optical assembly. A calcite Glan-Taylor polarizer is placed at the output of the fiber launcher to reduce polarization wander. The laser beam is sampled by a glass plate pick-off before entering the vapor cell; Thorlabs SM05PD1A photodetectors, with dark current 20 nA and active area of 3.5 mm $\times$ 3.5 mm, are placed on each side of the glass plate to monitor the optical power in the sampled beams. A cat eye retro-reflector [128] provides a precisely anti-parallel reflected beam, which is necessary for eliminating Doppler broadening. A portion of the fluorescence at 420 nm passes through a short-pass optical filter and is detected by a photomultiplier tube (PMT) (dark current 5 nA). The PMT provides a fast temporal response and high electron-multiplying gain. After a transimpedance amplifier, the PMT output signal is demodulated by the 130 kHz sinusoidal modulation applied to the EOM in a phase detector, resulting in a laser detuning-dependent error signal. A digital servo controller with dual integrators and approximately 50 kHz bandwidth, limited in this case by the LO, feeds the 1556 nm laser drive current to hold the laser on the two-photon resonance.

This design allows for the study of various parameters that contribute to the system's performance at different time scales. The short-term stability is determined by the atomic linewidth, optical intensity, detector collection efficiency, and laser frequency noise characteristics. The long-term stability requires the stabilization of various experimental and environmental parameters including the vapor cell temperature (Rb vapor density), magnetic field, and optical power; these parameters are investigated in subsequent sections.

2.5 Stability

When a composite standard variance is calculated, a variance arising from individual sources are weighted and summed. Much like the standard variance, a composite Allan variance can be calculated as a sum of all contributing instability variables,

properly scaled, $\sigma_y^2(X+Y) = K_X\sigma_y^2(X) + K_Y\sigma_y^2(Y)$. Stabilizing all environmental parameters and isolating a specific instability can be leveraged to measure the instability coefficients, K_i. Once every relevant coefficient is measured, clock stability is just the composite Allan variance. Although this is true of long term stability, the short term stability of the system is driven by the quality of the atomic signal and the optical oscillator. Because a low-noise (albeit free-running) 1556 nm diode laser is the LO, the intermodulation effect is small and the associated white noise frequency instability is estimated as $2.6 \times 10^{-14}/\sqrt{\tau}$. Under typical operating conditions, the frequency standard is not limited by this intermodulation process but rather by shot noise associated with fluorescence detection at 420 nm.

One can assess the expected instability by analyzing the voltage signal present at the output of the transimpedance amplifier that follows the PMT. Using a fast-Fourier transform analyzer, the signal's power spectral density (S_v) is typically observed as white frequency noise between 1 kHz and 100 kHz. Combined with knowledge of the detuning-dependent error signal magnitude (V_e), the effective gain of the phase detector (g_{PD}) at the modulation frequency f_m, and the atomic linewidth $\Delta\nu$, the clock instability can be estimated as,

$$\sigma_y(\tau) = \frac{\Delta\nu}{2\nu_0}\frac{g_{PD}}{V_e}\sqrt{\frac{S_v}{\tau}}, \tag{2.20}$$

with τ the integration time [65]. Typical values are shown in Table 2.1 and yield an expected one-second Allan deviation of $\sigma_y(\tau = 1s) \approx 4.7 \times 10^{-13}$ for 30 mW of laser power incident on the vapor cell. By varying the laser power and the resulting error signal magnitude, the frequency standard's performance is confirmed to be limited by shot noise on the PMT signal. However, the calculated shot noise based on the mean PMT photo-current is a factor of 2 smaller, indicating the PMT has an effective noise factor of 1.5 dB, which is consistent with the description in Ref. [65].

Table 2.1: Typical parameters related to the short-term stability of the frequency standard as defined in the main text.

Parameter	Typical value
Detection rate	3.7×10^{7}/s
S_v	8.8×10^{-9} V^2/Hz
g_{PD}	0.41
V_e	0.065 V
$\Delta\nu$	608 kHz
Effective SNR (10 kHz bandwidth)	22
σ_y (1 s)	4.7×10^{-13}
$S_y^{(LO)}$ [$2f_m = 260$ kHz]	2.7×10^{-27}/Hz

2.6 Instability coefficients

Collection of several environmental variables and calculation of the expected Allan variance is an important tool to assessing clock performance. Detailed in this section is the measurement of the instability coefficents.

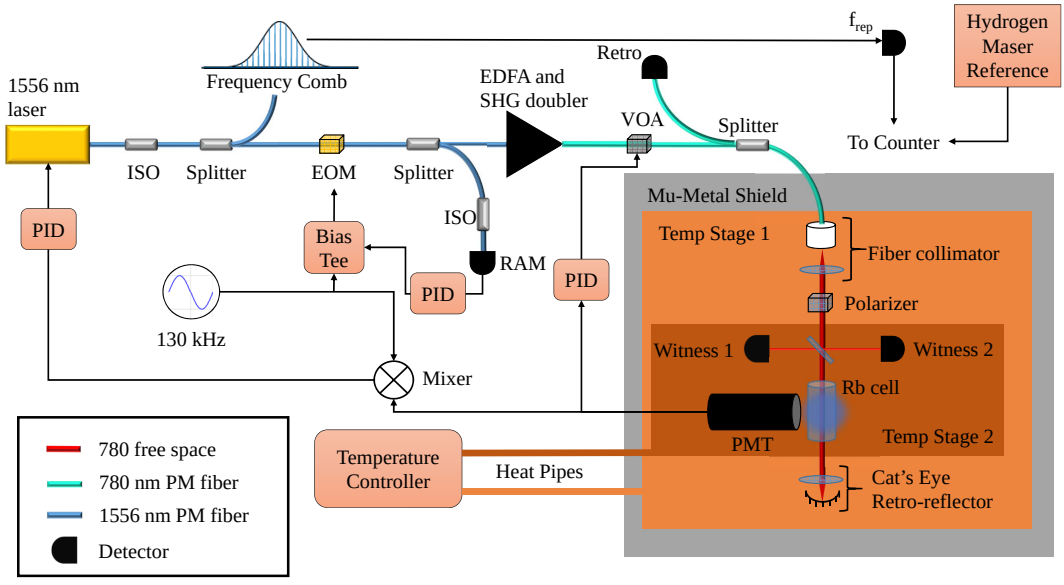

Figure 2.12: An optical and simplified electrical schematic of the Rb two-photon frequency standard as described in the text. EOM - electro-optic modulator; PMT - photomultiplier tube; VOA - variable optical attenuator; ISO - optical isolator; EDFA - erbium doped fiber amplifier; SHG - second harmonic generator; RAM - residual amplitude modulation; PID - proportional integral differential lock mechanism. Figure originally presented in [92].

2.6.1 Collisional Shifts

Collisions between two rubidium atoms can perturb the ground and excited state electronic wavefunctions, in principle leading to both a density-dependent collisional shift and a spectral line-broadening. While exact details of these processes, which depend on the Rb-Rb molecular potentials, have not been published, Ref. [146] reported that line broadening is insignificant for this system so long as the vapor cell is operated below 125 °C, and further reported a collisional shift coefficient in fractional frequency of 3.5×10^{-8}/Torr. Practically speaking, this places a tight constraint on the temperature stability of the vapor cell, which effectively controls the saturated vapor density.

The vapor cell temperature was determined using a standard 100 ohm resistive temperature detector (RTD) four wire measurement, with a duplicate device for out-of-loop monitoring. Generally thought to be slow, RTDs provide less drift from thermal aging than thermistors and higher precision than thermocouples. The slow responsiveness for RTDs is not a concern as the vapor cell clamshell has significant thermal mass and a four wire measurement eliminates the temperature instability from lead resistance. Two independent temperature control stages were designed, a 333 K plate (temperature stage 1 in Figure 2.12), to provide a stable reference temperature for heat transfer control, and a second, more finely controlled 373 K stage (temperature stage 2) upon which the vapor cell was mounted (see Figure 2.12). These stages were separated by four G-11 fiberglass posts to provide conductive thermal isolation. A SRS PTC-10 precision temperature controller regulated a thermoelectric device and closed the temperature servo loops. Fiberglass insulation was added around the temperature control stages to reduce convective heat loss while the system was operated in an open air laboratory environment.

The collisional shift for a ^{87}Rb enriched vapor cell was measured by varying the vapor cell temperature. For each temperature change the system was allowed to

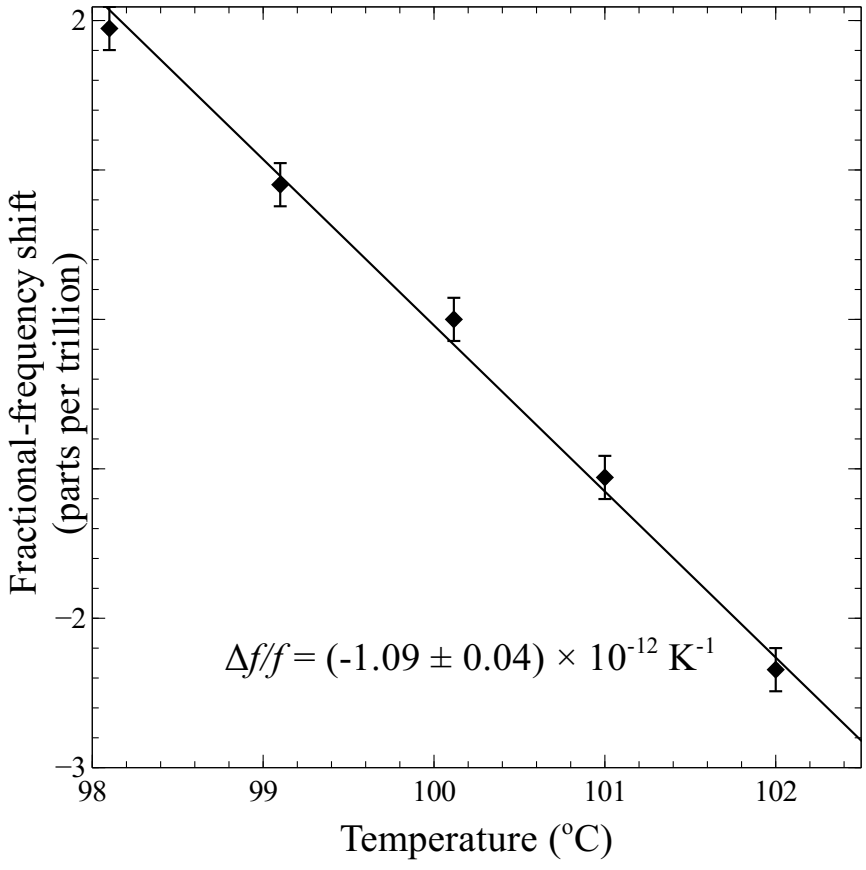

Figure 2.13: The normalized fractional frequency as a function of vapor cell temperature. Figure originally presented in [92].

thermalize, whereupon the resulting frequency shift was measured over 300 s. The obtained frequency vs. temperature is plotted in Figure 2.13, and the fit supports a clock shift of $-1.09(4) \times 10^{-12}$/K, which is a factor of 2 larger than reported for ^{85}Rb by Zameroski *et al.* [146] in a vapor cell with natural Rb.

While this discrepancy could, in principle, be due to isotope-dependent collision shift coefficients, it could also be due to non-collisional effects that were also varied when the cell temperature was changed, such as servo errors. Regardless, the measurement performed here accurately characterizes the system's sensitivity to vapor

cell temperature; at 373 K the temperature must be stable to 0.92 mK to achieve a fractional frequency stability of 1×10^{-15}.

Experimentally determined collisional shifts in [146] for various noble gases were examined to put limits on vapor cell impurities. Helium is the only gas known to permeate the vapor cell, and it produces frequency shifts of –2.1 MHz/Torr. Therefore, a helium leak rate of $< 3.6 \times 10^{-8}$ Torr/day must be achieved in order to achieve fractional clock instabilities below 1×10^{-15}. The cell may also be permeable to methane, which has an atmospheric composition of about three times less than helium, but no measure of this shift rate could be found.

Helium diffusion through glass

All vapor cells have glass or crystal windows necessary for spectroscopy. Since these materials are permeable to helium, even at room temperature, atomic line broadening and shifts arising from collisions with helium can be problematic. There are a few solutions: actively pump the helium from the system, never let the helium enter the cell to begin with, or wait until the helium in the cell is in steady state and accept the line broadening. Manufacture of vapor cells impermeable to helium is an active area of research and requires specialty glasses, proper vapor cell material baking and specialty bonding techniques [40]. To simplify manufacturing of the O-RAFS system, vapor cells were purchased from local suppliers, constructed with either borosilicate or fused silica glasses. Unfortunately, both of these glasses are known to be permeable to helium. Initial tests of the O-RAFS system were performed in an open air environment with the Rb transition broadened by 4 mTorr of residual helium. Final tests of O-RAFS stability will require that the system be moved to a high vacuum environment to reduce convective heat transfer between the room and experiment and are described in Chapter 3. Knowing the expected clock shift of a slow leak of helium is important for final analysis, as well as approximations of how

long the helium will remain in the cell.

Consider a volume of helium with a permeable partition separating gas at internal pressure, p_i, and external pressure, p_e. Diffusion of helium through the glass partition can be described fully by knowing the difference in pressure, geometry of the window, and the solubility, S, and diffusion constants, D, of the glass. The pressure change as gas leaks into a vapor cell of volume V, area A, and thickness d is is solved in Refs [5, 40, 114, 133]. However, the boundary conditions used to solve this problem are not correct in our case. Refs [5, 40, 114, 133] solved for the case where the helium on the outside of the vapor cell was constant. They also solved the diffusion equation in the short time limit where there was no measurable helium in the vapor cell. A solution for the diffusion equation with the following boundary conditions is required:

1. The helium number density outside the vapor cell is zero for all time.
2. There exists a finite number of helium atoms inside the vapor cell.
3. At time t=0 the vapor cell glass is saturated with helium.

Refs. [31, 38] solved this problem, yielding slightly different answers. However, in the *lumped capacitance* approximation the answers agree. The *lumped capacitance* usually is used in reference to a thermal mass, this approximation states that temperature gradients across the mass are negligible. In the case of diffusion of a gas through glass the *lumped capacitance* approximation assumes the pressure gradients in the vapor cell are negligible. In this approximation the solution takes the form,

$$u(x,t) = u(x,0)e^{-\frac{DSA}{Vd}t}x. \tag{2.21}$$

For a fused quartz window 0.1 cm thick and surface area 5.5 cm^2 occupying a volume of 0.2 cm^3, the decay time can be calculated using the diffusion constants from Ref. [5]. The final system will be integrated into a vacuum chamber slowly driving the helium from the vapor cells, there will be only a small fraction of helium left in the vapor cell after 200 days.

2.6.2 Magnetic Field

Expressing the differential Zeeman sensitivities in fractional frequency units, we find the net clock shifts to be $6.5 \times 10^{-11}/\mathrm{G}^2$ for ^{87}Rb and $2.5 \times 10^{-10}/\mathrm{G}^2$ for ^{85}Rb. The energy level splitting diagram for the exited states of ^{87}Rb and ^{85}Rb are shown in Figure 2.6 and 2.7. With these coefficients, we can now specify the magnetic shielding requirements; for ^{87}Rb (^{85}Rb), the magnetic field should be stable at the 3.9 mG (2.0 mG) level. To reduce the magnetic field at the vapor cell a rectangular μ-metal shield of thickness 5 mm was installed for which the expected shielding factor exceeds 1000. In practice, the shielding factor is reduced to due to openings for the heat pipes, optical fiber, electrical cabling, and PMT, but nonetheless the residual magnetic field at the vapor cell is expected to be ≤ 1 mG.

2.6.3 Relativistic Doppler

The use of degenerate, counter-propagating beams eliminates non-relativistic Doppler broadening. However, an atom moving at velocity v will see a relativistic Doppler shift of the incident laser frequency, f_s, given by,

$$f_o = \gamma(1-\beta)f_s, \tag{2.22}$$

where $\gamma = (1-\beta^2)^{-1/2}$ and $\beta = v/c$. For a two photon transition the atom will see a Doppler shifted frequency from the incident and retro-reflected beams, where the relative velocity between the atom and these two lasers differ by a sign,

$$f_{o,I} + f_{o,R} = f_s\gamma\Big[1-\beta_L + 1-\beta_R\Big], \tag{2.23}$$

where the I and R subscripts denote the incident or retro-reflected signal and $\beta_I = -\beta_R$. Simplification of 2.23 and utilizing the binomial expansion to second order in β yields

$$\frac{f_{o,I}+f_{o,R}}{2f_s} = 1 + \frac{1}{2}\beta^2. \tag{2.24}$$

The average velocity of a 3 dimensional gas with temperature T, mass m can be approximated, $\bar{v}^2 = 8k_bT/m\pi$. The final relativistic Doppler shift for a Doppler free two-photon transition is then

$$\frac{f_{o,I} + f_{o,R}}{2f_s} = 1 + \frac{4k_bT}{\pi mc^2}. \tag{2.25}$$

For Rb at 373 K the fractional clock shift is 5×10^{-13} with a slope of 1×10^{-15}/K.

2.6.4 Line-pulling

The two Lorentzian curves shown in Figure 2.14 illustrate a phenomena known as line pulling. The spectral line on the left is the simulated clock transition, and the spectral line on the right is another atomic transition not of interest but whose mere existence moves the main spectral line slightly to the right. The picture is described by the function $G(f)$,

$$G(f) = \frac{A}{\pi}\frac{\frac{1}{2}\Gamma_1}{(f-f_0)^2 + (\frac{1}{2}\Gamma_1)^2} + \frac{B}{\pi}\frac{\frac{1}{2}\Gamma_2}{(f-f_0-\delta)^2 + (\frac{1}{2}\Gamma_2)^2}, \tag{2.26}$$

where A and B are parameters that describe the relative strengths of the Lorentzians. Although the peak of the main Lorentzian is found at f_0 the maximum of the function $G(f)$ is no longer located there. To find the local maximums of the function the derivative with respect to frequency can be written,

$$\frac{dG(f)}{df} = -\frac{A}{\pi}\frac{\frac{1}{2}\Gamma_1 2(f-f_0)}{\left[(f-f_0)^2 + (\frac{1}{2}\Gamma_1)^2\right]^2} + \frac{B}{\pi}\frac{\frac{1}{2}\Gamma_2 2(f-f_0-\delta)}{\left[(f-f_0-\delta)^2 + (\frac{1}{2}\Gamma_2)^2\right]^2}. \tag{2.27}$$

To make this equation more simple some estimations are needed. the following assumptions will be used in the derivation:

$$\frac{f-f_0}{\frac{1}{2}\Gamma_1} << 1, \quad \frac{f-f_0}{\delta} << 1 \quad \text{and} \quad \frac{\Gamma_2}{\delta} << 1 \tag{2.28}$$

Rearranging Equation 2.27 yields,

$$\frac{dG(f)}{df} = -\frac{A}{\pi}\frac{\frac{1}{2}\Gamma_1 2(f-f_0)}{(\frac{1}{2}\Gamma_1)^4\left[\frac{(f-f_0)^2}{(\frac{1}{2}\Gamma_1)^2} + 1\right]^2} + \frac{B}{\pi}\frac{\frac{1}{2}\Gamma_2 2(f-f_0-\delta)}{\delta^4\left[\frac{(f-f_0)^2}{\delta^2} + 1 - 2\frac{(f-f_0)}{\delta} + \frac{(\frac{1}{2}\Gamma_2)^2}{\delta^2}\right]^2}. \tag{2.29}$$

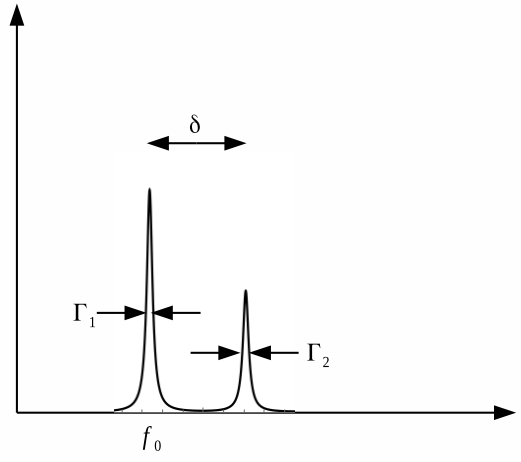

Figure 2.14: Two Lorentzian curves to help illustrate line pulling

Only keeping first order terms in the small variables yields,

$$\frac{dG(f)}{df} \approx -\frac{A}{\pi}\frac{\frac{1}{2}\Gamma_1 2(f-f_0)}{(\frac{1}{2}\Gamma_1)^4} + \frac{B}{\pi}\frac{\frac{1}{2}\Gamma_2 2(f-f_0-\delta)}{\delta^4\big[1-2\frac{(f-f_0)}{\delta}\big]^2}. \tag{2.30}$$

Employing the binomial expansion to further simplify the equation, again only keeping first order terms, yields,

$$\frac{dG(f)}{df} \approx -\frac{A}{\pi}\frac{2(f-f_0)}{(\frac{1}{2}\Gamma_1)^3} + \frac{B}{\pi}\frac{\Gamma_2(f-f_0-\delta)}{\delta^4}\big[1+4\frac{(f-f_0)}{\delta}\big]. \tag{2.31}$$

The final transition frequency of the system illustrated in Figure 2.14 is,

$$f = f_0 + \frac{\frac{B}{A}\Gamma_2}{\delta^3\left[\frac{2}{(0.5\Gamma_1)^3} - \frac{B}{A}\frac{3\Gamma_2}{\delta^4}\right]}. \tag{2.32}$$

The amount by which a particular transition is shifted can calculated by summing over all relevant hyperfine Lorentzians with appropriate frequencies and strengths given by Ref. [99]. This can be done numerically or using the derived approximation. The two-photon transition is shifted by 0.477 Hz for ^{85}Rb and 0.030 Hz for ^{87}Rb. This calculation does not take into account possible cross-damping terms, which can arise from quantum interference between multiple decay paths associated with neighboring, off-resonant transitions [143].

2.6.5 Stark shift

Although many environmental variables impact the clock instability of O-RAFS, the inherently large ac-Stark shift motivates the most difficult requirements. Careful calculation and direct measurement of the ac-Stark shift magnitude are pivotal to understanding the overall impact on clock performance. The ac-Stark shift can be written as [58],

$$\delta\nu\left(r\right) = \frac{\Delta\alpha}{2c\epsilon_0 h} I\left(r\right), \tag{2.33}$$

where $I\left(r\right)$ is the laser intensity, and $\Delta\alpha$, the differential atomic polarizability will need to be calculated.

The rank-2 atomic polarizability tensor can be separated into three irreducible components: the scalar (trace), the vector (free symmetric) and the tensor (anti-symmetric) polarizabilites. The two-photon transition is pumped with linearly polarized light, yielding zero vector shift, and each hyperfine state is addressed uniformly, leaving the atom orientation independent, netting zero tensor shift. The only term in the atomic polarizability tensor that results in a ac-Stark shift is the scalar term, written below in atomic units [42, 130],

$$\alpha\left(\omega, J\right) = -\frac{2}{3\left(2J+1\right)} \sum_{J'} \frac{\omega_{J',J} |\langle J|d|J'\rangle|^2}{\omega_{J',J}^2 - \omega^2}, \tag{2.34}$$

where $\langle J|d|J'\rangle$ is the dipole matrix element and J is the angular quantum number for the ground state of the two-level system in question.

In general it is necessary to sum over all allowed $J \to J'$ transitions to calculate the polarizability of the state $\alpha(\omega, J)$, however, as $\omega_{J',J}$ approach ionization the contribution to the total polarizability is negligible. Table A.4 summarizes the states included in the polarizability calculation displaying the transition energy difference, the dipole matrix elements, and the Einstein A coefficients calculated from Equation 2.16 (unless stated otherwise) [35, 45, 64]. A large number of the parameters listed in Table A.4 originate from Safronova *et al.* [118], however, the $5S_{1/2} \to 5P_{1/2}$ and $5S_{1/2} \to 5P_{3/2}$ dipole matrix elements are calculated utilizing measured Einstein A coefficients [112].

Another three matrix elements, $5D_{5/2} \to 9F_{7/2}$, $5D_{5/2} \to 9F_{5/2}$ and $5D_{5/2} \to 12P_{3/2}$, are calculated utilizing quantum defect theory; generalizing that energy deviations from the Rydberg atom can be written,

$$E = \frac{A}{(n-d)^2}, \tag{2.35}$$

where, E is the energy, n is the principle quantum number, d is the quantum defect. Equation 2.35 can be used to calculate the energies and thus the transition frequencies subtracting the result from the Rb ion limit in [119]. Necessary elements for the calculation are the Rydberg constant substituted for A from [97] and the defects for Rb which are 3.13 for S states, 2.64 for P states, 1.35 for D states and 0.016 for F states [56]. Under the assumption that the dipole matrix elements follow the same form as Equation 2.35, where now E is the dipole matrix element and A and d are free fitting parameters a least square regression was performed on the existing data sets. The linear regression yields: $A = 79.1 \pm 4$ and $d = 2.38 \pm 0.04$ with residuals of 0.2 for $nF_{7/2}$, $A = 17.7 \pm 0.9$ and $d = 2.38 \pm 0.04$ with residuals of 0.05 for $nF_{5/2}$, and $A = 14.3 \pm 1.6$ and $d = 5.98 \pm 0.06$ with residuals of 0.2 for $nP_{3/2}$. These fitting parameters were used to generate the three dipole matrix elements and were included

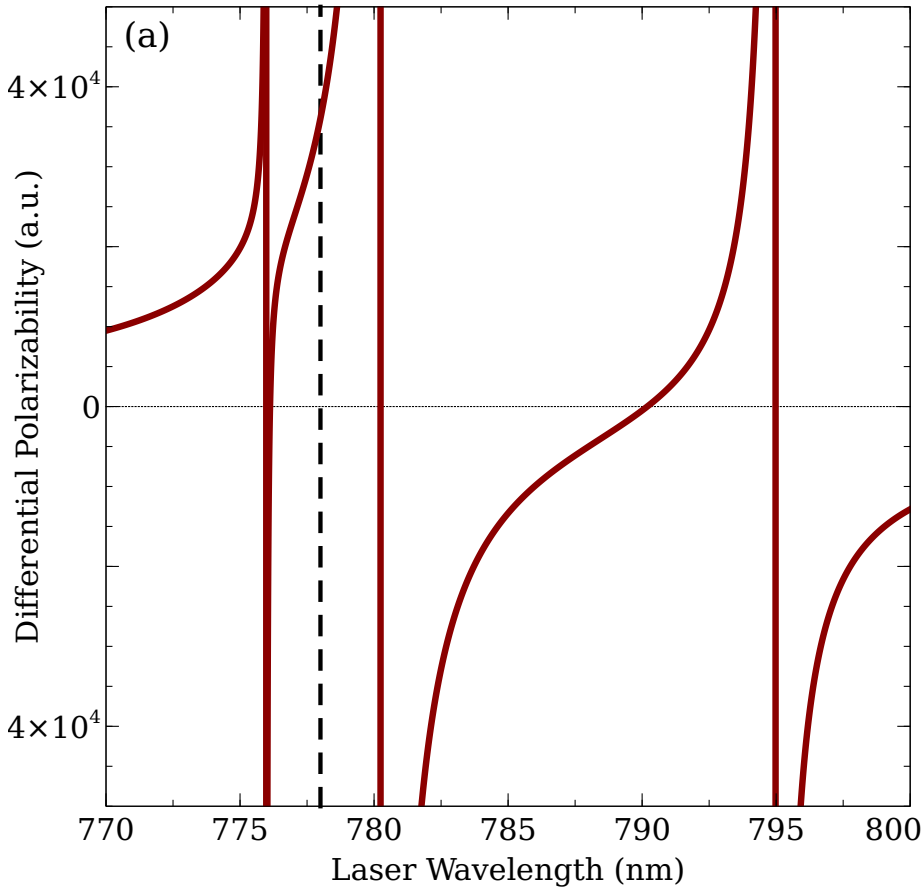

Figure 2.15: The differential polarizability of the $5S_{1/2} \rightarrow 5D_{5/2}$ transition as a function of wavelength displayed in atomic units as calculated by Equation 2.34.

in the total calculation of the ac-Stark shift, yet the polarizability of the excited state arising from these calculation only make up ≈0.34 % of the total value.

The differential polarizability was calculated for a range of incident wavelengths shown in Figure 2.15. Calculation of the ac-Stark shift at 778.1 nm yields a fractional frequency shift of 2.3×10^{-13} /(mW/mm^2). This calculation can be confusing, it is important to note that each 778.1 nm photon carries one half of the transition shift: $\Delta\omega_{778} = \left(\Delta\omega_{5D_{5/2}} - \Delta\omega_{5S_{1/2}}\right)/2$, and it is this that imposes the limit on intensity stability of the incident light. ‘

Combining equations 2.33 and 2.34 yields a Stark shift dependence on local intensity of the laser electric field. Although O-RAFS is sensitive to local fluctuations of laser intensity, only the effective average intensity of the laser is measured. The average Stark shift,

$$\overline{\delta\nu\left(r\right)} = \frac{\Delta\alpha}{2c\epsilon_0 h}\overline{I_{tot}\left(r\right)}, \tag{2.36}$$

requires the spatial weighted average intensity,

$$\overline{I_{tot}} = \frac{\int I_{tot} I_1 I_2 dV}{\int I_1 I_2 dV}, \tag{2.37}$$

with the total intensity as the sum of the two curves $I_{tot} = I_1 + I_2$. The weighting function $I_1 I_2$ is a proxy for the two photon excitation rate, the main contributor to the ac-Stark shift. This weighted average of the two-photon intensity is the desired clock shift parameter necessary for laser intensity fluctuation driven clock instabilities. Equation 2.36 details that changes in laser intensity field will cause a clock shift. Variations in the total laser intensity can be caused by not only laser power fluctuations but also by slight alignment variations.

Alignment Calculation

Typical optic mounts allow slight tip/tilt adjustments which are required for control of the beam. In the O-RAFS system, variations in alignment affect the total intensity of the two-photon excitation causing an ac-Stark instability. This section examines slight angular variations of the laser light emitted from the fiber launcher, as well as slight variation of the retro-reflector, and calculates the associated ac-Stark shift. Figure 2.16 presents what a small angular misalignment would look like for both a flat mirror (a) and a cat eye retro-reflector (b). These two separate retro-reflectors have been successfully integrated in the experimental apparatus. The optimal retro-reflector necessary to reduce the alignment induced ac-Stark shift effects can be determined through calculation of Equation 2.37.

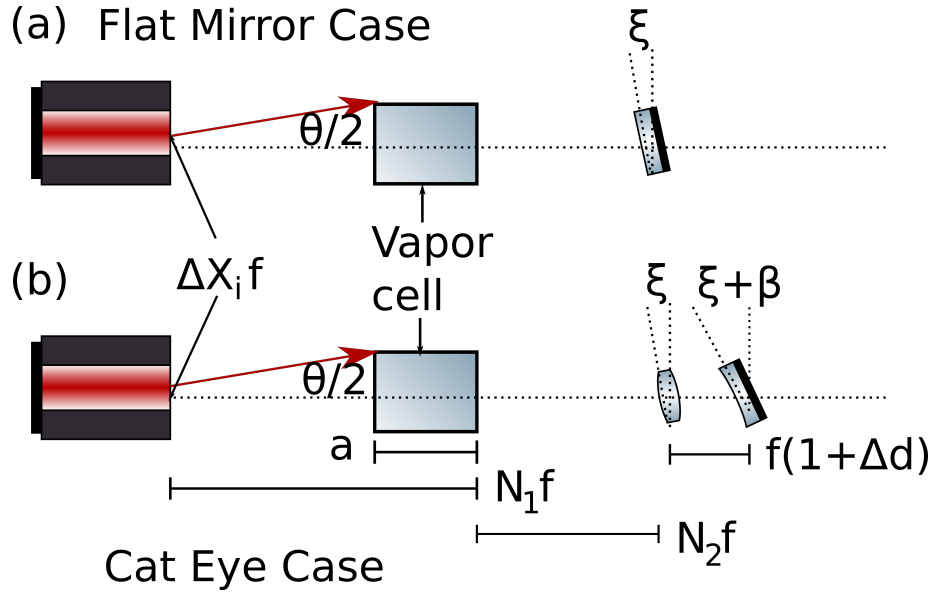

Figure 2.16: Simple geometric alignment diagram for a flat mirror (a) and a cat eye (b). In each case all distances were written in terms of the focal length of the lens utilized in the cat eye: N_1,N_2,Δd,Δf ΔX_i are unit-less parameters. ΔX_if - displacement of the initial Gaussian beam from the optical axis, θ - angular misalignment of the initial beam, ξ - angular misalignment of the retro-reflecting optic, β - angular misalignment of the mirror and lens in the cat eye optic, fΔd - displacement from optimal placement of the mirror in the cat eye optic, N_1f - distance from the fiber launcher to the rear of the vapor cell, N_2f - distance from the vapor cell to the retro-reflector, a -vapor cell length and fΔ f - absolute deviation of the cat eye mirror from optimal radius of curvature.

Normally, the intensity of a Gaussian beam after interaction with a series of optical components can be calculated using the ABCD or M matrices and the Gaussian q- parameter formulation [124, 130]. However, the M matrices require that the optical elements are placed normal to the optical axis, which is not true for a general case. The extended ray trace matrices can be leveraged [124] (see Table 2.2),

$$\begin{pmatrix} A & B & \delta \\ C & D & \gamma \\ 0 & 0 & 1 \end{pmatrix}, \tag{2.38}$$

where δ is a displacement from the optical axis, γ is a rotation of the optic from

Table 2.2: The extended ray trace matrices used to calculate misalignment effects from the cat eye optic

Freespace propagation of distance N	$\begin{pmatrix} 1 & N & 0 \\ 0 & 1 & 0 \\ 0 & 0 & 1 \end{pmatrix}$
Thin lens with focal length f at angle ξ	$\begin{pmatrix} 1 & 0 & 0 \\ -1/f & 1 & \xi \\ 0 & & 1 \end{pmatrix}$
Concave mirror, radius $f(1+\Delta f)$, at angle $\xi+\beta$	$\begin{pmatrix} 1 & 0 & 0 \\ 2/f(1+\Delta f) & 1 & \xi+\beta \\ 0 & 0 & 1 \end{pmatrix}$
Flat mirror, at angle ξ	$\begin{pmatrix} 1 & 0 & 0 \\ 0 & 1 & \xi \\ 0 & 0 & 1 \end{pmatrix}$

normal incidence, and the ABCD elements are unchanged.

In the flat mirror case, the Gaussian beam originating from the fiber launcher can be written as,

$$I_{incident} = I_0 e^{-2(x^2+y^2)/w_0^2}. \tag{2.39}$$

The extended M matrix for the beam as it re-enters the vapor cell after reflection off the mirror is,

$$M = \begin{pmatrix} 1 & 2N_2 f & N_2 f\xi \\ 0 & 1 & \xi \\ 0 & 0 & 1 \end{pmatrix}. \tag{2.40}$$

The Gaussian q parameter [124, 130],

$$q = q_1 + iq_2 = \frac{Aw_0^2\pi i/\lambda + B}{Cw_0^2\pi i/\lambda + D}, \tag{2.41}$$

can be used to to determine the retro reflected beam characteristics as it re-enters the cell. Substituting the parameters from Equation 2.40 yields,

$$q = w_0^2\pi i/\lambda + 2N_2 f, \tag{2.42}$$

where, λ is the wavelength and w_0 is the beam waist. Calculating the retro-reflected beam from these q-parameters and using the approximation that the free space propagation lengths are less than the Rayleigh length and thus $(q_1/q_2) << 1$, yields,

$$I_{retro} = I_0 e^{-2(x^2+y^2+2x(N_2 f+z)(\xi-\theta)+(N_2 f+z)^2(\xi-\theta)^2)/w_0^2}, \tag{2.43}$$

for the retro-reflected beam. Equation 2.37 is calculated and the normalized weighted average, $\overline{I}$, is given by,

$$\frac{\overline{I_{tot}}}{\overline{I_{tot}}(\xi=\theta)} = \frac{\sqrt{3}}{2}\frac{\mathrm{erf}\left(2(y_1+y_2)/\sqrt{3}\right) - \mathrm{erf}\left(2y_2/\sqrt{3}\right)}{\mathrm{erf}\left(y_1+y_2\right) - \mathrm{erf}\left(y_2\right)}, \tag{2.44}$$

where $y_1 = a\left(\xi-\theta\right)/\omega_0$ and $y_2 = Mf\left(\xi-\theta\right)/\omega_0$. This result is plotted in Figure 2.17 for the experimental set-up described in Section 2.4. The M matrix formulation already leverages the small angle approximation where, $\xi, \theta << 1$. Applying this approximation to Equation 2.44 the weighted average becomes,

$$\overline{I} \approx 1 - \frac{\left(a^2 + 3aN_2 f + 3N_2^2 f^2\right)\left(\xi-\theta\right)^2}{9\omega_0^2}, \tag{2.45}$$

which has been expanded to second order in θ, ξ and their cross terms.

The final desired quantity is the sensitivity of the average weighted total intensity to angular misalignment in each optic, or the derivative of the intensity w.r.t. the angular variable. Taking the derivative of Equation 2.45 w.r.t. either θ or ξ yield the same result,

$$\frac{d\overline{I}}{d\theta} \approx \frac{-2\left(a^2 + 3aN_2 f + 3N_2^2 f^2\right)\theta}{9\omega_0^2}. \tag{2.46}$$

The cat eye calculation is more challenging. A cat eye retro-reflector consists of a convex lens with a focal length f, and a concave mirror with a radius of curvature f, placed at the focus of the lens. An ideal cat eye provides an anti-parallel retro-reflected beam [128], whereas misalignment in the fiber launcher will yield non-parallel beams in the case of a flat mirror reflector. Although the incident beam can be recycled and the q-parameter formulation is the same, the M matrix becomes more complex. Various misalignment mechanisms in the cat eye optic calculation, shown

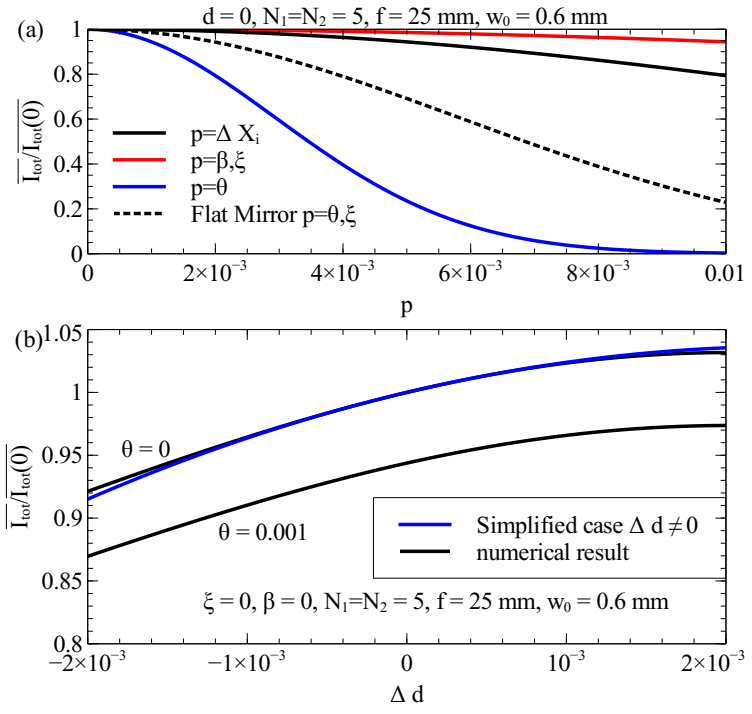

Figure 2.17: Shown in (a) is the simplified case where $\Delta d = 0$. Clearly, the fiber launcher angle is more sensitive than the other misalignment variables in the cat eye case and either angular misalignment in the flat mirror case. Shown in (b) is the numerically calculated average intensity as a function of Δd for incident angular misalignment of $\theta = 0$ and $\theta = 0.001$ for $\Delta d \neq 0$ as well as the simplified case where $\Delta X_i = 0$, $\beta = 0$ and $\Delta f = 0$. Over a half percent change in cat eye optic displacement Equation 2.50 holds

in Figure 2.16, include small deviations of the location of the mirror, now located at $f(1 + \Delta d)$, and radius of curvature of the mirror, $f(1 + \Delta f)$, while also allowing for the lens and mirror to have a misalignment angle β between them. The following assumptions are enforced: $\xi << 1$, $\theta << 1$, $\Delta d << 1$, $\Delta f << 1$, $\Delta X_i << 1$, $\beta << 1$ and the initial beam is collimated.

Calculation of the intensity weighted average for the cat eye case requires the Gaussian beam profile of the retro-reflected beam. After retro-reflecting off of the cat eye the beam re-enters the vapor cell with the following M matrix parameters:

$$\begin{pmatrix} X_f \\ Y_f \\ 1 \end{pmatrix} = \frac{1}{1+\Delta f} \begin{pmatrix} A & B & E \\ C & D & F \\ 0 & 0 & 1+\Delta f \end{pmatrix} \begin{pmatrix} f\Delta X_i \\ \theta \\ 1 \end{pmatrix},$$

where,

$$\begin{aligned}
A =& -(1+\Delta f - 2\Delta d(N_2 + \Delta d - N_2\Delta d + (N_2-1)\Delta f))),\\
B =& f(2(\Delta d - N_2(\Delta d - 1))((N_2-1)\Delta d - 1) + (2\Delta d(N_2 + \Delta d - N_2\Delta d) - 1)N_1\\
&+ (2(N_2-1)((N_2-1)\Delta d - 1) + (2(N_2-1)\Delta d - 1)N_2)\Delta f),\\
C =& -(-1 + (N_2-1)\Delta d)f((2\Delta d - 3\Delta f - 1)\xi - \beta(1+\Delta f)),\\
D =& \frac{2\Delta d(1 - \Delta d + \Delta f)}{f},\\
E =& -(1+\Delta f - 2\Delta d(N_2 + \Delta d - N_2\Delta d + N_1 - \Delta d N_1 + \Delta f(N_1 + N_2 - 1))),\\
F =& \Delta d(\xi - 2\Delta d\xi + 3\Delta f\xi + \beta + \Delta f\beta).
\end{aligned}$$

Here we utilize the same approximation as the flat mirror case, namely that all distances are much shorter than the incident beam Rayleigh length. Even leveraging this approximation yields a complicated Gaussian function. In order to simplify the analytical solution a few special cases were examined.

1. Setting $\Delta d = 0$ yields

$$\frac{\overline{I_{tot}}}{\overline{I_{tot}}(0)} = e^{\frac{-f^2(2x_i(1+\Delta f)+\xi+3\Delta f\xi+\beta+\Delta f\beta+(N_1+N_2)\theta-\Delta f\theta+(N_1+N_2)\Delta f\theta)^2}{3(1+\Delta f)^2 w_0^2}}. \tag{2.47}$$

   Figure 2.17 shows the variation on average intensity as a function of ΔX_i, β, ξ, and θ with all other misalignment variables set explicitly to zero. The fiber launcher angular sensitivity dominates. As in the flat mirror case the sensitivity of the average intensity w.r.t. angular misalignments of the fiber launcher and retro-reflector is the desired quantity. In the cat eye case these solutions differ,

$$\frac{d\overline{I}}{d\theta} \approx \frac{-2f^2\,(N_1+N_2)\,(\xi + (N_1+N_2)\,\theta)}{3\omega_0^2} \tag{2.48}$$

$$\frac{d\overline{I}}{d\xi} \approx \frac{-2f^2\left(\xi + \left(N_1 + N_2\right)\theta\right)}{3\omega_0^2} \tag{2.49}$$

where, $\Delta f = 0$, $\beta = 0$, and $\Delta X_i = 0$. By design, the cat eye suppresses angular motion of the retro-reflector optic over the flat mirror, but at the expense of sensitivity to angular misalignment of the fiber launcher. Equations 2.48 and 2.49 can be found by taking proper derivatives of Equation 2.47

2. A numerical integral was performed using the Gauss Kronrod quadrature method [37]. The numerical result is displayed in Figure 2.17 (b).

3. A mapping exists between changes in ΔX_i and θ, as well as between β and Δd, finally Δf is known to have small impacts on the retro-reflected beam profile [128]. With this in mind another analytical case was examined where $\Delta X_i = 0$, $\Delta f = 0$ and $\beta = 0$. It was also necessary to expand the integrand in a Taylor series and ignore the higher order terms before final integration yielding an average intensity of,

$$\begin{aligned}\overline{I} \approx & 1 - \frac{f^2\xi^2 + 2f^2\xi\theta\left(N_1 + N_2\right)\theta^2 f^2\left(N_2^2 + 2N_2N_1 + N_1^2\right)}{3\omega_0^2} + \\ & + \Delta d\left(4N_2 + \frac{a}{f} + 2N_1\right) + \Delta d^2\left(4 - 4N_2 + \frac{88N_2^2}{9} + \frac{37a^2}{27f^2} - \frac{a}{f} + \frac{40aN_2}{9f}\right) \\ & + \Delta d^2\left(-2N_1 + \frac{32N_2N_1}{3} + \frac{4aN_1}{3f} + 4N_1^2\frac{2\pi^2\omega_0^4}{f^2\lambda^2}\right).\end{aligned} \tag{2.50}$$

Taking the derivative of the above Equation w.r.t. either θ or ξ yields the same result when $\Delta d = 0$. Figure 2.17 (b) shows average intensity given above plotted for a specific case along with the numeric results for the same case study.

Careful examination of alignment shows that the cat eye retro-reflector helps reduce sensitivity of the average intensity to variations in the retro-reflecting optic over

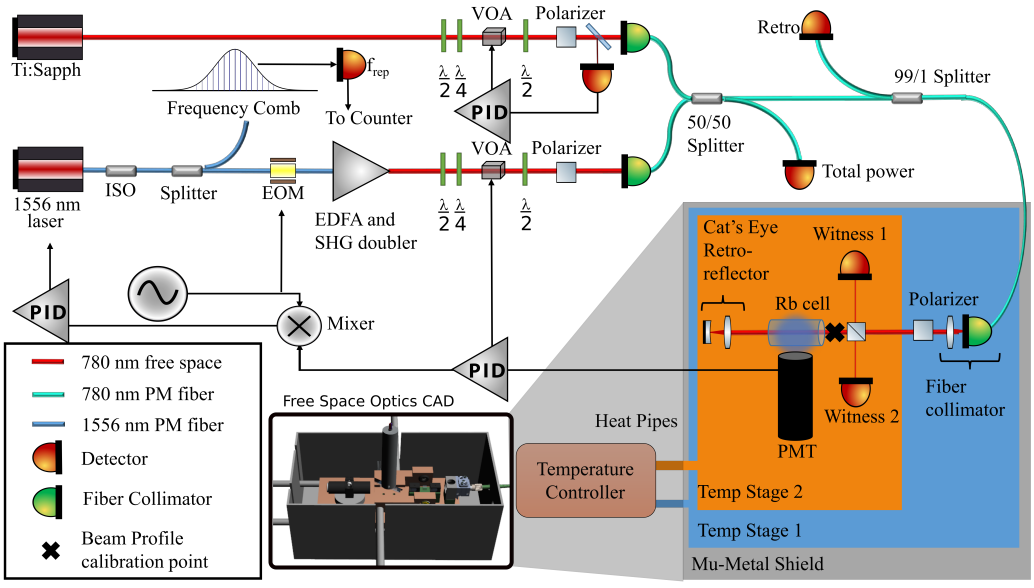

Figure 2.18: A optical and simplified electrical schematic of the Rb two-photon frequency standard as described in the text.

the flat mirror reflector. However, the cat eye retro-reflector increases the sensitivity of the average intensity to angular misalignments of the fiber launcher, and introduces another very sensitive misalignment variable, the distance between the lens and mirror in the cat eye optic. While effort can be placed to reduce the dynamic response of the displacement Δd, care must be taken to ensure that the average intensity signal is maximized during initial alignment. For a dynamic system, however, the flat mirror retro-reflector might be the best choice to reduce complexity/sensitivity to motion. Ultimately, any effort to further reduce the overall ac-Stark shift will also reduce Stark shift related alignment sensitivities.

Measurement

Measuring the ac-Stark shift is important to confirm the accuracy of the theoretical result. An experiment was designed specifically to measure the effects of the

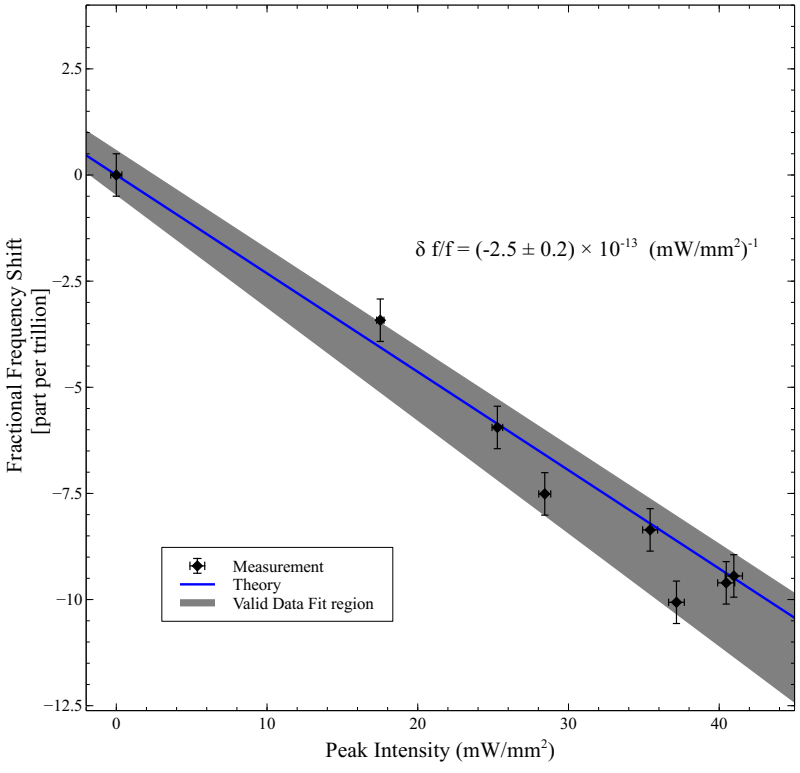

Figure 2.19: Experimentally measured 778 nm ac-Stark shift for a (0.66 ± 0.05) mm beam. The fit (shaded region) used was orthogonal distance regression (ODR) which weights error bars in x and y data yielding a reduced χ^2 of 1.57. The calculated ac-Stark shift is also shown in blue.

ac-Stark shift on the output clock frequency. Two lasers were utilized in the Stark shift measurement (Figure 2.18): the clock laser described in Section 2.4.3, and a Ti:Sapph laser tuned slightly away from the two-photon resonance to 385287.8 GHz, a 2 GHz detuning is far enough from the resonant two-photon excitation frequency to introduce no measurable vapor excitation. The clock laser is tuned to be on resonance with the two-photon transition, described in Section 2.4.3. After amplification and subsequent second harmonic generation of 778.1 nm, the clock laser and the Ti:Sapph laser separately pass through a half wave-plate followed by a quarter wave-plate. The remaining light in each beam is subsequently sent through a VOA,

which is used for laser power stabilization. Each beam then passes through another half wave-plate and polarizer, properly aligning the polarization to fiber couple each beam into two separate arms of a polarization maintaining (PM) 2×2 50:50 fiber splitter. A portion of the Ti:Sapph light is sampled before fiber coupling. This signal is used for feedback to the Ti:Sapph VOA and stabilize the optical power coupled into the beam splitter. One arm of the splitter is sent to a detector used for independent power measurements. The second arm of the splitter is sent to the vapor cell assembly through a 2×2 99:1 PM fiber splitter. Up to 30 mW of Ti:Sapph light and 30 mW of clock laser light was delivered to the vapor cell assembly, described in [92].

The two witness photodiodes, Thorlabs SM05PD1A, and the forward going detector, Thorlabs PDA36A, on the 50:50 splitter were independently calibrated to both a Thorlabs PM160 and an Ophir PD300-TP silicon power meter at the 'X" marked in Figure 2.18. Differences in the calibrations are part of the systematic error which are included in the fit shown in Figure 2.19.

After the clock laser is stabilized to be on resonance, the Ti:Sapph laser power is varied using the VOA in its optical train. The frequency shifts are measured and averaged over 100 seconds and are reported in Figure 2.19. The data was fit with a orthogonal distance regression (ODR) algorithm which weights the error bars in both the x and y coordinates, yielding a fractional frequency fit of -2.5$\pm$0.2$\times 10^{-13}$ $(\mathrm{mW/mm^2})^{-1}$ with a reduced χ^2 of 1.57. A gray shaded region shows associated error with the fit. The theoretical value is plotted on the same curve and shows good agreement with the experimentally measured values.

Blackbody radiation shift

Plank's Law describes the electromagnetic radiation emanating from an object at temperature T. The time averaged intensity of the radiated field can expressed, [25],

$$\langle E(\omega)^2 \rangle = \frac{\hbar}{\pi^2 \epsilon_0 c^3} \frac{\omega^3}{e^{\hbar\omega/k_B T} - 1}. \tag{2.51}$$

An atom in a bath of electromagnetic radiation will experience an ac-Stark shift. Equation 2.51 describes an electromagnetic field whose intensity is dependent on the source temperature. Thus, fluctuating temperatures of a source that is radiatively coupled to the atoms can cause a clock shift via temperature driven ac-Stark interactions. The shift arising from blackbody radiation (BBR) can be calculated by,

$$\delta\nu = \frac{1}{2h} \int_0^\infty \Delta\alpha(\omega) E(\omega)^2 \, d\omega, \tag{2.52}$$

where $\Delta\alpha(\omega) = \alpha_e - \alpha_g$. Oftentimes, the resonance frequencies between atomic states connected to the ground and excited states involved in the clock transition are far from the blackbody spectrum. In this case the blackbody spectrum can be treated as a static polarizability field and Equation 2.52 can be simplified to be,

$$\delta\nu = \frac{\Delta\alpha}{2h} \int_0^\infty E(\omega)^2 \, d\omega \approx \frac{\Delta\alpha}{2h} \left(8.3 \frac{V}{cm}\right)^2 (T/300K)^4 . \tag{2.53}$$

Systems requiring higher precision include a small dynamic contribution, η, to account for frequency dependence [12,96,117]. Here, BBR is wideband and has significant overlap with the $5D_{5/2} \rightarrow 4F_{7/2,5/2}$ transitions in Rb at operational temperatures making it necessary to fully integrate Equation 2.52.

This integral was calculated numerically two separate ways. First, the polarizability was calculated using Equation 2.34 and the integral was performed using the Cauchy's principle value. The second method introduced the decay time of each transition [130],

$$\alpha(\omega, J) = -\frac{2}{3(2J+1)\hbar} \sum_{J'} \frac{\omega_{J',J} |\langle J|d|J'\rangle|^2 (\omega_{J',J}^2 - \omega^2)}{(\omega_{J',J}^2 - \omega^2)^2 + \Gamma_J^2 \omega^2}, \tag{2.54}$$

where Γ_j is the spontaneous decay rate. When the polarizability is written this way the function no longer diverges in the resonant cases. Equation 2.52 was then calculated with a deterministic adaptive integration technique. BBR shifts were

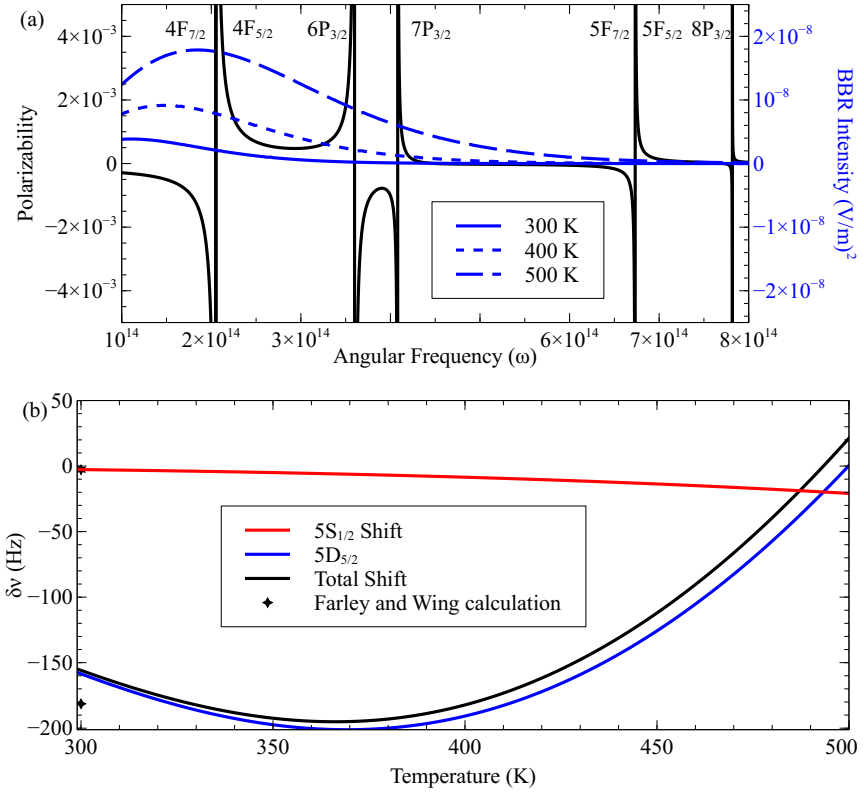

Figure 2.20: Shown in (a) blackbody radiation intensity (blue) at 300 K, 400 K and 500 K is shown with the excited state polarizability (black). Along the top of (a) are labeled the states connected to the excited state whose atomic transition is on resonance with the black body spectrum. (b) Shows the state shifts and the total BBR shift for the two-photon transition as a function of temperature.

examined under nominal operational conditions, specifically looking at the shifts produced in the temperature range of between 300 K and 500 K. The fractional difference for each of these calculations for both the excited state and ground state were less than 1×10^{-7}.

The resultant BBR shift of the ground state, $5S_{1/2}$, whose polarizabilities are far off resonance for the examined temperature range, yields a result that was consistent with the Farley *et al.* [50] calculations. The shift also is consistent with a T^4 temperature dependence and a static polarizability approximation. More interesting were

the results from integration over the excited state polarizabilities. The $5D_{5/2}$ state has resonant polarizablities in the temperature range of interest. Not only was the calculated ac-Stark shift no longer monotonic, the differential polarizability changed sign, see Figure 2.20. This result is not consistent with either a T^4 behavior or with the static polarizability approximation. The calculation yields two interesting 'magic" temperatures. Around 493 K $\delta\nu = 0$ and around 366 K $d\delta\nu/dT$=0. Clock operation hoping to achieve greater accuracy could operate around 493 K to eliminate the extra BBR shift while a clock hoping to achieve greater precision could operate around 366 K to suppress environmental temperature dependence. Greater precision and accuracy through these two magic temperatures is more difficult to achieve in practice. The vapor pressure of the vapor cell is exponential in temperature, operation at elevated temperatures to acieve greater accuracy would require greater control over cell temperature. Furthermore, temperature driven collisional shifts have far greater effects on instabilities than BBR shifts. A vapor cell with finite Rb, or starved vapor cell, would need to be constructed. A starved cell could benefit from these two magic temperature for future clock development.

dc-Stark shift

The dc polarizability of the $5D_{5/2}$ state was measured in [136], and it exceeds that of the $5S_{1/2}$ state by a factor of ~ 50 due to low-lying transitions to nearby levels. Using this polarizability, we calculate the fractional clock sensitivity to dc electric fields is $5.9 \times 10^{-15}/(\mathrm{V/cm})^2$. The magnetic shield surrounding the vapor cell assembly also acts as a Faraday cage to prevent external electric fields from reaching the atomic vapor. However, stray charge could accumulate on the glass vapor cell itself; any resulting patch potentials need to be stable at the 0.5 V level.

Similar to the magnetic field splittings, the dc-Stark splittings are commonly looked at in the weak and strong field limits. In order to determine the splittings

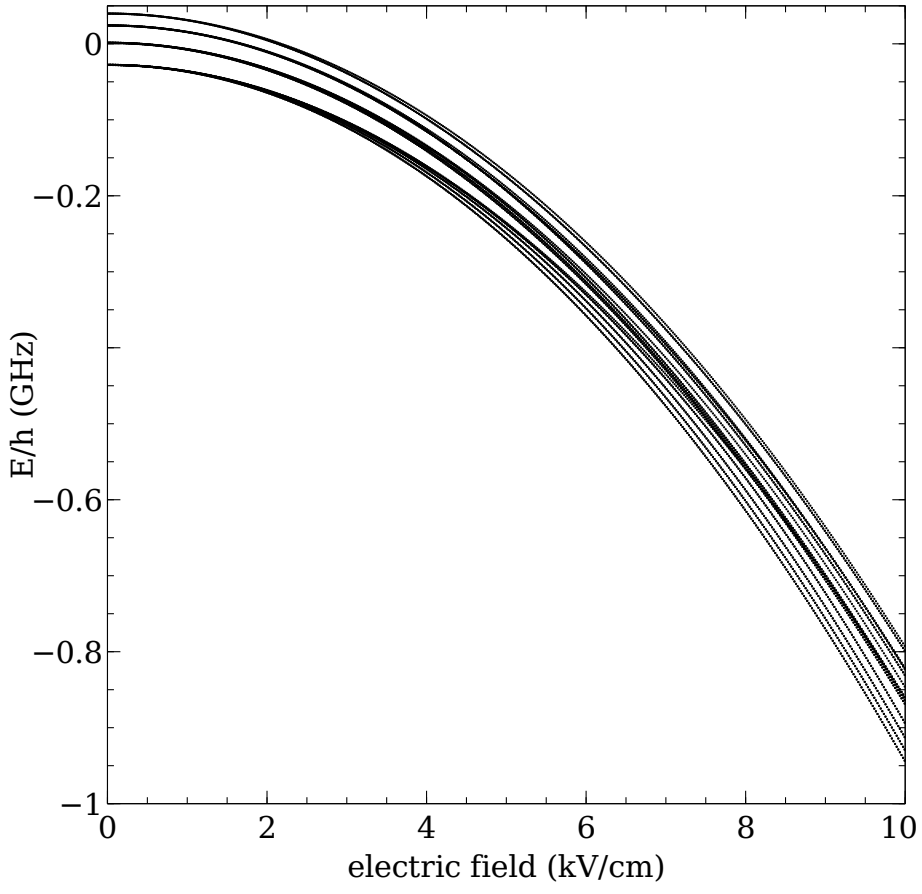

Figure 2.21: The dc-electric field splitting for the $5D_{5/2}$ states of of ^{87}Rb, which was determined by numerical diagonalization of the total Hamiltonian as described in the text.

caused by a wide range of electric fields the full Hamiltonian must be diagonalized. Appendix B details the difficulty of writing the hyperfine Hamiltonian in the strong field basis. The resultant dc-Stark splittings on the excited state for both ^{85}Rb and ^{87}Rb is now trivial to calculate, and are shown in Figure 2.22 and Figure 2.21 respectively. For the ground state splittings there is an analog to the Briet-Rabi formula yielding energy eigenstates of,

$$E_{|J=1/2 m_J; I m_I\rangle} = -\frac{1}{2}\alpha\left(J\right) E_z^2 - \frac{A_{hfs}}{4} \pm \frac{A_{hfs}}{2}\left(I(I-m_I)\right)^{1/2} \tag{2.55}$$

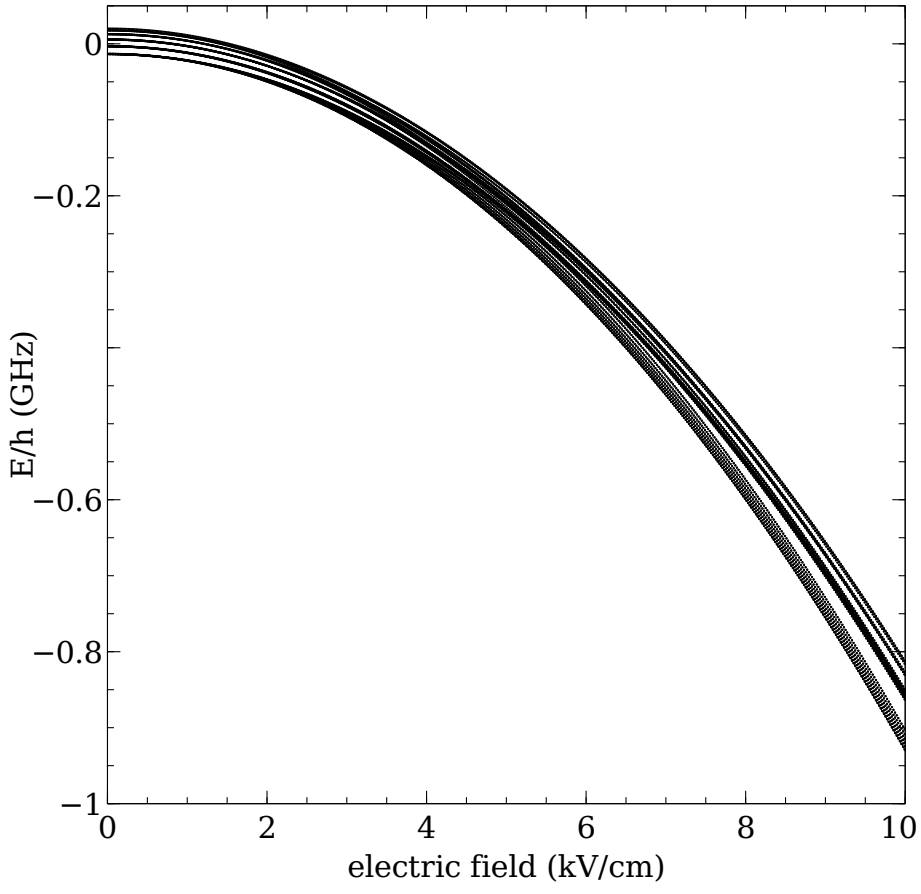

Figure 2.22: The dc-electric field splitting for the $5D_{5/2}$ states of of ^{85}Rb, which was determined by numerical diagonalization of the total Hamiltonian as described in the text.

2.6.6 Residual Amplitude Modulation

Frequency and phase modulation techniques are commonly used for laser frequency stabilization. These techniques are known to suffer from residual amplitude modulation (RAM) that can arise for a variety of reasons. Time-dependent RAM at the modulation frequency decreases the laser frequency stability. Following the derivation from Hall *et al.* [141], consider an EOM crystal with light propagating along the x axis. The index of refraction of the the ordinary axis (y axis, n_2) and the

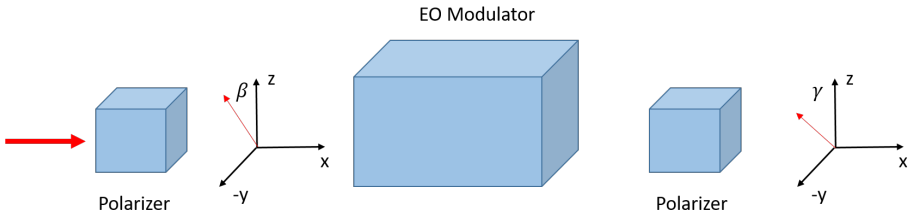

Figure 2.23: The picture above details the proposed EOM set-up. The EOM is placed between two polarizers on the input and output. Light exiting the first polarizer is linearly polarized at an angle β w.r.t. the EOM z-axis. Light leaving the final polarizer is at an angle γ w.r.t. the EOM z-axis. The proposed modulation electric field is applied in the z-axis.

extraordinary axis (z axis, n_3) are given by,

$$n_{2,3} = n_{o,e} - \frac{1}{2} n_{o,e}^3 r_{o,e} E_z, \tag{2.56}$$

where n_o and n_e are the unperturbed indices and r_o and r_e are the electro-optic coefficients for the ordinary and extraordinary axes, respectively. The applied electric field, E_z, is along the z direction. The total phase shifts seen by polarization along either the y or z axis for a crystal of length l and width d can be written as,

$$\phi_{2,3} = \phi_{o,e} + \phi_{o,e}^{dc} + \delta_{o,e} \sin \omega_m t \tag{2.57}$$

where,

$$\begin{aligned}
\phi_{o,e} &= \frac{2\pi l}{\lambda} n_{o,e}, \\
\phi_{o,e}^{dc} &= -\frac{\pi}{\lambda} \frac{l}{d} n_{o,e}^3 r_{o,e} V_{dc}, \\
\delta_{o,e} &= -\frac{\pi}{\lambda} \frac{l}{d} n_{o,e}^3 r_{o,e} V_{rf}.
\end{aligned}$$

V_{rf} and V_{dc} are the rf and dc voltages applied to the crystal generating the electric field E_z and ω_m is the modulation frequency. The final complex electric field output can be written as,

$$E_T = E_o e^{i\omega_0 t} \left[a \exp\left[i(\phi_o + \phi_o^{dc} + \delta_o \sin \omega_m t) \right] + b \exp\left[i(\phi_e + \phi_e^{dc} + \delta_e \sin \omega_m t) \right] \right] \tag{2.58}$$

where E_0 is the incident field intensity, $a = \sin\beta\sin\gamma$ and $b = \cos\beta\cos\gamma$, where β and γ are described in Figure 2.23 as misalignments in incident and modulated light polarizations w.r.t the crystal axis. However, the atoms detect the light intensity given by,

$$\begin{aligned} I = E_T E_T^* &= |E_0|^2 \left[a^2 + b^2 + 2ab\cos(\Delta\phi + \Delta\phi^{dc} + M\sin\omega_m t)\right] \\ &= |E_0|^2 \left[a^2 + b^2 + 2ab\sum_{k=-\infty}^{\infty} J_k(M)\cos(\Delta\phi + \Delta\phi^{dc} + k\omega_m t)\right] \end{aligned} \tag{2.59}$$

where

$$\begin{aligned} \Delta\phi &= \phi_e - \phi_o, \\ \Delta\phi^{dc} &= \phi_e^{dc} - \phi_o^{dc}, \\ M &= \delta_e - \delta_o, \end{aligned}$$

$J_k(M)$ is a Bessel function of the first kind and M is the modulation depth. In the simplest description RAM occurs when the frequency sidebands that are written onto the laser carrier frequency are not equal and opposite. This occurs when there are non-vanishing odd terms of Equation 2.59, i.e. k is odd. Pure phase modulation, a signal without RAM, thus requires that,

$$\sin\left(\Delta\phi + \Delta\phi^{dc}\right) = 0. \tag{2.60}$$

When the condition described in Equation 2.60 is not met, coherent detection of the signal at $k\omega_m$ yields a non-zero dc shift proportional to

$$4ab|\epsilon_0|^2 J_k\left(M\right)\sin\left(\Delta\phi + \Delta\phi^{dc}\right), \tag{2.61}$$

thereby altering the lock point of the system. Under different requirements a dc lock point shift might not be detrimental. However, the desired system instability goals require this lock-point to be stable to $< 1 \times 10^{-6}$, and several variables involved are time dependent. The crystal natural birefringence, $\Delta\phi$, is influenced directly by crystal temperature change, variations in laser power and rf modulation intensity.

The detected laser amplitude, ϵ_0, can change with time dependent scatter, the ètalon effect, and photorefractive effects in the crystal. Entry and exit polarization parameters, a and b, can change with crystal vibration, temperature and stress-related input fiber polarization wander. Finally, the modulation intensity of the electric field (M), which depends directly on rf modulation, may vary over time.

Although not explicitly present in Equation 2.61, quadrature RAM has a similar effect of dc lock point error and can arise for a few reasons listed by Ishibashi *et al.* [72]; piezo-electric response of the EOM crystal leading to beam steering, temperature dependence of the beam optical path, and spacial inhomogeneity of the modulation field in the EOM crystal leading to angular deviation of the beam. All three of these effects result in quadrature RAM.

Arising from the finite lifetime of the excited transition, the atoms introduce a phase delay to the detected florescence signal (for a 450 kHz modulation this delay is 37°). Although, the lock-in phase could be adjusted, it could never perfectly match the phase delay arising from the fluoresced single. Suppression of both in-phase and quadrature RAM is necessary.

Suppression of RAM

Suppression of RAM is extremely important to the short and long term stability of the clock. Passive suppression of RAM can be attained through a few methods. Spurious polarization effects can be suppressed with proper alignment of the input and output polarization w.r.t. the crystal axis. Complete suppression of polarization driven RAM with passive methods is impossible if misalignment is driven by mechanical vibrations and thermal expansion. Ètalon effects can be partially suppressed with the proper use of optical isolators. However, laser scatter still remains, which largely impacts the final detected amplitude. Finally, a properly saturated input to the optical amplifier leads to a passive suppression of RAM. These three passive techniques

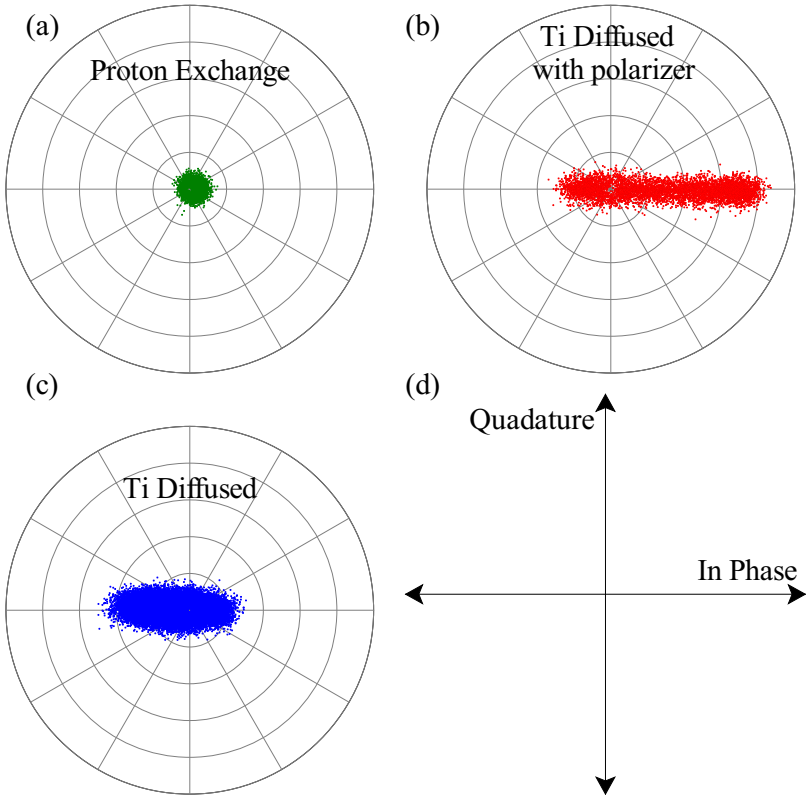

Figure 2.24: Presented above is data taken from three different EOMs using a network analyzer as described in the text, (a) Shows the proton exchange model, (b) shows the titanium diffused model with an integrated polarizer and (c) shows the titanium diffused model without the integrated polarizer. (d) Shows which axes the quadrature and in-phase RAM are measured along.

are employed in the experiment in an attempt to reduce the amount of RAM before any active techniques are utilized.

The choice of modulator became more complicated then initially thought. Lithium niobate is a common crystal used in optical modulators due to its electro-optic and nonlinear coefficients. A waveguide modulation requires lower modulation voltages, and reduces the size of the laser system making a waveguide modulation attractive for O-RAFS. The two most common techniques for waveguide implementation include titanium diffusion and proton exchange. Devices produced with each of the

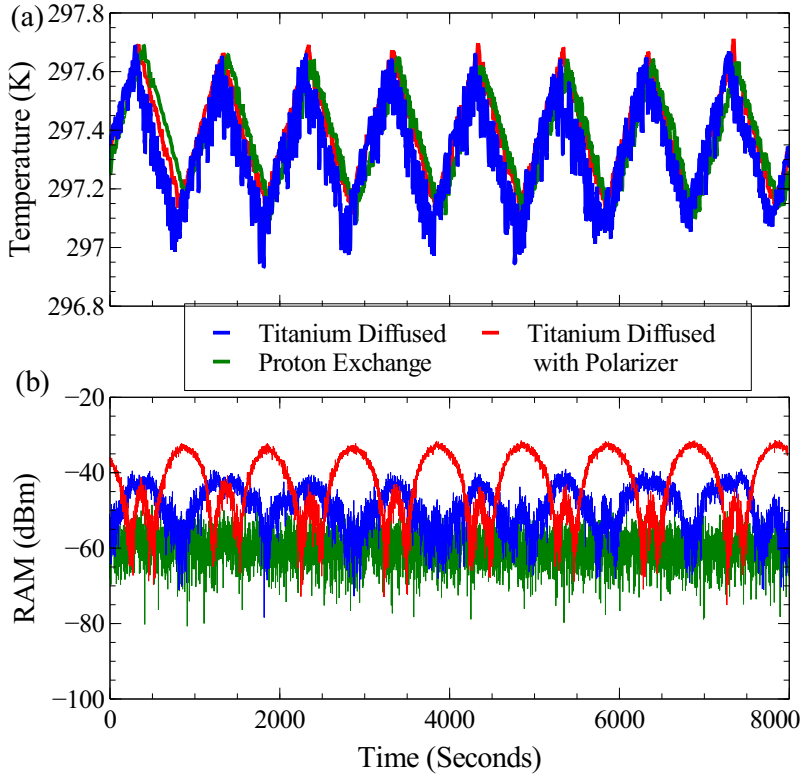

Figure 2.25: Three lithium niobate phase modulators were integrated into a simplified optical chain, a proton exchange (green), a titanium diffused (blue) and a titanium diffused with integrated polarizer (red). A slow, 0.5 °C at 20 mHz, temperature ramp was applied to each EOM, shown in (a), each EOM was driven with an RF modulation signal and the RAM was detected downstream, shown in (b).

processes were investigated as potential modulators in the final design. Each device was tested in several ways to determine properties of the ideal EOM to best suppress RAM.

A simplified experiment was designed where a Keysight E5061B network analyzer was used to drive the modulator and detect the RAM, thus enabling simultaneous analysis of both the in-phase and quadrature RAM signals. Three modulators were examined: two titanium diffused lithium niobate modulators where one had an integrated polarizer on the output of the crystal and one proton exchange model. The

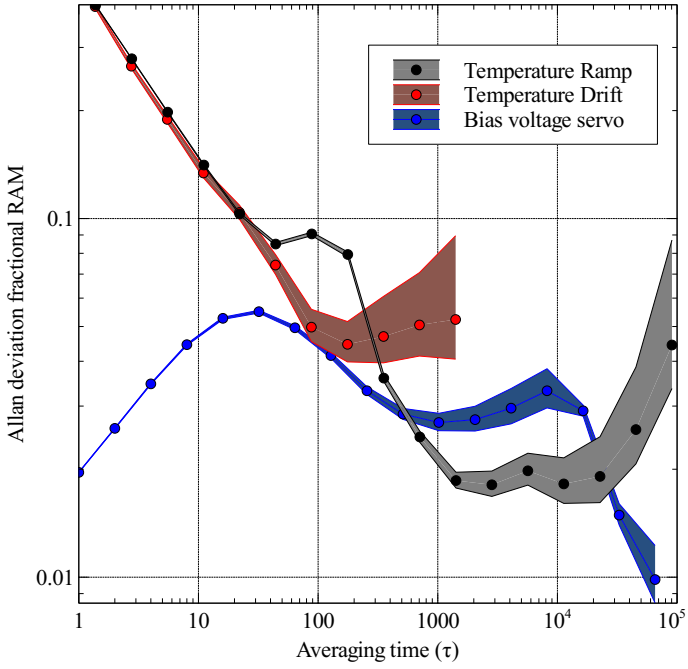

Figure 2.26: Shown above are Allan deviations of fractional RAM measurements during three experiments with a proton exchange lithium niobate modulator. The three experiments involved an EOM with: 1. No active RAM suppression and no temperature control (red), 2. No active RAM suppression while sitting on a temperature controlled plate with an oscillating set-point as described in the text (gray) and 3. Active dc bias RAM suppression while sitting on a stable temperature controlled plate (blue).

RAM signal was plotted in a polar plot (on the same scale) with the in-phase RAM signal aligned to $\theta = 0°$ and the quadrature RAM signal along the $\theta = 90°$, see Figure 2.24. From these plots it is easy to see that the proton exchange model had reduced in-phase RAM as well as reduced quadrature RAM over the titanium diffused modules. Manufacturing processes are not the only contributor to the difference in performance. Electrode and waveguide package design influence the modulation depth parameter and field uniformity. This test only compared EOM models not manufacturing processes.

Temperature is a large driver in clock performance. Slow temperature variations

were applied to various laser components to determine which needed precise temperature control. Large shifts in RAM as a function of temperature, sometimes as large as 50 dBm/°C, were apparent for the titanium diffused models. The proton exchange model had relatively low coupling between EOM temperature and detected RAM, see Figure 2.25 (b). Proton exchange lithium niobate is a polarizing material, light that propigates polarized along the wrong crystal axis experiences loss. Proton exchange models have been used in polarization optics [131] with > 50 dB polarization extinction ratio. Use of this model eliminates the need for integrating polarizers before and after the EOM. Since small changes in temperature can cause the input and output polarizations to wander w.r.t. the crystal axis, the polarizing proton exchange model is more robust to thermally induced polarization wander.

While investigating how temperature changes on various laser components impacted clock performance, I found that applying this slow temperature ramp helps reduce RAM generated by the proton exchange model on longer timescales, see Figure 2.26. Alternatively, active suppression of the in-phase AM, satisfying Equation 2.60, can be achieved by properly applying a dc voltage to the modulator. This technique allows for further RAM suppression on shorter timescales without an increased RAM instability at the temperature modulation frequency, as well as better performance over longer timescales, 10^5 secs. However, the presence of free charge, which degrade the effective dc electric field applied in the crystal, complicate this technique. To compensate for this another loop is employed, which periodically switches the sign of the applied dc voltage allowing RAM to be suppressed with a finite field, see Figure 2.27. In addition to the dc bias switch, a fraction of the detected RAM is added to the florescence signal to account for the remaining RAM.

Quadrature RAM can be suppressed with an active servo modulating the temperature of the EOM [147]. This has never successfully been executed with O-RAFS. Alternatively, an acoustic optical modulator (AOM) used as an amplitude modulator could be used to suppress both in-phase and quadrature RAM [145].

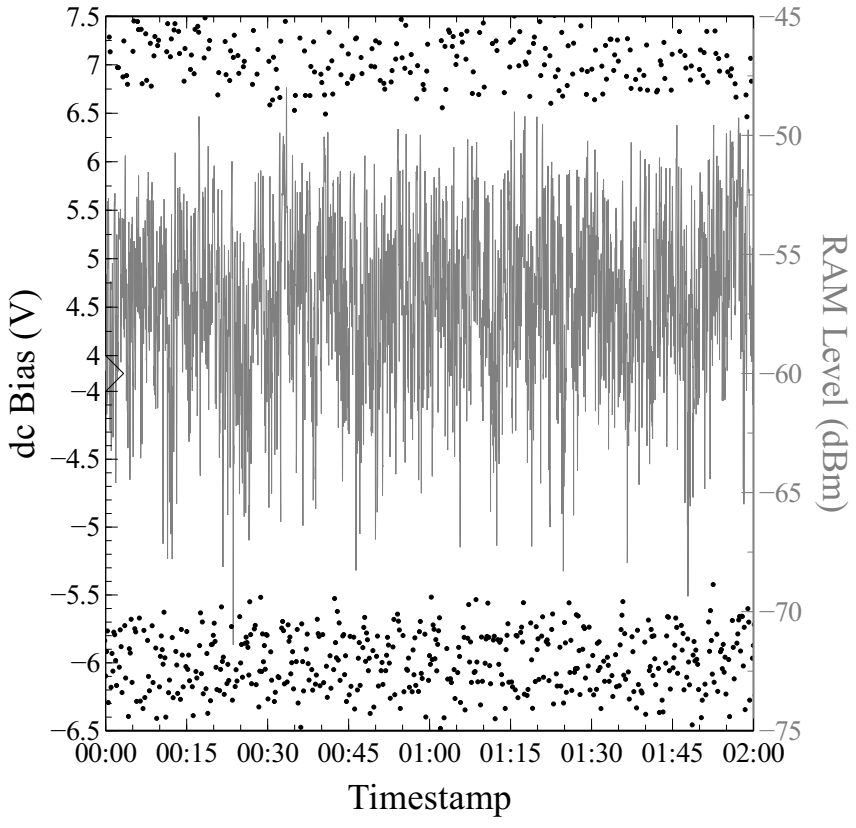

Figure 2.27: Shown above is the recorded RAM signal as well as the dc bias voltage that periodically switches sign to prevent slow charge migration in the lithium niobate crystal.

2.7 Discussion

Having assessed the leading contributions to instability, see Table 2.3, clock performance was measured by photodetecting the comb repetition rate and counting it relative to a hydrogen maser. During data collection, the vapor cell temperature and 778 nm laser power were monitored. The counter was gated at a rate of 1 Hz, and the resulting frequency record was analyzed after removing a linear drift of -1×10^{-18}/s. Figure 2.28 shows the resulting total Allan deviation for a time record of 40,000 s, and the system is shown to average as $4 \times 10^{-13}/\sqrt{\tau(s)}$ for τ from 1 s to 10,000 s.

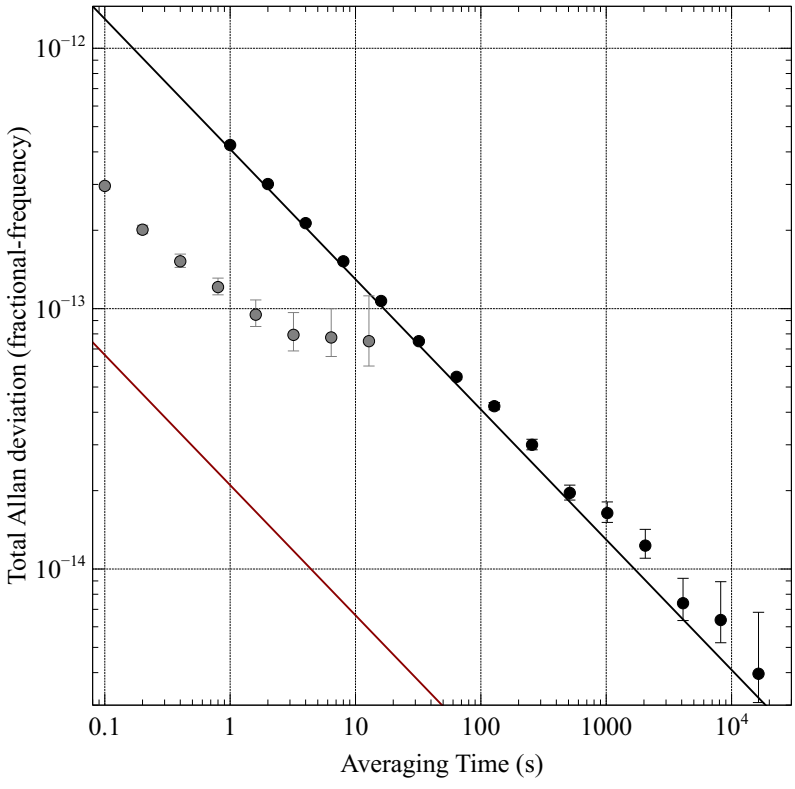

Figure 2.28: The measured fractional frequency instability for typical operating conditions (black circles) plotted as a Total Allan deviation along with a $1/\sqrt{\tau}$ white noise line (black solid line). Also shown are the measured instability when the frequency standard was operated with a larger signal to noise ratio (grey circles) and the expected intermodulation limit (red) as described in Sec. 2.5. Figure originally presented in [92].

On longer timescales, however, the instability increases. Figure 2.29 shows total Allan deviation for a record of 180,000 s, as well as the expected clock performance limitations derived from out-of-loop measurements of the cell temperature and laser power. On some timescales, the clock performance exceeds the expected stability as determined from laser power measurements; however, long term laser power measurements from the witness photodiode are thought to be particularly influenced by room temperature fluctuations, and these temperature variations may lead to an overestimate of Stark shift-related clock instability. The apparent "bump" in all sig-

Table 2.3: The environmental variables that impact ^{87}Rb clock performance are listed along with the corresponding fractional frequency sensitivity coefficient. The right column tabulates the stability requirement for each parameter to support a fractional frequency instability of 1×10^{-15}. Table originally presented in [92].

Shift	Fractional Coefficient	Stability at one day
778 nm AC Stark	4.8×10^{-13}/mW	2.1 μW
Rb density	1.1×10^{-12}/K	0.92 mK
Blackbody Radiation (at 373 K)	$5.5 \times 10^{-16}/K$	1.82 K
DC Stark	$5.9 \times 10^{-15}/(\mathrm{V/cm})^2$	0.17 $(\mathrm{V/cm})^2$
2^{nd} Order Doppler	$1.0 \times 10^{-15}/K$	1.0 K
Zeeman	$6.5 \times 10^{-11}/\mathrm{G}^2$	3.9 mG
Helium Collisional	2.7×10^{-8}/Torr	3.6×10^{-8} Torr

nals around 10^4 s is likely caused by room temperature fluctuations, indicating that the frequency standard performance can be improved by more tightly regulating the system temperature.

In principle, the short-term instability of this system could be decreased by either collecting a greater fraction of the atomic fluorescence or by increasing the laser power incident on the vapor cell. To demonstrate this, the clock was operated with significantly higher laser power, resulting in brighter fluorescence signals and reduced instabilities. The gray points in Figure 2.28 demonstrate a one-second Allan deviation of approximately 1×10^{-13}, which is consistent with the expected limit from the hydrogen maser frequency reference. In-loop stability estimates suggest that the actual one-second Allan deviation for this mode of operation could be in the middle of the 10^{-14} decade; however, for the current design, operating at this level is detrimental to the long-term stability due to fluctuations of the ac-Stark shift as described in Section 2.6.5. To achieve the best long-term performance, the clock is typically operated with 30 mW of laser power, as it represents a compromise between shot noise and ac-Stark shift. The clock stability predicted in Section 2.5 of $\sigma_y(\tau = 1s) \approx 4.7 \times 10^{-13}$ for 30 mW of laser power incident on the vapor cell, is near

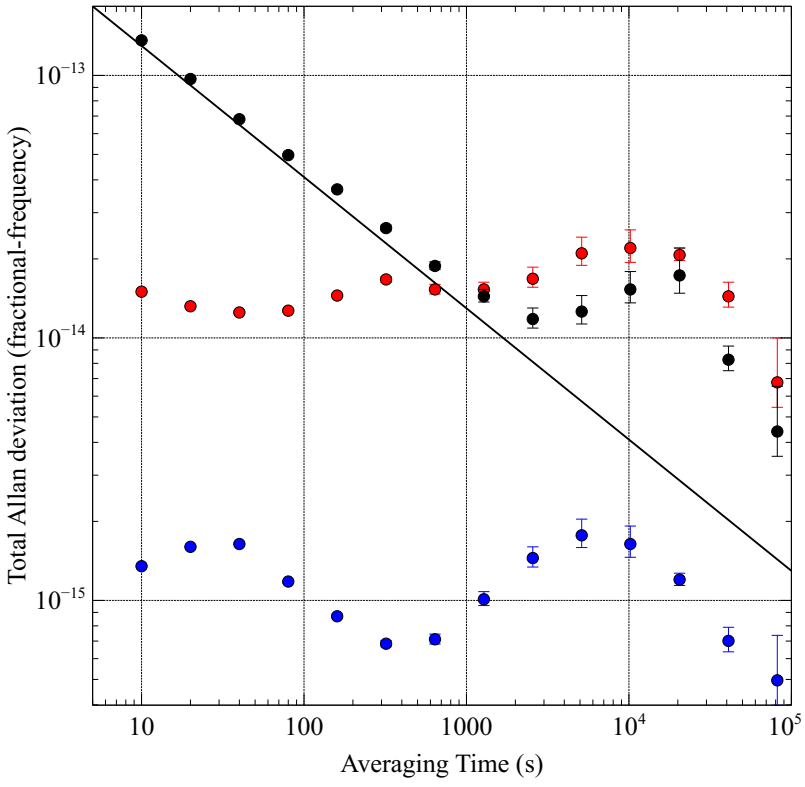

Figure 2.29: The fractional frequency instability plotted as a Total Allan deviation for ^{87}Rb with $1/\sqrt{\tau}$ white noise (black) as well as anticipated limits on the clock stability arising from cell temperature fluctuations (blue) and laser power fluctuations (red). The instability limit arising from laser power fluctuations is believed to be an overestimate due to temperature-dependent effects in the witness photodiode as described in the main text. Figure originally presented in [92].

to the observed instability of $\sigma_y(\tau = 1s) \approx 4.1 \times 10^{-13}$ shown in Figure 2.28

The system is capable of averaging down to less than 7×10^{-15} at 16,000 s and to $\lesssim 1 \times 10^{-14}$ at one day. It appears that, on timescales beyond a few hours, the instability is related to the ac-Stark shift, which would indicate that an improved method for detecting and stabilizing the laser power will be required to achieve fractional frequency instabilities of 1×10^{-15} at one day. The initial optical design of the vapor cell assembly implemented a photodiode, thermally anchored to temperature stage 2

for reduction of temperature-influenced drifts, as the in-loop laser power sensor. Instead the PMT photo-current was implemented as the feedback sensor because it was found to produce superior results. One advantage of stabilizing the laser power based on the detected fluorescence signals is that it relies on an atomic signal rather than a beam sampling optic, for which the reflectivity is subject to polarization and temperature variations. Nevertheless, thermal considerations are still required, as the PMT's conversion efficiency is also temperature dependent [144], with an expected coefficient of 0.5 % to 1 % per K. Within the current design of the vapor cell assembly, an attempt was made to thermally connect the PMT to temperature stage 2, and fiberglass insulation was used to reduce thermal parasitics. However, temperature gradients are difficult to minimize over the 10 cm length of the PMT. Additionally, the PMT's high voltage power supply and transimpedance amplifier need to provide constant voltage and gain, respectively, in order to use the PMT as a long-term laser power sensor.

Alternatively, if improving the laser power stability proves too challenging, there are several design modifications that allow the two-photon clock to operate with a smaller ac-Stark shift. First, the spectral linewidth could be decreased by removing the helium contamination in the vapor cell. In the current cells, which are expected to be saturated with 4 mTorr of helium, the linewidth is approximately a factor of 2 larger than the natural linewidth. Removing the helium (through the use of a vacuum chamber or a helium-resistant cell [40]) would allow for a reduced laser power by a factor of 2 without affecting the short-term stability. Additional modifications include increasing the efficiency of the fluorescence detection; increasing the effective length of the vapor cell by routing the beam through the vapor on multiple, non-overlapping passes; increasing the vapor density; and decreasing the desired short-term stability metric. Another final option is to increase the laser beam radius and laser power together; increasing both the power P and the intensity radius w_0 by a factor of F results in the same photon detection rate (accounting for both the

decreased optical intensity and the increased number of atoms in the beam path) but a smaller overall ac-Stark shift by the same factor F.

Chapter 3

O-RAFS revisited

The stability shown in Figures 2.29 and 2.28 represents the best reported stability (long or short-term) for a two-photon transition in Rb [92]. A system whose fractional frequency flicker floor is 1×10^{-14} fails to improve upon existing technology from a portable frequency standard sense (see Figure 3.1). Efforts to further reduce the instabilities of the O-RAFS clock are presented here to produce a frequency standard that surpasses existing portable technologies.

3.1 Reducing the ac-Stark shift

Proper authority over laser power is a challenge in the O-RAFS system described in Chapter 2. As presented in Table 2.3, the ac-Stark shift is quite large and imposes a stringent requirement over laser power stabilization (1 part in 10,000). The data presented in Figure 2.29 shows that the ac-Stark shift limits clock performance. However, Equations 2.33 and 2.10, reveal a simple idea to reduce ac-Stark effect while maintaining low short term instability: reduce laser intensity by expanding the beam and increase efficiency of the blue fluorescence collection. A new atomic reference chamber was built that increased the PMT active area, optimized the path

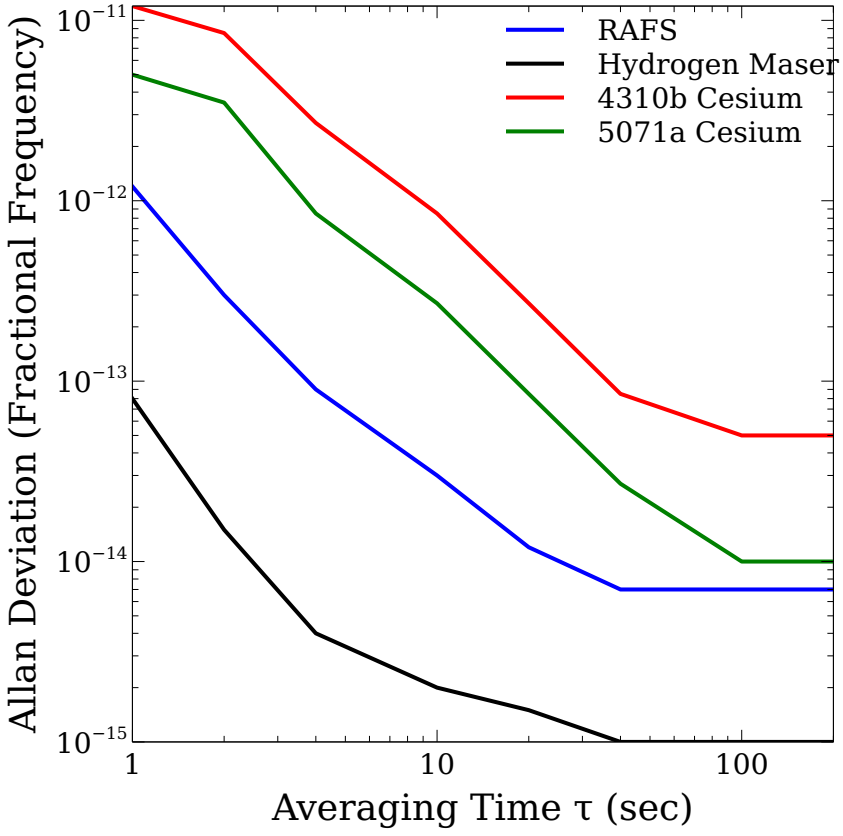

Figure 3.1: Shown here are four commercial microwave clocks currently on the market, the Hydrogen maser (black), the rubidium atomic frequency standard or RAFS (blue) and two cesium clocks, the 4310B (red) and the 5071A (green). [1, 2, 108, 109]

length of the laser through the vapor cell to leverage this increased area, and added a second vapor cell bending the laser through a right angle prism to further increase the use of the incident red light (see Table 3.1).

The rate at which atoms are excited is equal to the two-photon cross section, $\sigma_{2\gamma}$, times the square of the intensity divided by the photon energy,

$$A_{i\to f} = I^2 \sigma_{2\gamma} \frac{\lambda}{hc}. \tag{3.1}$$

The detection rate can be calculated as a volumetric integral of $A_{i\to f}$ over the beam volume times the density of atoms times a collection efficiency (that takes into ac-

Table 3.1: Proposed design changes to increase fluorescence detection efficiency and reduce ac-Stark effects.

Parameter	Chapter 2 design	Proposed changes
PMT quantum efficiency	0.148	0.325
PMT active area	78.5 mm^2	324 mm^2
Beam waist	0.6 mm	2.1 mm
Rb cell path length (two total cells)	5.3 mm	18 mm

count the probability of the decay channel b_r, the PMT efficiency Q_{eff} and the effective solid angle of fluoresced light collected e_C),

$$R_{i\to f} = \rho \underbrace{b_r Q_{eff} e_C}_{\text{collection efficency}} \int A_{i\to f} dV. \tag{3.2}$$

Calculation of the integral requires knowledge of the laser beam intensity profile. The beam can be assumed to be of Gaussian profile, perfectly overlapped with the retro-reflected beam which has some loss from an imperfect reflector,

$$I(r) = (1+\eta_r)\frac{2P}{\pi w^2} e^{-2r^2/w^2}. \tag{3.3}$$

Final integration of Equation 3.2 yields,

$$R_{i\to f} = \frac{b_r e_C L_0 \rho P^2 Q_{eff} (1+\eta_r)^2 \lambda \sigma_{2\gamma}}{ch\pi w^2}. \tag{3.4}$$

If we assume that no other parameters change outside the listed ones in Table 3.1, we can calculate the power and thus the final average intensity required to achieve a detection rate necessary to reach instabilities of 1×10^{-13} at one second in the shot noise limit,

$$\sigma_y^{(SN)}(\tau) = \frac{\Delta\nu}{\omega/2\pi} F_{\text{Noise}} \frac{1}{\sqrt{R_{i\to f}/2}}. \tag{3.5}$$

Given that the noise factor, F_{Noise}, for a typical PMT is generally 2, the power to reach short term stability goals for the design in Chapter 2 is around 25 mW. For the new design the required power to reach the necessary detection rate drops to around

19 mW; however, the average intensity across the beam decreases significantly, leading to a 15× reduction of ac-Stark shift.

Unfortunately, this picture is incomplete. The cells in the original design were at Brewster's angle. The new vapor cells are at a normal incidence and, although an anti-reflective coating was added to both sides of all vapor cell windows, initial tests showed large amount of scattered light still present on the PMT leading to a reduction of almost 2× in anticipated detection rate. Including these corrections, the expected ac-Stark limitation is 2×10^{-15}, a shift of 2×10^{-14} $(\mathrm{mW/mm^2})^{-1}$, an improvement over the original limit of 2×10^{-14}, a shift of 2.5×10^{-13} $(\mathrm{mW/mm^2})^{-1}$.

3.2 Collisional shifts revisited

A new vapor cell was designed, a 10 mm cylinder that was 52 mm long. The cell has 3 mm thick windows and wall thickness of 1 mm. The fill tube was kept purposely long at 13 mm in an attempt to generate a condensation pot for the liquid Rb. The body of the cell was regulated to a temperature, T_H, warmer than the cell fill tube at T_C, see Figure 3.2 (a). Relying on the hypothesis that the Rb vapor pressure would be driven by the coldest spot in the cell, this new design is supposed to increase temperature control precision. After completion of the design and integration into a vacuum chamber this hypothesis was tested. Figure 3.2 presents data from three experiments. Experiment 1 regulated T_C to 100 °C while measuring clock frequency shift as a function of T_H (black). Experiment 2 regulated T_H to 106.7 °C while measuring clock frequency shift as a function of T_C (blue). Experiment 3 regulated T_C to 112.7 °C while measuring clock frequency shift as a function of T_H (red). Concern about Rb collecting on the top of the vapor cell left Experiment 3 to be the shortest, shortly after collecting data the temperature of T_H was raised to alleviate this concern. Similar to the experiment performed in Section 2.6.1 the vapor cell temperature was allowed to first stabilize and frequency data was collected over 300

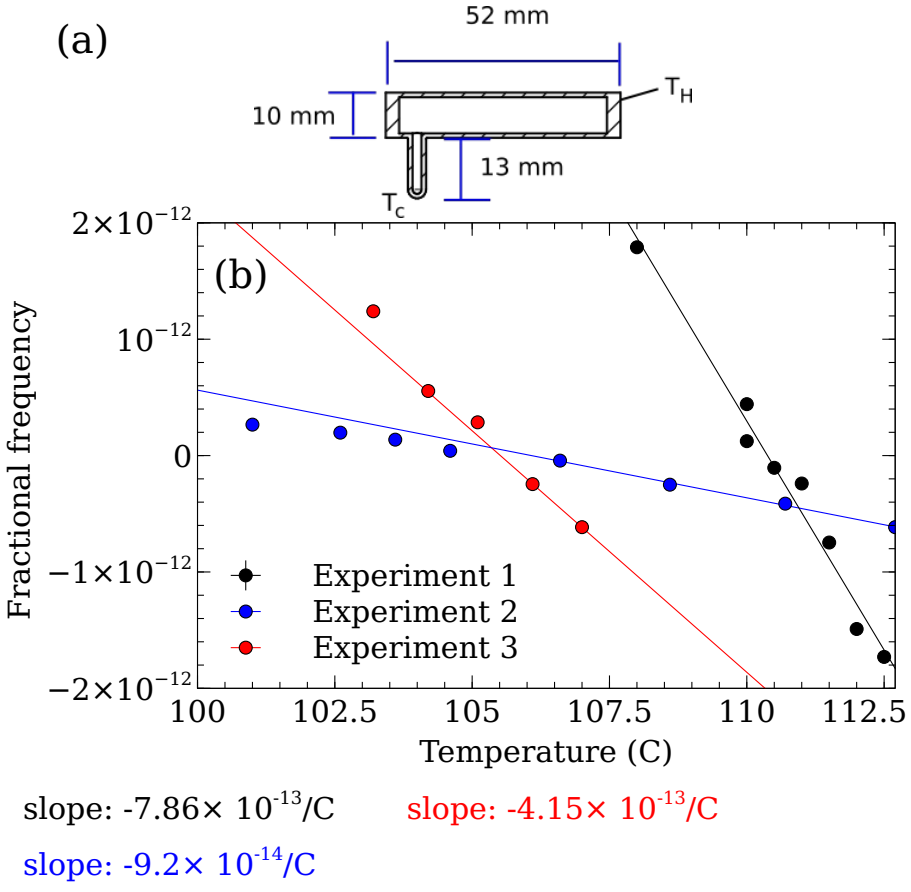

Figure 3.2: (a) New vapor cell dimensions. Shown in (b) are three distinct experiments measuring the fractional frequency shift as a function of temperature change as described in the text.

s. The data was fit using a least squares linear regression and yielded three distinct shift parameters. This could imply that not only does the absolute temperature of the measurement reflect the dependence of frequency but also the temperature profile over the entirety of the cell. This possibly explains the measurement discrepancy between Refs. [146] and [92].

3.2.1 Helium Leak

Helium permeation through a fused silica vapor cell was described in Section 2.6.1. Data shown in Figure 3.3 shows continuous fractional frequency data taken over 40 days. Accounting for the new vapor cell geometry: $A = 11.56$ cm^2, $V = 2.3$ cm^3, and $d = 0.1$ cm one can calculate the permeation rate to be 7.3×10^{-9} cm^2/sec slightly higher then the 1×10^{-9} cm^2/sec measured in Ref. [5]. This discrepancy could be accounted for by looking at the physical geometry of the cells or in the actual temperature of the vapor cell. Since the permeation rate is exponential in vapor cell temperature small changes in absolute operational temperature could make dramatic differences. It is also important to note that the exact composition of the glass could change the solubility and diffusion rate a reasonable explanation for the discrepancy. The expected time for helium to reach negligible levels is approximately 157 days.

3.3 Working without RAM

Section 2.6.6 collects the best known methods of actively suppressing RAM. The following surmises the effort:

- Use a polarizing EOM.
- Temperature stabilize the EOM.
- Detect RAM nearby the atomic source.
- Engage a servo applying a dc offset to suppress RAM.
- Adjust the phase of the lock-in to only suppress the in phase portion of the RAM signal.
- Correctly choose a coefficient to digitally multiply the remaining RAM signal and add to the fluorescence signal, thus removing the remaining effects of RAM.

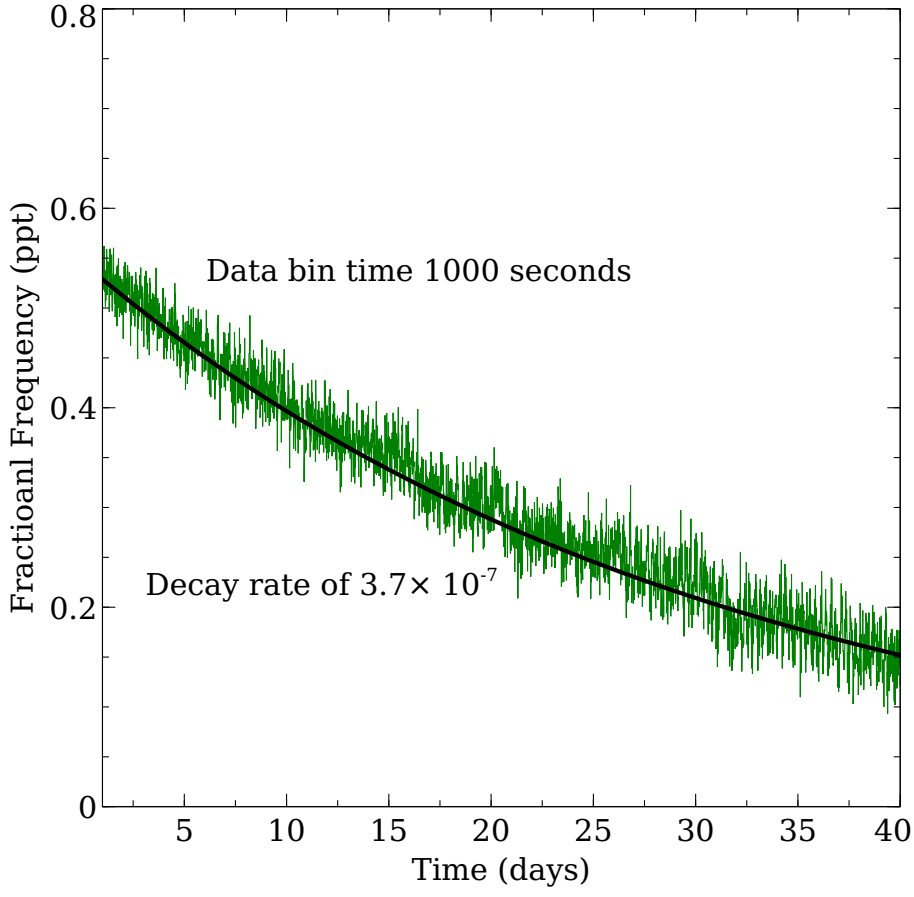

Figure 3.3: The normalized fractional frequency output with an observed exponential drift with rate of -3.7×10^{-7}/sec, similar in magnitude and sign as the predicted shift due to helium leaking from the vapor cell.

- Start the loop that switches the sign of the dc bias occasionally. Pick the right settling time to allow the EOM surface charge to settle some, but not too much.

- Start data collection and cross your fingers.

After struggling with proper RAM suppression, with only slight improvements to the clock performance, another method was desired.

The derivation of RAM in Section 2.6.6 relies on the presence of an EOM. A

more general derivation of RAM would look at all amplitude modulation that occurs with the same frequency as the phase modulation of the laser. Following closely to the derivation in Burck *et al.* [46] the electric field of a phase modulated laser with residual amplitude modulation at ω_m is,

$$E(t) = \sum_k \beta_k e^{ik\omega_m} e^{i[\omega_0 t + M\sin(\omega_m t)]}, \tag{3.6}$$

here β_k is the k^{th} Fourier component of the amplitude modulation, $\beta_0 = 1$ and the amplitude modulation yielding the constraint that $\beta_{-k} = \beta_k^\star$. The Fourier expansion of the frequency modulated signal is given by,

$$e^{i[\omega_0 t + M\sin(\omega_m t)]} = \sum_p J_p(M) e^{i[\omega_0 + p\omega_m]t}, \tag{3.7}$$

where $J_p(M)$ is the p^{th} order Bessel function. Equation 3.7 can now be written,

$$E(t) = \sum_p h_p e^{i[\omega_0 + p\omega_m]t}, \tag{3.8}$$

where,

$$h_p = \sum_k \beta_k J_{p-k}(M). \tag{3.9}$$

As light travels through the system, the light experiences a differential index of refraction (in this case assumed to be dominated by the EOM) and absorption provided by the atomic species under observation.

$$F(\omega) = e^{-T(\omega)-\phi} \tag{3.10}$$

with

$$T(\omega) = \frac{\alpha(\omega)L}{2} + i\frac{\omega n(\omega)L}{c} \tag{3.11}$$

describes the absorption, $\alpha(\omega)$ and the index of refraction, $n(\omega)$, of the atomic medium. In the region of weak resonance Equation 3.10 can be written $F(\omega) \approx (1 - t(\omega)) \times e^{-\phi}$. The detected signal is then mixed with the original modulation source generating the error signal S_{det}. Not only can the modulation frequency ω_m

be used as the demodulation source, but also integer multiples of ω_m. The choice of the n^{th} integer multiple of the modulation for detection of the signal with arbitrary phase, θ, between demodulation source and the electric field is proportional to

$$S_{det} = \frac{\Theta}{2}\sum_p h_p \left(h^\star_{p+n}e^{i\theta} + h^\star_{p-n}e^{-i\theta}\right) - \Theta\sum_p h_p T_p \left(h^\star_{p+n}e^{i\theta} + h^\star_{p-n}e^{-i\theta}\right) \quad (3.12)$$

with $T_p = T(\omega + p\omega_m)$ and $\Theta = |e^{-\phi^2}|$. The first term in Equation 3.12 is the signal background. When the modulation is larger than the carrier linewidth the detected signal can be written,

$$S_{det} = \Theta S_{bg}(\theta) - \Theta h_0 T_0 Re\left[h^\star_n e^{i\theta} + h^\star_{-n}e^{-i\theta}\right]. \quad (3.13)$$

The in phase detection with n even is,

$$S_{det} = \Theta S_{bg}(0) - 2\Theta J_0(M)J_n(M)Re\left[T_0\kappa\right], \quad (3.14)$$

with quadrature detection and n odd

$$S_{det} = \Theta S_{bg}(\pi/2) - 2\Theta J_0(M)J_n(M)Im\left[T_0\kappa\right]. \quad (3.15)$$

When $J_0(M)J_n(M) \neq 0$ κ can be written as,

$$\kappa = \frac{1}{2\Theta J_0(M)J_n(M)}\sum_k \beta_k J_{-k}(M) \times \sum_l \left(\beta^\star_l + (-1)^l\beta_l\right) J_{n-l}(M). \quad (3.16)$$

At this point Burck *et al.* apply some Bessel function gymnastics to show that

$$\kappa = 1 + \frac{J_1(M)}{J_0(M)} \times \frac{J_{n+1}(M) - J_{n-1}(M)}{2J_n(M)}\mu^2\sin^2(\psi) - i\left(\frac{J_1(M)}{J_0(M)} - \frac{J_{n+1}(M) - J_{n-1}(M)}{2J_n(M)}\right)\mu\sin(\psi). \quad (3.17)$$

The symmetry of the second terms in both Equations 3.14 and 3.15 is determined by the symmetry of κ. RAM will still distort the line shape. However, only when κ has an odd symmetry will the lock-point move. The negative effect of RAM is the shifted lock point, forcing

$$\frac{J_1(M)}{J_0(M)} - \frac{J_{n+1}(M) - J_{n-1}(M)}{2J_n(M)} = 0 \quad (3.18)$$

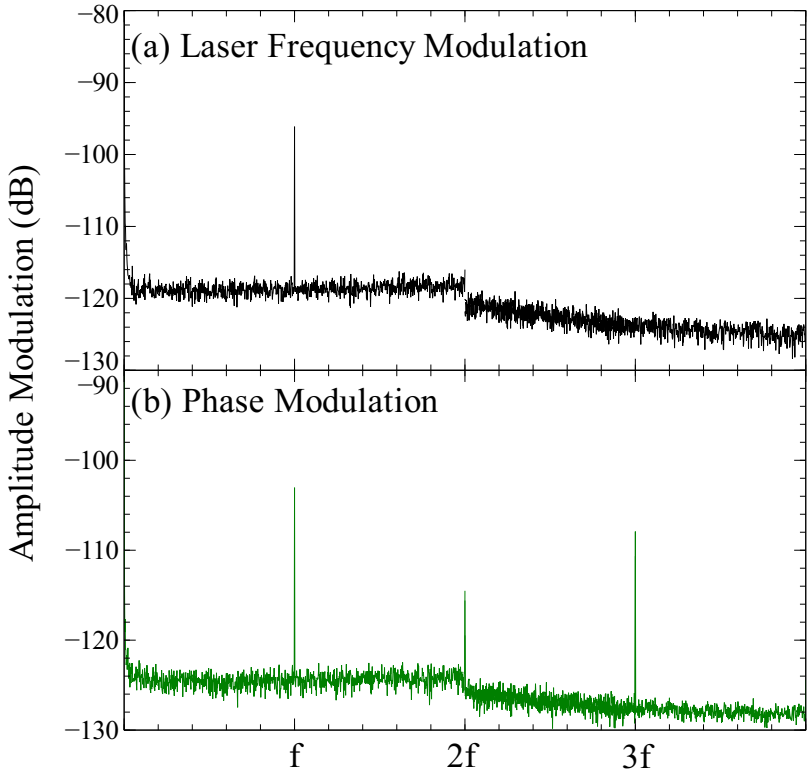

Figure 3.4: Direct measurements of the residual amplitude modulation from (a) modulating the laser frequency and (b) modulating the phase with an EOM. Note the discontinuity at 2f. The data was pieced together from two separate datasets as the spectrum analyzer didn't have sufficient bandwidth and resolution to span the full 500 kHz.

does not eliminate RAM, but forces the RAM to effect the error signal in a symmetric way. This relationship can be forced for a plethora of choices of n and M. The first such instance occurs at $n = 3$ (the third harmonic of the modulation signal) and $M = 3.544$.

Demodulating the signal with a $3f$ detection (detection on the third harmonic of the modulation signal) can eliminate the RAM from the $1f$ modulation. However, there still exists a potential for $3f$ RAM (generated by the initial modulation signal) to alter the lock point of the system, and a servo would still be needed to compensate

Table 3.2: Typical parameters related to the short-term stability of the frequency standard optimized for fluorescence detection as described in the main text.

Parameter	Typical value
Detection rate	5.0×10^{7}/s
S_v	1.6×10^{-7} V^2/Hz
g_{PD}	0.625
V_e	0.2 V
$\Delta\nu$	514 kHz
Effective SNR (10 kHz bandwidth)	19
σ_y (1 s)	5.9×10^{-13}
$S_y^{(LO)}$ $[2f_m = 50$ kHz$]$	1.8×10^{-26}/Hz

for $3f$ RAM. Figure 3.4 shows the detected RAM from a phase modulated laser using an EOM and a frequency modulated laser, directly modulation the current. Directly modulating the frequency of the laser generates less $3f$ RAM, thus eliminating the requirement for a RAM servo.

3.4 Results

Data was collected with the classic RAM suppression techniques described in Section 2.6.6 and the Allan deviation is presented in the red curve in Figure 3.5. Short term stability analysis was performed, Table 3.2, in good agreement with the measured performance of a shot noise limited system of $4.6 \times 10^{-13}/\sqrt{\tau}$. Unfortunately, although the there was an increase in long-term stability over the previous design, clock performance fell short of the predicted ac-Stark flicker floor.

The final system design leverages a 3f locking technique directly modulating the laser frequency. Data collected leveraging a 3f locking technique is shown in black in Figure 3.5.

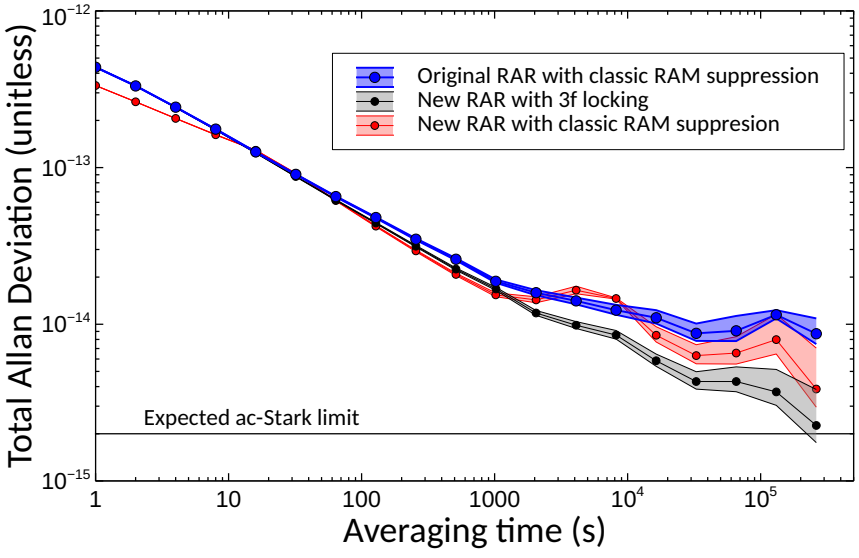

Figure 3.5: Shown above is the system described in Chapter 2 (blue), the new system as described in Section 3.1 with classic RAM suppression as described in Section 2.6.6 (red) and the new system described in 3.1 with 3 f locking techniques described in Section 3.3 (black). Also shown is the proposed ac-Stark limit of the new design under certain assumptions detailed in the text.

3.5 Advanced O-RAFS

Further reduction of the ac-Stark shift would be a powerful tool to reach the final long-term instability goal of 1×10^{-15} at one day. Alternative to the outlined approach in Section 3.1, two lasers of different frequencies could be utilized to excite

Table 3.3: Proposed wavelengths, associated shifts and required power (mW) per mW of 778 nm for a ac-Stark mitigation laser.

Wavelength (nm)	ac-Stark shift (Hz/(mW/mm^2))	Power multiplier $\times P_{778}$
1556.2	-16.5	10.8
808	-30.9	5.7
785	-62.5	2.9
778	178.5	X

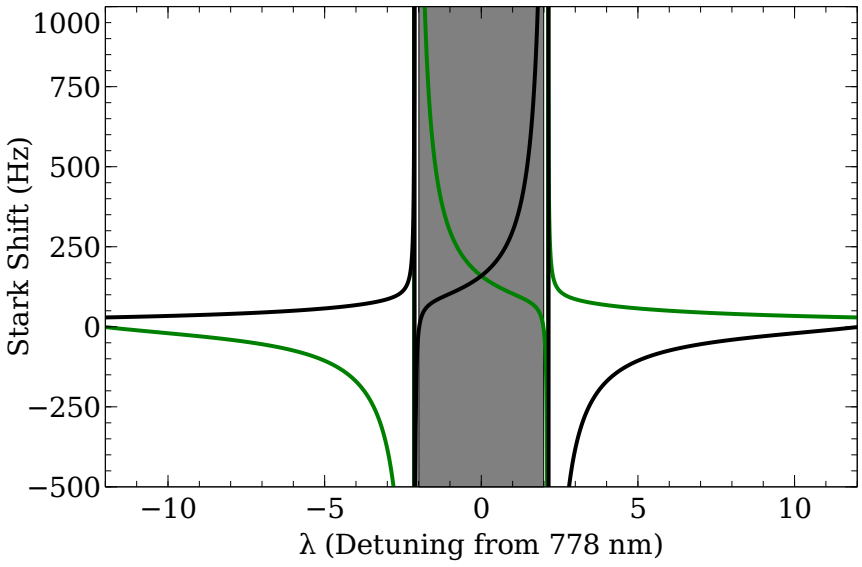

Figure 3.6: Numerical analysis of two-photon excitation with two non-identical frequencies. Shown above is the ac-Stark shift arising from two-photons whose sum is constrained to be on resonance with the $5S_{1/2} \rightarrow 5D_{5/2}$ transition, green and black lines detail the individual ac-Stark shifts from each photon as a function of wavelength detuned from 778 nm. The shaded area is the zone where ac-Stark shift cancellation is not possible.

the atom in a two-color approach described in [57, 106, 107]. In the atomic frame the $\vec{\boldsymbol{k}}$ vectors of the excitation photons no longer match, leading to a velocity dependent Doppler broadened peak. The Doppler broadening is offset by increased excitation (see Figure 3.6). Short term stability has also been shown to remain unchanged in this design, however, clock stability at one day has not yet been measured. Instabilities on longer timescales can often be driven by technical noise, i.e. lock-point errors, reference voltage drifts, detector responsivity drift, etc. Broadening the transition could make control of these noise sources more difficult. An alternative two-color approach introduces a second laser (off-resonance from the virtual and intermediate states) to the degenerate two-photon Doppler-free experiment. The wavelength of this mitigation laser would be chosen such that the differential polarizability sign is opposite that of a 778.1 nm photon. The mitigation laser and the 778.1 nm clock laser

could then be stabilized on a similar photo-detector, with respect to each other, reducing requirements for a stable voltage reference. Unfortunately, frequency drifts in the mitigation laser would cause variations in the ideal ratio, imposing requirements on the frequency stability. Volumetric Bragg grating stabilized lasers developed for Raman spectroscopy experiments [79, 93, 102, 140] offer potential options for mitigation lasers. Table 3.3 displays three possible mitigating wavelengths and calculated shifts. For a system whose purpose is to minimize the required operational power while maintaining high short term clock stability the mitigation laser at 785 nm is the preferred choice. Use of a mitigation laser could ease the challenge of power stabilizing the probe laser. O-RAFS has already demonstrated that clock laser power can be stabilized to 0.1% [92]. We assume that the mitigation laser can also be stabilized to 0.1%. If this assumption is true the variation in stark shift , $\delta\Delta\nu \propto \delta I \alpha_{diff}$, would be suppressed by the subtraction of the differential polarizabilities of the 778.1 nm clock laser and the 785 nm mitigation laser, α_{diff}. If the cancellation can be maintained at a 0.1% level the product is then a 1 ppm stabilization of the ac-Stark shift and an absolute cancellation of the shift to the $< 10^{-13}/\sqrt{\tau}$ level.

Beyond improvements to the stability, future work with this system necessarily involves miniaturizing and hardening the laser and frequency comb for future field deployment. Particular emphasis will need to be paid to automation of the locking electronics and simplification of the control loop architecture, which currently includes 10 independent temperature control segments. Reducing the power consumption of the frequency comb, which currently uses four pump lasers, is another important area of research. Finally, any attempt to prepare this type of advanced optical clock for space will have to overcome the challenge of radiation-induced darkening of optical components. Despite these challenges, a vapor cell optical clock, such as the one described here, could soon be deployed to provide precise timekeeping for extra-laboratory applications.

Chapter 4

Calcium

The long term fractional frequency instability goals for the O-RAFS system of 1×10^{-15} at one day are quite ambitious. Operation at 1×10^{-15} is the practical limit for O-RAFS given the ac-Stark and collisional shift limitations. Divalent atoms such as calcium and strontium possess spectrally narrow, highly-forbidden optical transitions that are attractive for optical frequency standards. The recent development of optical clocks with these species has largely focused on the $^1S_0 \rightarrow {}^3P_0$ transition with a natural linewidth in the mHz regime [88]. The broader $^1S_0 \rightarrow {}^3P_1$ transition is more attractive from a compact clock mindset (see Figure 4.1). Of particular interest is the 657 nm transition in neutral calcium, for which the natural linewidth is just below 400 Hz [32, 75, 82]. In fact, calcium beam clocks in sealed vacuum tubes have made significant progress with instabilities reaching $5.5 \times 10^{-14}/\sqrt{\tau}$ [123] by using a reference cavity and achieving 5×10^{-15} at one second by leveraging Ramsey-Bordé spectroscopy [55]. A great reduction of size could be made if a vapor cell technology were employed. Not only is the linewidth of the clock transition much more narrow than in O-RAFS, but the transition is more resistant to magnetic field, dc-Stark changes and broadening by Helium impurities (Table 4.1). Since all allowed transitions from either the excited or ground states are more energetic than

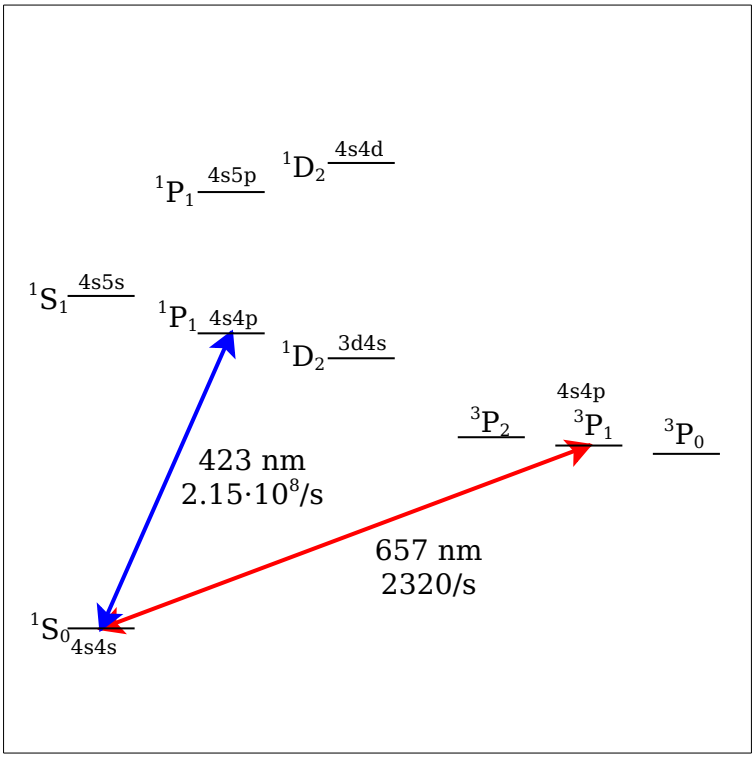

Figure 4.1: Shown above is a partial energy level diagram of calcium. Of particular interestares the $^1S_0 \rightarrow {}^3P_1$ intercombination line and the $^1S_0 \rightarrow {}^1P_1$ cooling transition, which could be utilized to created a cold atom vapor cell clock. Figure generated with data from Ref. [112].

the thermal blackbody radiation at 480 °C ,the BBR shift is easier to calculate and of the same order as in Rb. It is these properties that make calcium an intriguing choice for a vapor cell based clock. However, to achieve similar vapor pressures of the rubidium cells used in Chapters 2 and 3, a calcium vapor cell must be operated at around 480 °C, well outside the operating rage of any standard vacuum systems (see Figure 4.2). Moreover, chemical reactions between typical glasses and alkaline-earth vapors occur rapidly at elevated temperatures, eventually blocking laser transmission.

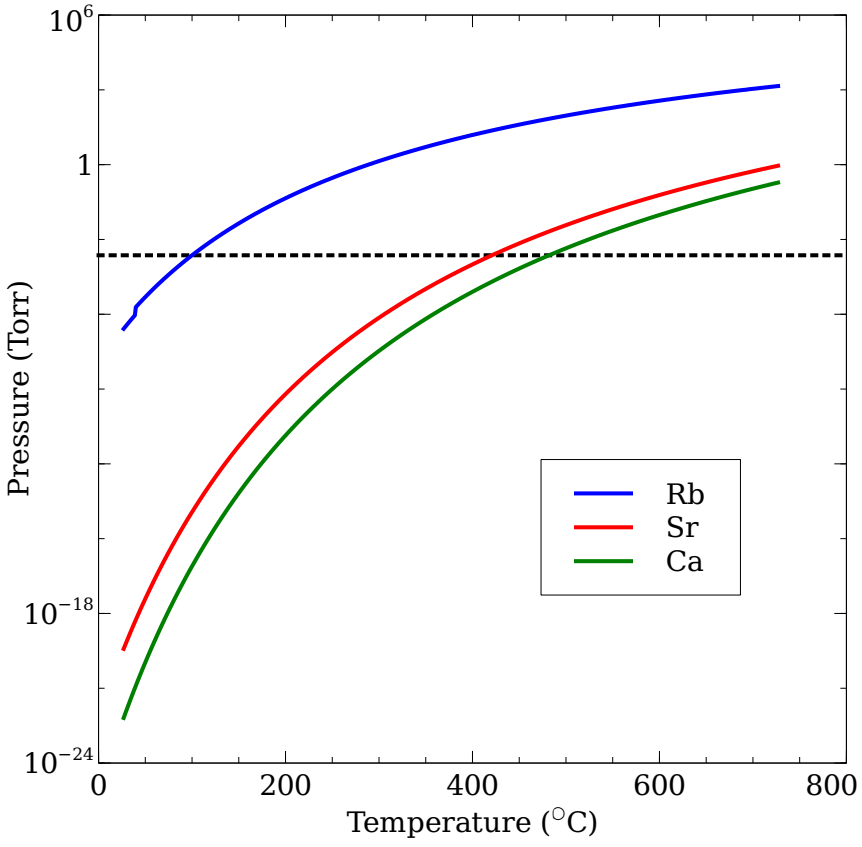

Figure 4.2: The vapor pressure (Torr) of rubidium (blue), strontium (red), and calcium (green) versus temperature (°C). The operating pressure of the O-RAFS system at 100 °C is at the dotted black line. Figure generated with the model presented in Ref. [3].

Crystalline materials have proven far more impervious to reaction, with sapphire and calcium fluoride (CaF_2) showing good results at higher temperatures [48,69,83]. Use of these materials, coupled with a cold finger in the cell, these methods have shown working calcium vapor cells that operate continuously for days. However, after long term operation, either new calcium is introduced or new windows are needed. A vapor cell constructed from Eu:CaF_2 [9] has shown some promise for future calcium vapor cell needs. Recent interest in rubidium resistant windows for the diode pumped alkali laser have shown that ALON, MgF, spinel and cubic zirconia have resistance

Table 4.1: Comparison of environmental shift parameters between the intercombination line in calcium and the two-photon transition in rubidium.

Shift parameter	657 nm line in Ca	two-photon transition in ^{87}Rb
dc-Stark (kHz/(kV/cm)^2)	29.874 [86]	79.4
Magnetic Field (Hz/G^2)	0.006265 [14]	50000
BBR (mHz/K)	-200 [39]	210
He Broadening (kHz/mTorr)	8.24 at 879 K [115]	51.1 at 373 K [146]

to rubidium at high temperature (around 450 °C) for multiple days of exposure [52]. These materials may have some resistance to calcium vapor at elevated temperatures. An attempt to design, build and test a calcium vapor cell is detailed in this chapter.

4.1 Optical Contact Vapor Cells

Frit and diffusion bonding are two common techniques to create vapor cells. Both require that the system undergo extreme temperatures. Usually, optical windows are bonded to a glass tube with a fill tube opening. The cell is evacuated, the alkali metal is deposited and the fill tube is pinched off. Unfortunately, the glass frit material begins to melt around 450 °C [78], which is near the projected operational temperature of an calcium vapor cell. Alternatively, diffusion bonding works by raising the temperature of the glass close to melting while under pressure. The high melting point of CaF_2, 1418 °C, and cubic zirconia, 2750 °C, make diffusion bonding challenging. For these reasons, another method for vapor cell construction was desired and an optical contact bond was chosen.

Two clean optically polished surfaces will bond when brought into intimate contact, a process known as optical contact bonding. Both ionic and van der Waals forces contribute to the bond making a vacuum tight seal. The vapor cells were constructed out of a polished block of crystalline material with a through hole. A

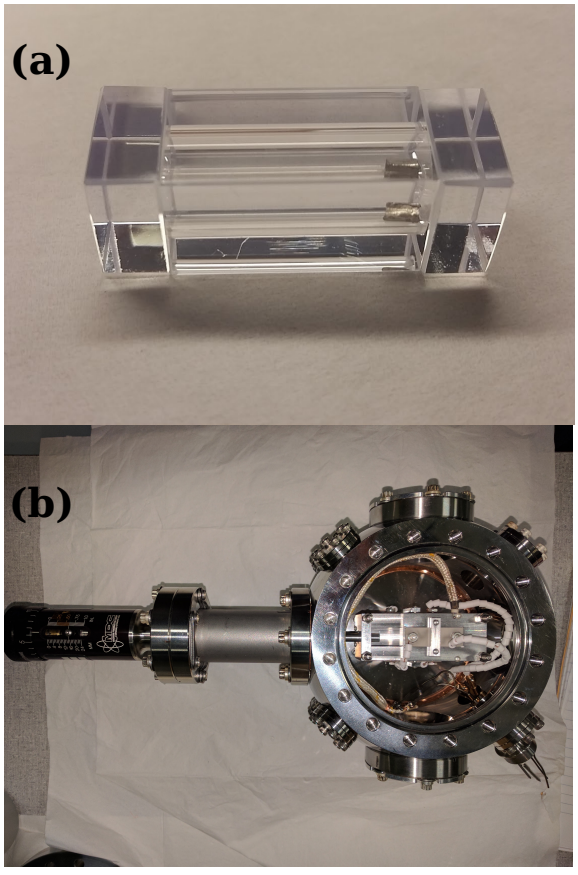

Figure 4.3: Photographs of (a) completed vapor cell and (b) cell bonding and bake out chamber.

base and a lid were then optically contact bonded with a small amount of calcium introduced. However, in order to avoid buffer gas broadening of the narrow calcium transition the final step would need to be done in a high vacuum environment. A chamber was designed so that the cell could be baked out and placed into optical contact under a high vacuum environment (Figure 4.3).

4.2 Heating Package

In order to achieve optically dense vapors on the calcium intercombination line, the vapor cell must reach temperatures 550 °C. Original designs of the vapor cell called for the faces of the optical axis to be completely unrestricted. The original vapor cell itself consists of a 2x1x1 inch Eu:CaF_2 crystal with a 0.75 inch diameter core milled through the long axis. The interior and end are polished and a 1x1x0.25 inch cap is optical-contact bonded to the open face with calcium inside. The calcium vapor cell was surrounded on three sides by thin plates of aluminum nitride (AlN), a material which has a high thermal conductivity and acts as a heat spreader. Heating elements sit in direct contact with each of the AlN plates. The heating elements consist of a tungsten wire potted into an AlN ceramic. These heating elements then rested on plates of high temperature borosilicate glass (thickness 5 mm), which provide electrical insulation of the heating elements exposed connectors. One side of the cell was intentionally left without a heater and heat spreader. This bare crystal material was positioned opposite a vacuum chamber window to provide a cold spot for the calcium to collect away from the vapor cell optical windows. All of these components fit tightly into a four sided copper shroud for structural support. This heating package was then separated from the stainless steel vacuum chamber by a set of four alumina springs, which provide a long thermal pathway.

This approach exposed several obstacles. The most apparent issue was the need for much more input power than desired in a compact device. 85 W of input power was required to reach 570 °C. While this temperature was sufficient to observe laser absorption on the 657 nm clock transition, operation of the cell at these elevated temperatures caused a second complication, namely that optical access quickly diminished. The problem was that the interior vapor call faces were becoming coated with calcium. Thermal analysis concluded that the top of the vapor cell and the windows were competing cold spots allowing for calcium build up in both locations.

By observing the temperature of the vapor cell as it cooled, along with estimates of the heat capacity of the crystal and the thermal resistance of the alumina springs, we determined that heat was primarily lost by radiation from the copper box to the surrounding stainless steel vacuum chamber. Specifically, the relatively short cool down time constant (2-3 hours) suggested a thermal resistance near 150 K/W, while the springs are expected to have a thermal resistance on the order of 3,000 K/W. I then performed simulations utilizing a CAD based finite element thermal modeling software. This program allows the user to develop radiative (using Monte Carlo methods), conductive, and convective heat transfer models for solids and surfaces. For our simulations the following conditions were set. The heating package was tested under a hard vacuum, where convective heat transfer can be ignored. A 6-inch diameter spherical shell with emissivity 0.8 that was regulated to 60 °C was used to simulate the vacuum chamber. Three heaters were placed directly on the sides of the simulated CaF_2 crystal to apply the power necessary to achieve the correct operational temperature in steady state. The modeling showed that only about 1 W of power was dissipated through the alumina springs, while the remaining heat loss was radiative. This conclusion, along with the observation of calcium material buildup at the vapor cell faces, prompted a radiative heat shield design.

The new design again implemented AlN heat spreaders and AlN potted tungsten heaters, but eliminated the borosilicate glass, modified the copper shroud, and added a much needed outer heat shield, for which aluminum was chosen. The calcium vapor cell was surrounded by the AlN heat spreaders on all sides with the exception of a 4 mm hole for optical access on each end face, and a rectangle on the top face enforcing a cold spot far from optical access points. The vapor cell and heat spreaders were enclosed in a copper box with the same 4 mm openings on the faces for optical access and openings on three sides to allow three heaters to contact the heat spreaders. The copper box provides structural support to hold the heaters and aluminum nitride heat spreaders in contact with the crystal. This assembly is then

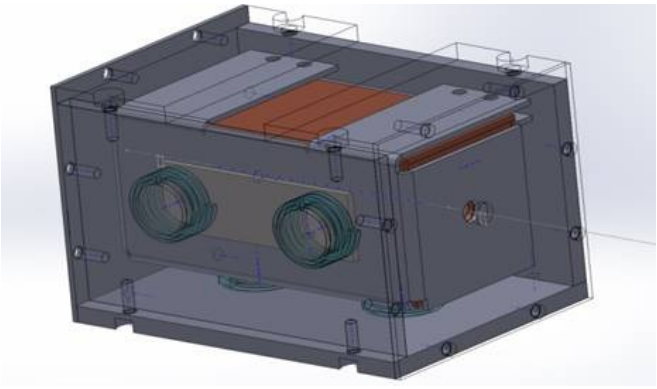

Figure 4.4: A computer animated drawing of the cell heating package with radiation shield design.

suspended in an aluminum box, with corresponding openings for optical access and a rectangular opening on top to create the same top cold spot, by alumina springs. The alumina springs provide a long thermal path to the low emissivity aluminum box. A second set of alumina springs is used to stand off the heating package from the vacuum chamber. Figure 4.4 shows the final radiation shield design used.

This radiative heat shield packaging allowed us to hold the crystal vapor cell at 550 °C with only 36 W of input power, less than half the power required to reach the same temperature in the previous design. Moreover, we did not see calcium metal accumulate at the vapor cell faces, but rather around the top, which indicates the location of the cold spot in the cell. Figure **??** shows the thermal gradients across the cell to be no larger than 4 °C as determined by our simulation. Based on solid angles, we estimate that about 10% of the heat loss is through the laser beam apertures, 17% is through the opening near the top (used for loading calcium sample and evacuation of atmosphere), and just 3% is conducted through the alumina spring standoffs. The majority of thermal losses from both the vapor cell to the heat shield and from the heat shield to the outer vacuum chamber are radiative.

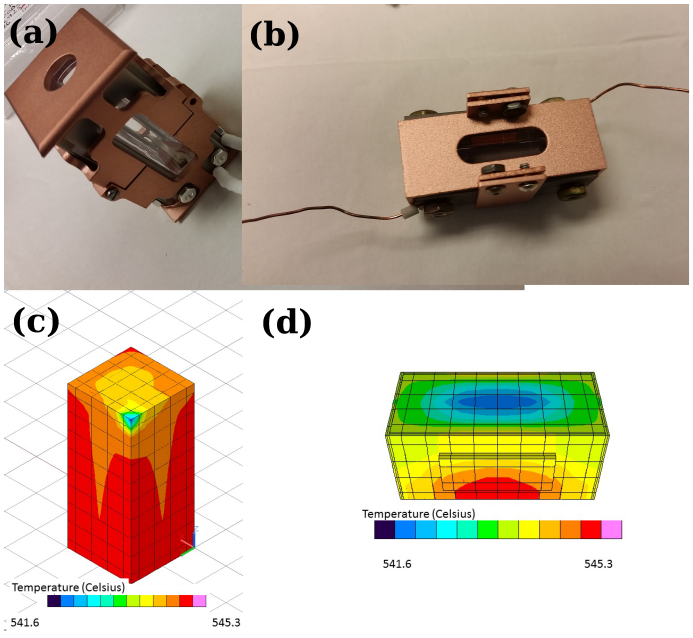

Figure 4.5: Photographs of (a) high optical access cell, (b) spectroscopy cell, (c) high optical access thermal model and the (d) spectroscopy thermal model. Temperature dependence as determined by thermal modeling. Partial figure originally presented in [9].

Finally another heating package was designed with high optical access for potential laser cooling projects. Sapphire slides replaced the AlN heat spreaders and the copper shroud was redesigned. It was also necessary in this design to eliminate the radiative heat shield, (see Figure 4.5 (a) and (c)).

Two methods to suspend the vapor cells in the vacuum chamber were used. Originally, custom aluminum nitride springs were manufactured. The heating package was carefully placed on 4 of these springs. The long thermal path reduced thermal conduction to the steel chamber. However, this design was not mechanically robust. Finally, a decision was made to sacrifice some heating efficiency for mechanical stability. Four threaded tungsten rods were used to suspend the heating package. The package was only in incidental contact with the rods as through holes accepted the rods and the package sat on four tungsten nuts. This suspension method was

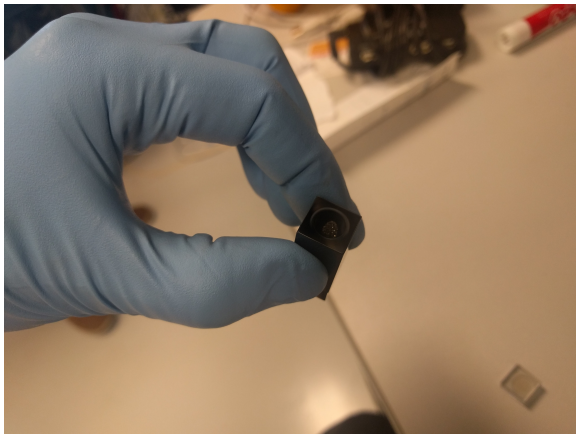

Figure 4.6: A cubic zirconia vapor cell after exposure to elevated temperatures in a vacuum environment.

introduced with little impact on necessary heating power.

4.3 Results and Future Work

To reduce convective heat exchange each heating package was placed under vacuum. The package mount was designed with a large conductive thermal resistance to the vacuum chamber. This served to keep the vacuum chamber temperature within manufacture specifications as well as further reduce required power to heat the vapor cell. At elevated temperatures the major heat leak from the vapor cell occurs through radiative heat transfer. Three vapor cells were constructed and tested: one cubic zirconia cell and two Eu:CaF_2 cells. Although cubic zirconia may be resistant to calcium vapor when placed under vacuum at elevated temperatures cubic zirconia becomes opaque, thereby confirming [73] (see Figure 4.6) and is not useful for the current vapor cell configuration. The first Eu:CaF_2 was slowly exposed to high temperatures with an incident 423 nm laser. The final clock architecture relied on a saturate absorption spectroscopy technique. Initially a 423 nm laser was directed through the

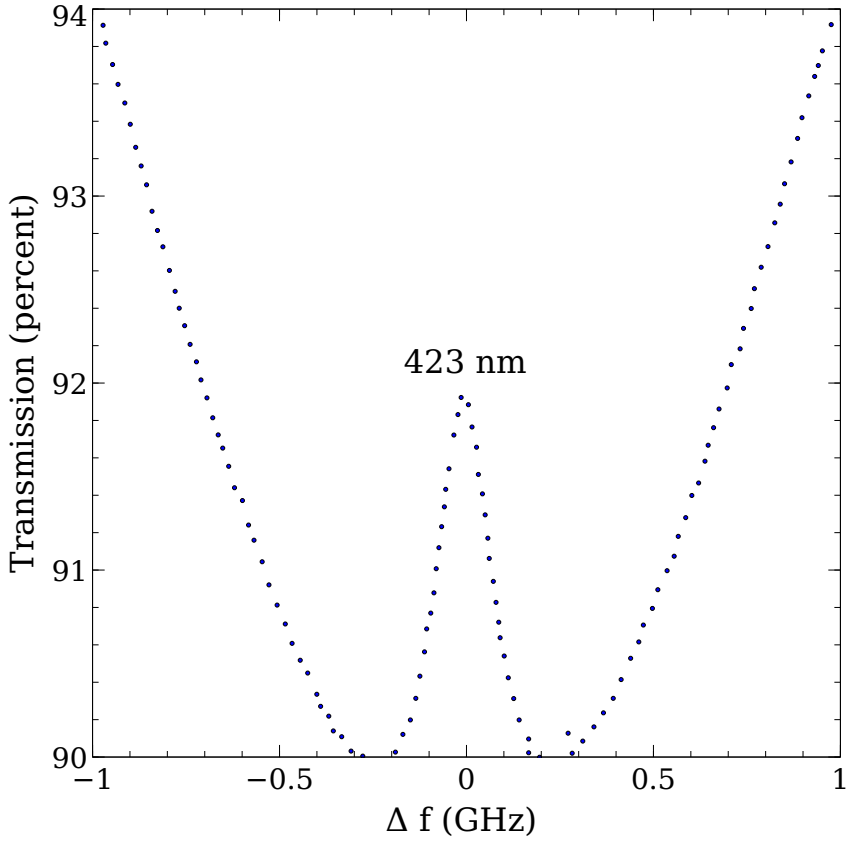

Figure 4.7: A saturated absorption peak of the cooling transition in a calcium vapor cell.

vapor cell and retro-reflected, the ${}^1S_0 \rightarrow {}^1P_1$ transition is easier to measure at lower vapor pressures. The final transmission was measured with a photodiode (see Figure 4.7). The 657 nm clock laser was injected and the temperature was slowly increased in an attempt to secure sufficient densities. Around 650 °C transmission decreased dramatically. The cell was removed and inspected, see Figure 4.8, confirming previously undiscovered literature [6, 23, 24, 51, 53, 63, 105, 110, 127] that show color centers form in Eu:CaF_2 under elevated temperatures in the presence of calcium vapor with absorption peaks around 220 nm, 300 nm, 380 nm and 580 nm. The second Eu:CaF_2 vapor cell was carefully kept under 600 °C and operated continuously until excess calcium clouded the windows (too much calcium was initially introduced), however

Figure 4.8: A Eu:CaF_2 vapor cell after exposure to calcium vapor in vacuum at 650 °C, observe the purple color of the cell, no longer transparent to either the 423 nm cooling or the 657.3 nm clock transition.

during final inspection it was determined that no noticeable color center formation had occurred during the roughly 30 days of continuous operation. However, during operation unexpected fluorescence was observed. A spectrometer was used to determine the origin of the extra contributions (see Figure 4.9). The spectrometer measured the presence of sodium, potassium and rubidium transitions. It appears that the excited calcium vapor transfered energy to the atomic impurities, which would subsequently decay causing the observed fluorescence signal. These impurities are believed to be present in the calcium ingot and would be easily removed for new vapor cell production. An AOM was introduced to quickly shutter the incident beam and a PMT was used as a fluorescence detector. At various temperatures the lifetime of the $^3P_1$ state was measured. The incident laser would be shuttered and the PMT would record the decay of the fluorescence signal. The measured exponential was fit and the decay time as a function of vapor temperature was measured (see Figure 4.9 (b)). The collisional energy transfer between calcium and the impurities resulted in a measured metastable lifetimes four times less than the expected $\sim$400 μs [55].

Although a calcium clock has some distinct advantages over the O-RAFS system described in Chapters 2 and 3 more work is needed to develop a clock based on a calcium vapor cell technology. Any clock reliant on a Eu:CaF_2 vapor cell will need

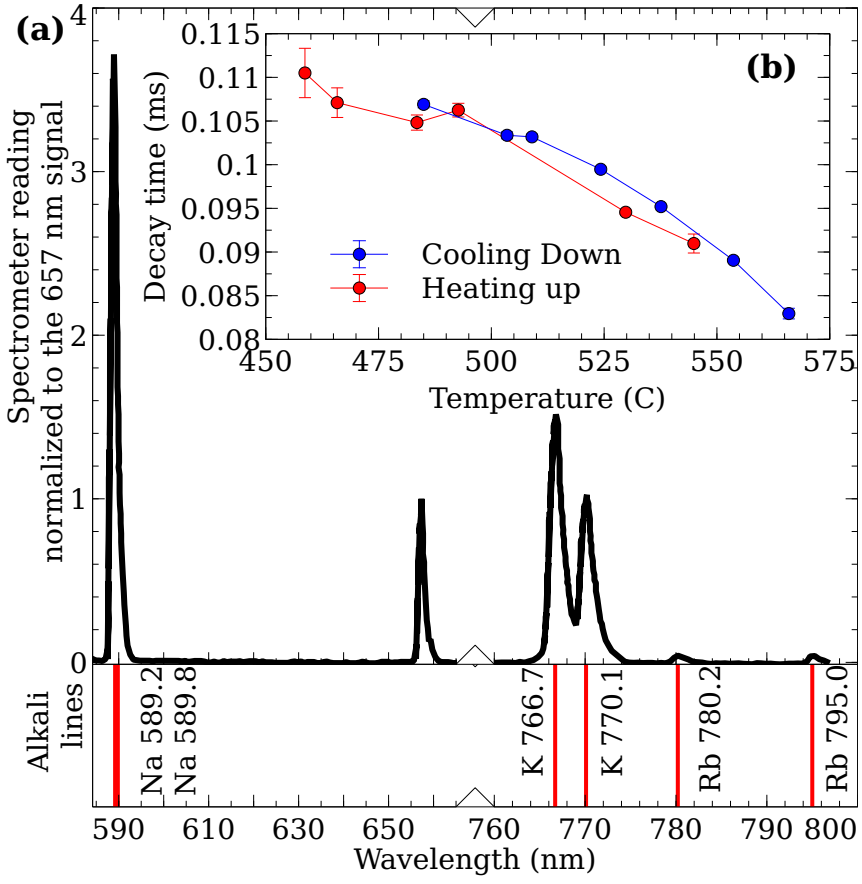

Figure 4.9: Fluorescence was measured with a spectrometer and compared to common transition energies of other alkali and alkali earths (a). The lifetime of the ${}^1S_0 \rightarrow {}^1P_1$ transition was measured to be temperature dependent as well as more than a factor of four less than the expected 400μs (b).

to operate strictly below 600 °C and be properly cleaned and baked out before use to avoid collisional broadening. In addition to exploring vapor cell technologies with Eu:CaF ALON MgF spinel diamond and sapphire show promise for vapor cell materials [52], these materials should be investigated. Unfortunately, to fully measure the Doppler free linewidth of the calcium intercombination line a new laser at 657.3 nm was necessary. Several attempts were made to procure such a laser with no success. More work detailing the collisional broadening and shifts setting a requirement on temperature stability would need to be performed before any prediction of clock in-

stabilities could be made. Moreover, the large radiative thermal transport of the system could make precision temperature control problematic.

Chapter 5

Conclusions

This dissertation has a detailed description of the development of optical frequency standard reliant on a two-photon transition in Rb. This system shows promise for a compact optical frequency standard that could operate in an environment where volume, weight and power are scarce. A compact clock with fractional frequencies of 1×10^{-15} would have similar performance to a Hydrogen maser with reduced size, power requirements, and at, potentially, a reduced cost. Moreover, O-RAFS employs a simple vapor cell clock design and insight into the limitations of the O-RAFS system could yield limitations on vapor cell clocks in general. Of interest is the practical frequency stability limit of vapor cell clocks, particularly at what point more complicated atomic confinement systems are required. The two major environmental influences in O-RAFS arise from ac-Stark effects and Rb-Rb collisional shifts. Ac-Stark shifts originate from the clock laser used to probe the transition while Rb-Rb collisional shifts arise from a temperature dependent vapor pressure driving a variable Rb number density in the vapor cell. "Rb-Rb" type self-collisional shifts ultimately set the floor for any operational hot vapor cell clock as measuring temperature to a higher precision eventually becomes a herculean task. Overcoming the large ac-Stark shift is necessary to measuring the limit of vapor cell clocks.

Ac-Stark shift is currently suppressed simply by stabilizing the laser power. Although this technique has been successful, allowing O-RAFS to reach 4.5×10^{-15} at one day, it has limitations. Measuring laser power precisely is difficult. Photo detector arrays are often non-isotropic, have temperature dependent responsivity curves, and eventual stabilization requires a stable voltage reference. Although counterintuitive, introduction of another laser to mitigate the shift and could ease the power stability requirements. Since the ac-Stark shift is a non-linear function in frequency, many laser frequency/intensity pairs exist whose ac-Stark effect is equal and opposite to the clock laser's. Several candidates have been identified that when introduced would reduce the total ac-Stark shift. Mitigation of the ac-Stark shift could lead to better clock performance as well as investigation into the practical limit of hot vapor cell clocks. Knowledge of this limit, coupled with a few other quick measurements, would in turn put practical performance limits of vapor cell clocks of any atomic species. This limit would clearly define the region where more complicated systems (ion clocks, lattice clocks) become necessary.

For performance beyond classical vapor cell clocks Rb-Rb collisions would need to be suppressed. Currently, the vapor pressure of Rb is non-linear in temperature. This is only true if liquid Rb is present in the vapor cell. Assume that at 100 °C N Rb atoms are in vapor form. If that vapor cell only had N Rb atoms the non-linear behavior of pressure as a function of temperature would be altered. This *starved cell* could be manufactured to explore the BBR magic temperature as well as suppress temperature driven instabilities for clock performances beyond the classical vapor cell limit.

Inclusion of any of: starved vapor cell, the two-color two-photon transition, the Stark shift mitigation laser and/or improved collection efficiency methods could significantly improve O-RAFS stability. With a combination of any of these improvements the two-photon transition in Rb shows promise for a compact clock that can operate at fractional frequencies of 1×10^{-15} at one day. However, operation at

stabilities lower than 1×10^{-15} could prove challenging. Current stability ambitions require operation of the vapor cell temperature with very tight stability, 0.92 mK. Typical platinum RTD devices have a slope of 0.38 $\Omega/°C$ around 100 °C and work by providing a stable current and reading a voltage. To condition temperature precisely to 0.92 mK from a set-point around 100 °C the sensor must be read to within 3.5×10^{-4} Ω, requiring a current source more stable (otherwise the error in provided current would influence the measurement). For a system to reach 1×10^{-16} temperatures stable to 0.092 mK must be achieved, requiring a current stable to better than 1 part 100000. Operation of O-RAFS at 1×10^{-16} is not practical with commercial platinum RTDs. Moreover, the macroscopic nature of the vapor cell allows for fluctuations of an observed temperature sensor driven by heat transfer interactions not represented on the entire clamshell that most likely approach the 10 μK level.

If longer term clcock instability requirements prove to be too demanding another operational version of O-RAFS could serve as a local oscillator to a larger microwave system. The short term limit of O-RAFS is determined by the greater of the shot noise and the intermodulation limit. Current systems are estimated to have short term innermodulation limits of 5×10^{-14} at one second of the RIO laser and 1×10^{-14} for the NP Photonics laser. Increasing the SNR of O-RAFS (at the expense of ac-Stark control) could achieve short term stabilities greatly exceeding current oven controlled crystal oscillators.

This dissertation also examines a calcium vapor cell technology, detailing a specific case where a vapor cell could be manufactured. The intercombination line in calcium provides a narrower transition and thus a more stable clock at one second in the shot noise limit. It also provides an atom that appears to be more resilient to dc-Stark and magnetic field effects. However, to the authors knowledge the Ca-Ca collisional broadening and shift on the ${}^1S_0 \rightarrow {}^3P_1$ has never been measured. It seems unlikely that this shift would be easier to control then the shift in Rb. Maintaining fractional frequency instabilities at the 10^{-16} level would likely require the assistance

of laser cooling. Maintaining a MOT in a vapor cell that must be heated to 480 °C could prove challenging and further investigation would need to be done to determine the proper bake out procedure necessary. Moreover, the lifetime of the vapor cell material could prove to be problematic. I have shown that a Eu:CaF_2 vapor cell can be operated at temperatures under 600 °C without loss of transmission for over a month. However, the diffusive color center creation process predicts the eventual failure of the vapor cell at some unknown time in the future.

Any clock reliant on calcium will most likely have similar disadvantages. Although the Ca-Ca collisional shift has yet to be measured, if the magnitude is close to the Rb-Rb collisonal shift, operation at 1×10^{-16} might still prove too challenging.

Although a clock based on neutral calcium could surpass O-RAFS stability on short time scales, eventually thermal control challenges will define the flicker floor of any vapor cell clock. The manufacture of a clock whose instabilities drastically impprove upon the measured instabilities of the O-RAFS system would most likley require an ensemble of trapped atoms. A interesting choice of such a system could be a $^{88}Sr^{+}$ trapped ion clock. Compared to other trapped clock design, it only requires three lasers and a optical frequency comb. In addition, the required lasers are not in the deep ultra violet a common problem with most traped atoms. In the meantime, small improvements to the O-RAFS system could improve compact clocks for use in extra-laboratory environments in the immediate future.

Appendix A

Rubidium Properties

This section collects the properties of rubidium used throughout the dissertation.

Table A.4 shows values for the reduced electric-dipole matrix elements, $\langle J|d|J'\rangle$,

Table A.1: Frequencies of the hyperfine components of the $5S_{1/2} \rightarrow 5D_{5/2}$ constrained to consider only the $F = 3$ (^{85}Rb) and $F = 2$ (^{87}Rb) ground states as reported by [99].

Hyperfine Component	Relative Intensity [99]	Measured frequency [99]
^{85}Rb		
$F_g = 3 \rightarrow F_e = 5$	$11/36 \approx 30.6\%$	385285142367.0 (8.0) kHz
$F_g = 3 \rightarrow F_e = 4$	$1/6 \approx 16.7\%$	385285147084.9 (8.0) kHz
$F_g = 3 \rightarrow F_e = 3$	$7/90 \approx 7.8\%$	385285151594.8 (8.0) kHz
$F_g = 3 \rightarrow F_e = 2$	$1/36 \approx 2.8\%$	385285155397.6 (8.0) kHz
$F_g = 3 \rightarrow F_e = 1$	$1/180 \approx 0.6\%$	385285158138.0 (13.0) kHz
^{87}Rb		
$F_g = 2 \rightarrow F_e = 4$	$3/8 \approx 37.5\%$	385284566366.3 (8.0) kHz
$F_g = 2 \rightarrow F_e = 3$	$7/40 \approx 17.5\%$	385284580777.8 (8.0) kHz
$F_g = 2 \rightarrow F_e = 2$	$1/16 \approx 6.25\%$	385284592255.2 (8.0) kHz
$F_g = 2 \rightarrow F_e = 1$	$1/80 \approx 1.25\%$	385284600225.2 (8.0) kHz

Table A.2: A partial list of ^{87}Rb properties

Constant	Value	Reference
$g_J(5S_{1/2})$	2.00233113 (20)	[8]
$g_J(5D_{5/2})$	1.1998 (15)	[8]
g_I	-0.0009951414(10)	[8]
Nuclear Spin (I)	3/2	
$5S_{1/2}$ hyperfine structure	6834.6870 (17) MHz	[18]
$5D_{5/2}$ magnetic dipole constant A	-7.4923 (3) MHz	[18]
$5D_{5/2}$ Electric quadrupole constant B	1.2713 (20) MHz	[18]

Table A.3: A partial list of ^{85}Rb properties

Constant	Value	Reference
$g_J(5S_{1/2})$	2.00233113 (20)	
$g_J(5D_{5/2})$	1.1998 (15)	
g_I	-0.0002936400(6)	[8]
Nuclear Spin (I)	5/2	
$5S_{1/2}$ hyperfine structure	3035.7333 (7) MHz	[18]
$5D_{5/2}$ magnetic dipole constant A	-2.1911 (12) MHz	[18]
$5D_{5/2}$ Electric quadrupole constant B	2.6804 (200) MHz	[18]

taken from [118], are presented in a.u., the transition energies are taken from [112], and the Einstein A coefficients are calculated utilizing Equation 2.16, unless referenced to another source where Equation 2.16 was utilized to calculate the reduced-dipole matrix elements. The chosen sign convention yields negative energies for the $5D_{5/2} \rightarrow 5P_{3/2}$ and $5D_{5/2} \rightarrow 6P_{3/2}$ transitions, where the excited, P, state has a lower energy then the ground, $5D_{5/2}$, state

Table A.4

Transition	$\langle J\|d\|J'\rangle$	Energy (cm^{-1})	A_{ki} (MCyc/sec)	Transition	$\langle J\|d\|J'\rangle$	Energy (cm^{-1})	A_{ki} (MCyc/sec)
$5S_{1/2} \rightarrow 5P_{1/2}$	4.233	12578.950	36.129 [a]	$5D_{5/2} \rightarrow 11P_{3/2}$	0.7988 [e]	6415.02	0.085
$5S_{1/2} \rightarrow 5P_{3/2}$	5.979	12816.545	38.117 [b]	$5D_{5/2} \rightarrow 12P_{3/2}$	0.39459 [c]	6734.75 [c]	0.024
$5S_{1/2} \rightarrow 6P_{1/2}$	0.333 [d]	23715.081	1.498	$5D_{5/2} \rightarrow 4F_{5/2}$	6.7789 [e]	1088.62	0.020
$5S_{1/2} \rightarrow 6P_{3/2}$	0.5239 [d]	23792.591	1.873	$5D_{5/2} \rightarrow 5F_{5/2}$	2.5129 [e]	3574.29	0.097
$5S_{1/2} \rightarrow 7P_{1/2}$	0.101 [d]	27835.02	0.223	$5D_{5/2} \rightarrow 6F_{5/2}$	1.3729 [e]	4924.48	0.076
$5S_{1/2} \rightarrow 7P_{3/2}$	0.202 [d]	27870.11	0.447	$5D_{5/2} \rightarrow 7F_{5/2}$	0.871 [e]	5738.23	0.048
$5S_{1/2} \rightarrow 8P_{1/2}$	0.059 [d]	29834.94	0.094	$5D_{5/2} \rightarrow 8F_{5/2}$	0.6411 [e]	6266.12	0.034
$5S_{1/2} \rightarrow 8P_{3/2}$	0.111 [d]	29853.79	0.166	$5D_{5/2} \rightarrow 9F_{5/2}$	0.40389 [c]	6627.71 [c]	0.016
$5D_{5/2} \rightarrow 5P_{3/2}$	1.9994 [d]	−12887	2.89	$5D_{5/2} \rightarrow 4F_{7/2}$	30.316 [e]	1088.59	0.030
$5D_{5/2} \rightarrow 6P_{3/2}$	24.6208 [d]	−1910.91	1.43	$5D_{5/2} \rightarrow 5F_{7/2}$	11.2382 [e]	3574.27	1.46
$5D_{5/2} \rightarrow 7P_{3/2}$	13.8188 [d]	2166.61	0.984	$5D_{5/2} \rightarrow 6F_{7/2}$	6.1398 [e]	4924.46	1.14
$5D_{5/2} \rightarrow 8P_{3/2}$	3.292 [d]	4150.29	0.392	$5D_{5/2} \rightarrow 7F_{7/2}$	3.8953 [e]	5738.22	0.726
$5D_{5/2} \rightarrow 9P_{3/2}$	1.6914 [e]	5266.69	0.212	$5D_{5/2} \rightarrow 8F_{7/2}$	2.8672 [e]	6266.12	0.512
$5D_{5/2} \rightarrow 10P_{3/2}$	1.0989 [e]	5957.66	0.129	$5D_{5/2} \rightarrow 9F_{7/2}$	1.80493 [c]	6627.71 [c]	0.240
$4D_{5/2} \rightarrow 6P_{3/2}$	6.184 [d]	4437.388	1.69	$4D_{3/2} \rightarrow 6P_{3/2}$	2.055 [d]	4436.942	0.19
$5P_{3/2} \rightarrow 6S_{1/2}$	6.013 [d]	7315.965	73.1	$5P_{3/2} \rightarrow 4D_{3/2}$	3.540 [d]	6539.104	1.77
$5P_{1/2} \rightarrow 4D_{3/2}$	7.847 [d]	6776.699	9.7	$5P_{1/2} \rightarrow 6S_{1/2}$	4.119 [d]	7553.56	7.4
$6S_{1/2} \rightarrow 6P_{3/2}$	13.592 [d]	3660.081	4.6				

[a] Lifetime measured in Refs. [61, 125, 139]

[b] Lifetime measured in Refs. [22, 61, 125, 139]

[c] Calcuated using quantum defect theory as described in the text

[d] Matrix element calculated in Ref. [118]

[e] Unpublished results from correspondence email with M. Safronova [116]

Appendix B

Magnetic Field Splitting Calculation

Normally, the atomic energy level shift caused by interaction with a magnetic field is examined in two extreme conditions. The weak magnetic field regime assumes that B is a small perturbation to the fine structure states and ignores mixing of the $|J, m_j\rangle$ states. In the Paschen-Back regime the B field is much larger then the fine structure energy splitting and the Hamiltonian is diagonal in the strong field basis. However, if the magnetic field is of arbitrary strength the incomplete Paschen-Back regime must be examined. This section details a calculation briefly described in the main text where the Hamiltonian was written in the strong field basis and numerically diagonalized.

The Hamiltonian to be diagonalized can be written as,

$$\begin{aligned}
&\boldsymbol{H} = \boldsymbol{H}_{hfs} + \boldsymbol{H}_B^{(hfs)}, \\
&\boldsymbol{H}_{hfs} = A_{hfs}\frac{\boldsymbol{I}\cdot\boldsymbol{J}}{\hbar^2} \\
&+ B_{hfs}\frac{\frac{3}{\hbar^2}(\boldsymbol{I}\cdot\boldsymbol{J})^2 + \frac{3}{2\hbar}(\boldsymbol{I}\cdot\boldsymbol{J}) - J(J+1)I(I+1)}{2I(2I-1)J(2J-1)}, \\
&\boldsymbol{H}_B^{(hfs)} = \mu_B(g_J\boldsymbol{J_z} + g_I\boldsymbol{I_Z})B,
\end{aligned}$$

To calculate $\langle \boldsymbol{H} \rangle$ requires careful expansion of $I \cdot J$ and $(I \cdot J)^2$:

$$\begin{aligned}
I \cdot J =& I_z J_z + I_x J_x + I_y J_y \\
=& I_z J_z + \frac{(I_+ + I_-)(J_+ + J_-)}{4} + \frac{(I_+ - I_-)(J_+ - J_-)}{4} \\
=& I_z J_z + \frac{I_+ J_- + I_- J_+}{2},
\end{aligned}$$

and

$$\begin{aligned}
(I \cdot J)^2 =& (I_z J_z)^2 + \frac{1}{2}[(I_z J_z), (I_+ J_- + I_- J_+)]_+ + \frac{(I_+ J_- + I_- J_+)^2}{4} \\
=& (I_z J_z)^2 + \frac{1}{2}[(I_z J_z), (I_+ J_- + I_- J_+)]_+ + \frac{(I_+ J_-)^2 + (I_- J_+)^2}{4} \\
&+ \frac{(I_+ I_- J_- J_+) + (I_- I_+ J_+ J_-)}{4},
\end{aligned}$$

where the notation $[A, B]_+ = AB + BA$. The raising and lowering operators yield,

$$J_\pm |J, m_J\rangle = \hbar\sqrt{(J \pm m_J + 1)(J \mp m_J)}|J, m_J \pm 1\rangle.$$

We can now calculate the expectation value of the Hamiltonian piece by piece yield-

ing,

$$\begin{aligned}\langle J, m_J; I, m_I|\boldsymbol{H}|J, m_J; I, m_I\rangle &= \mu_B(g_J m_J + g_I m_I)B + A_{hfs} m_I m_J \\ &+ \frac{\frac{3}{2} m_J m_I B_{hfs}}{2I(2I-1)2J(2J-1)} + \frac{3m_J^2 m_I^2 B_{hfs}}{2I(2I-1)2J(2J-1)} \\ &+ \frac{3B_{hfs}}{4}\frac{(J+m_J+1)(J-m_J)(I-m_I+1)(I+m_I)}{2I(2I-1)2J(2J-1)} \\ &+ \frac{3B_{hfs}}{4}\frac{(J-m_J+1)(J+m_J)(I+m_I+1)(I-m_I)}{2I(2I-1)2J(2J-1)} \\ &- \frac{(I+1)(J+1)}{4(2I-1)(2J-1)},\end{aligned}$$

$$\begin{aligned}&\langle J, m_J - 1; I, m_I + 1|\boldsymbol{H}|J, m_J; I, m_I\rangle = \\ &C_1\left[\frac{A_{hfs}}{2} + \frac{3B_{hfs}}{4}\frac{1}{2I(2I-1)2J(2J-1)}\left(4m_I m_J - 2m_I + 2m_J - 1\right)\right],\end{aligned}$$

where, $C_1 = \sqrt{(J-m_J+1)(J+m_J)(I+m_I+1)(I-m_I)}$,

$$\begin{aligned}&\langle J, m_J + 1; I, m_I - 1|\boldsymbol{H}|J, m_J; I, m_I\rangle = \\ &C_2\left[\frac{A_{hfs}}{2} + \frac{3B_{hfs}}{4}\frac{1}{2I(2I-1)2J(2J-1)}\left(4m_I m_J + 2m_I - 2m_J - 1\right)\right],\end{aligned}$$

where, $C_2 = \sqrt{(J+m_J+1)(J-m_J)(I-m_I+1)(I+m_I)}$,

$$\begin{aligned}&\langle J, m_J - 2; I, m_I + 2|\boldsymbol{H}|J, m_J; I, m_I\rangle = \\ &\frac{3B_{hfs}}{4}\frac{C_1\sqrt{(J+m_J+2)(J+m_J-1)(I+m_I+2)(I-m_I-1)}}{2I(2I-1)2J(2J-1)},\end{aligned}$$

and

$$\begin{aligned}&\langle J, m_J - 2; I, m_I + 2|\boldsymbol{H}|J, m_J; I, m_I\rangle = \\ &\frac{3B_{hfs}}{4}\frac{C_2\sqrt{(J+m_J+2)(J-m_J-1)(I-m_I+2)(I+m_I-1)}}{2I(2I-1)2J(2J-1)},\end{aligned}$$

A python script that generates the above Hamiltonian expectation value and numerically diagonalizes it yielding the hyperfine state dependence as a function of magnetic field for the ^{85}Rb $5D_{5/2}$ excited state manifold was used. The code then isolates the F=5 hyperfine level and fits the data to a quadratic function in B.

Appendix C

Ray trace Matrices and extensions

The extended ABCD matrices are presented in [124] to account for optics that are displaced and at an angle w.r.t the optical axis. However, the calculation in Section 2.6.5 relies on the assumption that the resulting ABCD matrix with the included extensions can be used with Gaussian beam propagation.

Consider two arbitrary extended ABCD systems and the resultant multiplication,

$$\begin{pmatrix} A_1 & B_1 & E_1 \\ C_1 & D_1 & F_1 \\ 0 & 0 & 1 \end{pmatrix} \begin{pmatrix} A_2 & B_2 & E_2 \\ C_2 & D_2 & F_2 \\ 0 & 0 & 1 \end{pmatrix}$$

$$= \begin{pmatrix} A_1A_2 + B_1C_2 & A_1B_2 + B_1D_2 & E_1 + A_1E_2 + B_1F_2 \\ A_2C_1 + D_1C_2 & D_1D_2 + C_1B_2 & F_1 + D_1F_2 + C_1E_2 \\ 0 & 0 & 1 \end{pmatrix}.$$

The resultant product has the same ABCD matrix values had the extended matrices not been used. The EF portion of the extended matrix is coordinate transformation after the first system before the entering the new system. Gaussian beam propagation is not dependent on the coordinate system used, allowing for the normal formulation to be leveraged during calculations with the extended matrices.

References

[1] https://www.microsemi.com/product-directory/cesium-frequency-references/4114-csiii-model-4310b.

[2] https://www.microsemi.com/product-directory/cesium-frequency-references/4115-5071a-cesium-primary-frequency-standard.

[3] C. B. Alcock, V. P. Itkin, and M. K. Horrigan. Vapour pressure equations for the metallic elements: 2982500 k. *Canadian Metallurgical Quarterly*, 23(3):309–313, 1984.

[4] D. W. Allan. The statistics of atomic frequency standards. In *Proc. IEEE*, volume 54, pages 221–230, Feb. 1966.

[5] V. O. Altemose. Helium diffusion through glass. *Journal of Applied Physics*, 32(7), 1961.

[6] A. E. Angervaks, A. V. Veniaminov, M. V. Stolyarchuk, V. E. Vasilev, I. Kudryavtseva, P. P. Fedorov, and A. I. Ryskin. Optical study of calcium precipitates in additively colored CaF_2 crystals. *J. Opt. Soc. Am. B*, 35(6):1288–1294, Jun 2018.

[7] AOSense. https://aosense.com/product/external-cavity-diode-lasers-ecdls/.

[8] E. Arimondo, M. Inguscio, and P. Violino. Experimental determinations of the hyperfine structure in the alkali atoms. *Reviews of Modern Physics*, 49, 1977.

[9] J. L. Armstrong, N. D. Lemke, K. W. Martin, and C. J. Erickson. Thermal design of high temperature alkaline-earth vapor cells. *Proc. SPIE*, 9763:976303–976303–4, 2016.

[10] C. Audoin, V. Candelier, and N. Dimarcq. A limit to the frequency stability of passive frequency standards. In *Precision Electromagnetic Measurements, 1990. CPEM '90 Digest., Conference on*, pages 93–, June 1990.

[11] I. Barmes, S. Witte, and Kjeld S. E. Eikema. High-precision spectroscopy with counterpropagating femtosecond pulses. *Phys. Rev. Lett.*, 111:023007, 2013.

[12] K. Beloy, J. A. Sherman, N. D. Lemke, N. Hinkley, C. W. Oates, and A. D. Ludlow. Determination of the $5d6s\ ^3D_1$ state lifetime and blackbody-radiation clock shift in Yb. *Phys. Rev. A*, 86:051404, Nov 2012.

[13] J. E. Bernard, A. A. Madej, L. Marmet, B. G. Whitford, K. J. Siemsen, and S. Cundy. Cs-based frequency measurement of a single, trapped ton transition in the visible region of the spectrum. *Physical Review Letters*, 82(16):3228–3231, 1999.

[14] N. Beverini, E. Maccioni, and F. Strumia. g_j factor of neutral calcium 3P metastable levels. *J. Opt. Soc. Am. B*, 15(8):2206–2209, Aug 1998.

[15] M. S. Bigelow, K. W. Martin, G. Phelps, and N. D. Lemke. A high performance clock laser for two-photon frequency stabilized optical clocks. In *Conference on Lasers and Electro-Optics*, page JW2A.163. Optical Society of America, 2018.

[16] F. Biraben, B. Cagnac, and G. Grynberg. Experimental evidence of two-photon transition without doppler broadening. *Phys. Rev. Lett.*, 32:643–645, Mar 1974.

[17] F. Biraben, B. Cagnac, and G. Grynberg. Déplacement et élargissement de la transition à deux photons 3S-4D dans l'atome de sodium par collision contre des atomes de néon. *J. Physique Lett.*, 36(2):41–43, 1975.

[18] S. Bize, Y. Sortais, M. S. Santos, C. Mandache, A. Clairon, and C. Salomon. High-accuracy measurement of the ^{87}Rb ground-state hyperfine splitting in an atomic fountain. *Europhysics Letters*, 45(5), 1999.

[19] J. E. Bjorkholm and P. F. Liao. Resonant enhancement of two-photon absorption in sodium vapor. *Phys. Rev. Lett.*, 33:128–131, Jul 1974.

[20] N. Bloembergen, M. D. Levenson, and M. M. Salour. Zeeman effect in the two-photon 3S→5S transition in sodium vapor. *Phys. Rev. Lett.*, 32:867–869, Apr 1974.

[21] B. J. Bloom, T. L. Nicholson, J. R. Williams, S. L. Campbell, M. Bishof, X. Zhang, W. Zhang, S. L. Bromley, and J. Ye. An optical lattice clock with accuracy and stability at the 10^{-18} level. *Nature*, 506(7486):71–75, February 2014.

[22] H. M. J. M. Boesten, C. C. Tsai, J. R. Gardner, D. J. Heinzen, and B. Verhaar. Observation of a shape resonance in the collision of two cold ^{87}Rb atoms. *Physical Review A*, 55:636, 1997.

[23] W. Bontinck. Colour centers in synthetic fluorite crystals. *Physica*, 24(6):639 – 649, 1958.

[24] V. N. Borisov, E. V. Barausova, A. V. Veniaminov, A. E. Andervaks, A. S. Shcheulin, and A. I. Ryskin. Dynamics recording of holographics gratings in a photochromic crystal of calcium fluoride. *J. Phys.: Conf. Ser.*, page 012011, 2016.

[25] J. J. Brehm and W. J. Mullin. *Introduction to the Structure of Matter*, volume ISBN 0-471-60531-X. Wiley, 1989.

[26] G. Breit and I. I. Rabi. Measurement of nuclear spin. *Phys. Rev.*, 38, 1931.

[27] A. Brusch, R. Le Targat, X. Baillard, M. Fouche, and P. Lemonde. Hyperpolarizability effects in a sr optical lattice clock. *Physical Review Letters*, 96(10):103003, 2006.

[28] J. H. Burke, N. D. Lemke, G. R. Phelps, and K. W. Martin. A compact, high-performance all optical atomic clock based on telecom lasers. In *Proceedings Volume 9763, Slow Light, Fast Light, and Opto-Atomic Precision Metrology IX*, volume 9763, pages 976304–976304–6, 2016.

[29] B. Cagnac, G. Grynberg, and F. Biraben. Spectroscopie d'absorption multiphotonique sans effet doppler. *J. Phys. France*, 34(10):845–858, 1973.

[30] J. Camparo. The rubidium atomic clock and basic research. *Physics Today*, 60(11), 2007.

[31] H.S. Carslaw and J. C. Jaeger. *Conduction of Heat in Solids*. Oxford, 1954.

[32] A. Celikov, F. Riehle, V.L. Velichansky, and J. Helmcke. Diode laser spectroscopy in a Ca atomic beam. *Optics Communications*, 107(1):54 – 60, 1994.

[33] C. W. Chou, D. B. Hume, J. C. J. Koelemeij, D. J. Wineland, and T. Rosenband. Frequency comparison of two high-accuracy Al^+ optical clocks. *Physical Review Letters*, 104(7):070802, 2010.

[34] H.-S. Chui, M.-S. Ko, Y.-W. Liu, J.-T. Shy, J.-L. Peng, and H. Ahn. Absolute frequency measurement of rubidium 5S–7S two-photon transitions with a femtosecond laser comb. *Opt. Lett.*, 30(8):842–844, Apr 2005.

[35] A. Corney. *Atomic and Laser Spectroscopy*. Clarendon, Oxford, 1977.

[36] S. T. Cundiff and J. (eds.) Ye. *Femtosecond optical frequency combs: Principle, Operation and Applications*. Springer, 2005.

[37] P. J. Davis. *Methods of Numerical Integration*. Academic Press, 2nd edition, 1984.

[38] L. J. De Chant. Analytical solutions for diffusive finite reservoir problems using a modified orthogonal expansion method. *Mathl. Comput. Modellig*, 28(11), 1998.

[39] C. Degenhardt, H. Stoehr, Lisdat C., Wilpers G., H. Schnatz, B. Lipphardt, P. Nazarova, T. ans Pottie, Sterr U., J Helmcke, and F. Riehle. Calcium optical frequency standard with ultracold atoms: Approaching 10^{-15} relative uncertainty. *Physical Review A*, 2005.

[40] A. T. Dellis, V. Shah, E. A. Donley, S. Knappe, and J. Kitching. Low helium permeation cells for atomic microsystems technology. *Opt. Lett.*, 41(12):2775–2778, Jun. 2016.

[41] W. Demtröder. *Laser Spectroscopy*. Springer, 1982.

[42] I. H. Deutsch and P. S. Jessen. Quantum control and measurement of atomic spins in polarization spectroscopy. *Optics Communications*, 283(5):681 – 694, 2010. Quo vadis Quantum Optics?

[43] Dick. Local oscillator induced instabilities in trapped ion frequency standards. *Proceedings of the Nineteenth Annual Precise Time and Time Interval (PTTI) Applications and Planning Meeting*, pages 133–147, 1987.

[44] S. A. Diddams, D. J. Jones, J. Ye, S. T. Cundiff, J. L. Hall, J. K. Ranka, R. S. Windeler, R. Holzwarth, T. Udem, and T. W. Hansch. Direct link between microwave and optical frequencies with a 300 THz femtosecond laser comb. *Physical Review Letters*, 84(22):5102–5105, 2000.

[45] R.W. Ditchburn. *Light*. Academic, New York, 3rd edition, 1976.

[46] F du Burck and O. Lopez. Correction of the distortion in frequency modulation spectroscopy. *Meas. Sci. Technol.*, 15:1327–1336, 2004.

[47] V. A. Dzuba and A. Derevianko. Dynamic polarizabilities and related properties of clock states of the ytterbium atom. *Journal of Physics B - Atomic Molecular and Optical Physics*, 43(7):074011, 2010.

[48] C. J. Erickson, B. Neyenhuis, and D. S. Durfee. High-temperature calcium vapor cell for spectroscopy on the $4s^2\,{}^1s_0 \rightarrow 4\mathrm{s}4\mathrm{p}^3p_1$ intercombination line. *Review of Scientific Instruments*, 76(12), 2005.

[49] K. M. Evenson, J. S. Wells, F. R. Petersen, B. L. Danielson, and G. W. Day. Accurate frequencies of molecular transitions used in laser stabilization: the 3.39m transition in CH_4 and the 9.33 and 10.18m transitions in CO_2. *Applied Physics Letters*, 22(4):192–195, 1973.

[50] J. W. Farley and W. H. Wing. Accurate calculation of dynamic stark shifts and depopulation rates of rydberg energy levels induced by blackbody radiation. hydrogen, helium, and alkali-metal atoms. *Phys. Rev. A*, 1981.

[51] P. Feltham and I. Andrews. Colour centers in alkaline earth fluorides. *phys. stat. sol.*, 10(203), 1965.

[52] A. Fletcher. A study of alkali-resistant materials for use in atomic physics based systems. mathesis, 2017.

[53] F. K. Fong and P. N. Yocom. Crystal growth and color centers of alkaline-earth halides. *The journal of chemical physics*, 41:1383, 1964.

[54] V. Formichella, J. Camparo, and P. Travella. Influence of the ac-Stark shift on GPS atomic clock timekeeping. *Applied Physics Letters*, 2017.

[55] R. W. Fox, J. A. Sherman, W. Douglas, J. B. Olson, A. D. Ludlow, and C. W. Oates. A high stability optical frequency reference based on thermal calcium atoms. In *2012 IEEE International Frequency Control Symposium Proceedings*, pages 1–3, May 2012.

[56] J. Gallagher and G. Peram. Determining the two-photon absorption cross-section for the $5^2S_{1/2} \rightarrow 5^2D_{5/2}$ transition in naturally occurring rubidium. *42nd AIAA Plasmadynamics and Lasers Conference in conjunction with the 18th Internati*, 2011.

[57] V. Gerginov and K. Beloy. Two-photon optical frequency reference with active ac stark shift cancellation. *Phys. Rev. Applied*, 2018.

[58] G. Grynberg and B. Cagnac. Doppler-free multiphotonic spectroscopy. *Reports on Progress in Physics*, 40:791–841, July 1977.

[59] J. Guena, M. Abgrall, D. Rovera, P. Laurent, B. Chupin, M. Lours, G. Santarelli, P. Rosenbusch, M. E. Tobar, R. Li, K. Gibble, A. Clairon, and S. Bize. Progress in atomic fountains at LNE-SYRTE. *IEEE Transactions on Ultrasonics, Ferroelectrics, and Frequency Control*, 59(3):391–409, March 2012.

[60] K. Guo, G. F. Wang, and A. P. Ye. Dipole polarizabilities and magic wavelengths for a Sr and Yb atomic optical lattice clock. *Journal of Physics B - Atomic Molecular and Optical Physics*, 43(13):135004, 2010.

[61] R. F. Gutterres, C. Amiot, A. Fioretti, C. Gabbanini, M. Mazzoni, and O. Dulieu. Determination of the ^{87}Rb 5P state dipole matrix element and radiative lifetime from the photoassociation spectroscopy of the $Rb_0g(P_{3/2})$ long-range state,. *Physical Review A*, 66:024502, 2002.

[62] K. C. Harvey, R. T. Hawkins, G. Meisel, and A. L. Schawlow. Measurement of the stark effect in sodium by two-photon spectroscopy. *Phys. Rev. Lett.*, 34:1073–1076, Apr 1975.

[63] B. Henderson. *Spectroscopy of Solid-State Laser-Type Materials.* Springer, 1987.

[64] R. C. Hilborn. Einstein coefficients, cross sections, f values, dipole moments, and all that. *arXiv:physics/0202029*, 2002.

[65] L. Hilico, R. Felder, D. Touahri, O. Acef, A. Clairon, and F. Biraben. Metrological features of the rubidium two-photon standards of the BNM-LPTF and Kastler Brossel Laboratories. *Eur. Phys. J. AP*, 4(2):219–225, 1998.

[66] I. R. Hill, R. Hobson, W. Bowden, E. M. Bridge, S. Donnellan, E. A. Curtis, and P. Gill. A low maintenance Sr optical lattice clock. In *8th symposium on frequency standards and metrology 2015*, number 012019 in Journal of Physics: Conference Series, 2016.

[67] N. Hinkley, J. A. Sherman, N. B. Phillips, M. Schioppo, N. D. Lemke, K. Beloy, M. Pizzocaro, C. W. Oates, and A. D. Ludlow. An atomic clock with 10^{-18} instability. *Science*, 341(6151):1215–1218, 2013.

[68] R. Holzwarth, T. Udem, T. W. Hansch, J. C. Knight, W. J. Wadsworth, and P. S. J. Russell. Optical frequency synthesizer for precision spectroscopy. *Physical Review Letters*, 85(11):2264–2267, 2000.

[69] M.-S. Huang, M.-H. Lu, and J.-T. Shy. A calcium vapor cell for atomic spectroscopy. *Review of Scientific Instruments*, 73:3747–3749, November 2002.

[70] N. Huntemann, C. Sanner, B. Lipphardt, Chr. Tamm, and E. Peik. Single-ion atomic clock with 3×10^{-18} systematic uncertainty. *Phys. Rev. Lett.*, 116:063001, Feb 2016.

[71] T. W. Hnsch, K. C. Harvey, G. Meisel, and A. L. Schawlow. Two-photon spectroscopy of na 3s-4d without doppler broadening using a cw dye laser. *Optics Communications*, 11(1):50 – 53, 1974.

[72] C. Ishibashi, J. Ye, and J. L. Hall. Analysis/reduction of residual amplitude modulation in phase/frequency modulation by an EOM. In *Quantum Electonics and Laser Science Conference (QELS)*, number QTuF27, 2002.

[73] S. Jeongho, N. Yunyoung, and S. Ohsung. Color evolution in single crystal colored cubic zirconias with annealing atmosphere and temperature. *J. Korean Ceram. Soc*, 53(4):450–455, 2016.

[74] D. J. Jones, S. A. Diddams, J. K. Ranka, A. Stentz, R. S. Windeler, J. L. Hall, and S. T. Cundiff. Carrier-envelope phase control of femtosecond mode-locked lasers and direct optical frequency synthesis. *Science*, 288(5466):635–639, 2000.

[75] P. Kersten, F. Mensing, U. Sterr, and F. Riehle. A transportable optical calcium frequency standarddedicated to J. Helmcke on the occasion of his 60th birthday. *Applied Physics B*, 68(1):27–38, Jan 1999.

[76] W. Ketterle. Atomic and optical physics 1. 2014.

[77] R. Kitamura, L. Pilon, and M. Jonasz. Optical constants of fused quartz from extreme ultraviolet to far infrared at near room temperatures. *Applied Optics*, 46(33):8118–8133, 2007.

[78] R. Knechtel. Glass frit bonding: an universal technology for wafer level encapsulation and packaging. *Microsystem Technologies*, 12:63–68, 2005.

[79] Florian Knorr, Zachary J. Smith, and Sebastian Wachsmann-Hogiu. Development of a time-gated system for raman spectroscopy of biological samples. *Opt. Express*, 18(19):20049–20058, Sep 2010.

[80] M.-S. Ko and Y.-W. Liu. Observation of rubidium $5s_{1/2} \rightarrow 7s_{1/2}$ two-photon transitions with a diode laser. *Opt. Lett.*, 29(15):1799–1801, Aug 2004.

[81] S. B. Koller, J. Grotti, St. Vogt, A. Al-Masoudi, S. Dörscher, S. Häfner, U. Sterr, and Ch. Lisdat. Transportable optical lattice clock with 7×10^{-17} uncertainty. *Phys. Rev. Lett.*, 118:073601, Feb 2017.

[82] Takayuki Kurosu and Atsuo Morinaga. Suppression of the high-frequency recoil component in optical ramsey-fringe spectroscopy. *Phys. Rev. A*, 45:4799–4802, Apr 1992.

[83] J. Lau. *Transparent glass-ceramics and interaction with alkali metal vapours.* phdthesis, 1980.

[84] M. D. Levenson and N. Bloembergen. Observation of two-photon absorption without doppler broadening on the 3S→5S transition in sodium vapor. *Phys. Rev. Lett.*, 32:645–648, Mar 1974.

[85] M. Lezius, T. Wilken, C. Deutsch, M. Giunta, O. Mandel, A. Thaller, V. Schkolnik, M. Schiemangk, A. Dinkelaker, A. Kohfeldt, A. Wicht, M. Krutzik, A. Peters, O. Hellmig, H. Duncker, K. Sengstock, Windpassinger.

P., K. Lampmann, T. Hülsing, T. W. Hänsch, and R. Holzwarth. Space-borne frequency comb metrology. *Optica*, 3(12):1381–1387, Dec 2016.

[86] J. Li and W. A. van Wijngaarden. Stark shift measurement of the $(4s)^{21}s_0 \rightarrow (4s4p)^3p_1$ calcium transition. *Phys. Rev. A*, 1996.

[87] J. Lodewyck, S. Bilicki, E. Bookjans, J.-L. Robyr, C. Shi, G. Vallet, R. Le Targat, D. Nicolodi, Y. Le Coq, J. Guna, M. Abgrall, P. Rosenbusch, and S. Bize. Optical to microwave clock frequency ratios with a nearly continuous strontium optical lattice clock. *Metrologia*, 53(4):1123, 2016.

[88] A. D. Ludlow, T. Zelevinsky, G. K. Campbell, S. Blatt, M. M. Boyd, M. H. G. de Miranda, M. J. Martin, J. W. Thomsen, S. M. Foreman, J. Ye, T. M. Fortier, J. E. Stalnaker, S. A. Diddams, Y. Le Coq, Z. W. Barber, N. Poli, N. D. Lemke, K. M. Beck, and C. W. Oates. Sr lattice clock at 1×10^{-16} fractional uncertainty by remote optical evaluation with a Ca clock. *Science*, 319(5871):1805–1808, 2008.

[89] L. Maleki and J. Prestage. Applications of clocks and frequency standards: from the routine to tests of fundamental models. *Metrologia*, 42(3):S145, 2005.

[90] W. A. Marrison. The evolution of the quartz crystal clock. *Bell System Technical Journal*, 27:510–588, 1948.

[91] W. A. Marrison and J. W. Horton. Precision determination of frequency. In *I. R. E. Proc*, number 2, 1928.

[92] K. W. Martin, G. Phelps, N. D. Lemke, M. S. Bigelow, B. Stuhl, M. Wojcik, M. Holt, I. Coddington, M. W. Bishop, and J. H. Burke. Compact optical atomic clock based on a two-photon transition in rubidium. *Phys. Rev. Applied*, 9:014019, Jan 2018.

[93] P. W. May, J. A. Smith, and K. N. Rosser. 785 nm Raman spectroscopy of CVD diamond films. *Diamond and Related Materials*, 17(2):199–203, 2008.

[94] J. G. McNeff. The global positioning system. *IEEE Transactions on Microwave Theory and Techniques*, 50(3):645–652, Mar 2002.

[95] S. Micalizio, A. Godone, C. Calosso, F. Levi, C. Affolderbach, and F. Gruet. Pulsed optically pumped rubidium clock with high frequency-stability performance. *IEEE Transactions on Ultrasonics, Ferroelectrics, and Frequency Control*, 59(3):457–462, March 2012.

[96] T. Middelmann, S. Falke, C. Lisdat, and U. Sterr. High accuracy correction of blackbody radiation shift in an optical lattice clock. *Phys. Rev. Lett.*, 109:263004, Dec 2012.

[97] P. J. Mohr, B. N. Taylor, and D. B. Newell. Codata recommended values of the fundamental physical constants: 2010. *Journal of Physical and Chemical Reference Data*, 2012.

[98] P. Morzyński, P. Wcisło, P. Ablewski, R. Gartman, W. Gawlik, P. Masłowski, B. Nagórny, F. Ozimek, C. Radzewicz, M. Witkowski, R. Ciuryło, and M. Zawada. Absolute frequency measurement of rubidium 5S→7S two-photon transitions. *Opt. Lett.*, 38(22):4581–4584, Nov 2013.

[99] F. Nez, F. Biraben, R. Felder, and Y. Millerioux. Optical frequency determination of the hyperfine components of the $5S_{1/2} \rightarrow 5D_{5/2}$ two-photon transitions in rubidium. *Optics Communications*, 102:432–438, October 1993.

[100] T. L. Nicholson, S. L. Campbell, R. B. Hutson, G. E. Marti, B. J. Bloom, R. L. McNally, W. Zhang, M. D. Barrett, M. S. Safronova, G. F. Strouse, W. L. Tew, and J. Ye. Systematic evaluation of an atomic clock at 2×10^{-18} total uncertainty. *Nat. Commun.*, 6:6896–, April 2015.

[101] K. Numata, J. Camp, M. A. Krainak, and L. Stolpner. Performance of planar-waveguide external cavity laser for precision measurements. *Opt. Express*, 18(22):22781–22788, Oct 2010.

[102] M. Paillet, F. Meunier, M. Verhaegen, S. Blais-Ouellette, and R. Martel. High performance resonance raman spectroscopy using volume bragg gratings as tunable light filters. *Review of Scientific Instruments*, 81(5):053111, 2010.

[103] T. E. Parker, S. R. Jefferts, T. P. Heavner, and E. A. Donley. Operation of the NIST-F1 caesium fountain primary frequency standard with a maser ensemble, including the impact of frequency transfer noise. *Metrologia*, 42(5):423–430, 2005.

[104] J. Paul, Y. Kaneda, T.-L. Wang, C. Lytle, J. V. Moloney, and R. Jason Jones. Doppler-free spectroscopy of mercury at 253.7 nm using a high-power, frequency-quadrupled, optically pumped external-cavity semiconductor laser. *Opt. Lett.*, 36(1):61–63, Jan 2011.

[105] S. M. Pelka. Examination of color center formation in CaF_2 crystals when exposed to gamma and mixed neutron/gamma fields. mathesis, 2017.

[106] C. Perrella, P. S. Light, J. D. Anstie, F. N. Baynes, F. Benabid, and A. N. Luiten. Two-color rubidium fiber frequency standard. *Opt. Lett.*, 38(12):2122–2124, Jun 2013.

[107] C. Perrella, P. S. Light, J. D. Anstie, T. M. Stace, F. Benabid, and A. N. Luiten. High-resolution two-photon spectroscopy of rubidium within a confined geometry. *Phys. Rev. A*, 2013.

[108] H. E. Peters and H. B. Owings. Hydrogen maser improvements and future applications. In *Proceedings of International Frequency Control Symposium*, 1997.

[109] J. Phelan, T. Dass, G. Freed, J. Rajan, J. D'Agostino, and M. Epstein. GPS block IIR clocks in space: current performance and plans for the future. In *Proceedings of the 2005 IEEE International Frequency Control Symposium and Exposition, 2005.*, 2005.

[110] W. Phillips and R. C. Duncan. Preparation of photochromic calcium fluoride by additive coloration. *Metallurgical Transactions*, 2(3):769–775, Mar 1971.

[111] M. Poulin, C. Latrasse, D. Touahri, and M. Ttu. Frequency stability of an optical frequency standard at 192.6 THz based on a two-photon transition of rubidium atoms. *Optics Communications*, 207(1):233 – 242, 2002.

[112] Y. Ralchenko, A. E. Kramida, J. Reader, and NIST ASD Team. *NIST Atomic Spectra Database (ver. 4.1.0) [Online].* National Institute of Standards and Technology, , 2011. `http://physics.nist.gov/asd`.

[113] W.J. Riley. Handbook of frequency stability analysis. *NIST Special Publication 1065*, 2008.

[114] W. A. Rodgers, R. S. Buritz, and D. Alpert. Diffusion coefficient, solubility, and permeability for helium in glass. *Journal of applied physics*, 25(7):868–875, 1954.

[115] J. Rohe-Hansen and V. Helbig. Pressure broadening of the calcium 657.3 nm line by helium, neon and argon. *J. Phys. B: At. Mol. Opt. Phys.*, 1992.

[116] M. S. Safronova. Email coorespondence with M. S. Safronova.

[117] M. S. Safronova, S. G. Porsev, U. I. Safronova, M. G. Kozlov, and C. W. Clark. Blackbody-radiation shift in the sr optical atomic clock. *Phys. Rev. A*, 87:012509, Jan 2013.

[118] M. S. Safronova, C. J. Williams, and C. W. Clark. Relativistic many-body calculations of electric-dipole matrix elements, lifetimes, and polarizabilities in rubidium. *Phys. Rev. A*, 69:022509, Feb 2004.

[119] J. E. Sansonetti and G. Nave. Wavelengths, transition probabilities, and energy levels for the spectrum of neutral strontium (Sr I). *Journal of Physical and Chemical Reference Data*, 39(3):3449176, 2010.

[120] H. Schnatz, B. Lipphardt, J. Helmcke, F. Riehle, and G. Zinner. First phase-coherent frequency measurement of visible radiation. *Phys. Rev. Lett.*, 76:18–21, Jan 1996.

[121] T. Schuldt, K. Döringshoff, E. V. Kovalchuk, A. Keetman, J. Pahl, A. Peters, and C. Braxmaier. Development of a compact optical absolute frequency reference for space with 10^{-15} instability. *Appl. Opt.*, 56(4):1101–1106, Feb 2017.

[122] C. Schwob, L. Jozefowski, B. de Beauvoir, L. Hilico, F. Nez, L. Julien, F. Biraben, O. Acef, J.-J. Zondy, and A. Clairon. Erratum: Optical frequency measurement of the $2S-12D$ transitions in hydrogen and deuterium: Rydberg constant and lamb shift determinations [phys. rev. lett. 82, 4960 (1999)]. *Phys. Rev. Lett.*, 86:4193–4193, Apr 2001.

[123] H. Shang, X. Zhang, Zhang S., Pan D., H. Chen, and J. Chen. Miniaturized calcium beam optical frequency standard using fully-sealed vacuum tube with 10^{-15} instability. *Optics Express*, 2017.

[124] A. E. Siegman. *Lasers*. University Science Books, 1986.

[125] J. E. Simsarian, L. A. Orozco, G. D. Sprouse, and J.W. Z. Zhao. Lifetime measurements of the 7p levels of atomic francium. *Physical Review A*, 57:2448, 1998.

[126] L. C. Sinclair, J.-D. Deschnes, L. Sonderhouse, W. C. Swann, I. H. Khader, E. Baumann, N. R. Newbury, and I. Coddington. Invited article: A compact optically coherent fiber frequency comb. *Review of Scientific Instruments*, 86(8), 2015.

[127] A. Smakula. Color centers in calcium flouride crystals. Technical report, Massachusetts Institute of Technology, 1954.

[128] J. J. Snyder. Paraxial ray analysis of a cat's-eye retroreflector. *Appl. Opt.*, 1975.

[129] C. Spiegelberg, J. Geng, Y. Hu, T. Luo, Y. Kaneda, J. Wang, W. Li, M. Brutsch, S. Hocde, M. Chen, J. Babico, K. Barry, W. Eaton, M. Blake, D. Eigen, I. Song, and S. Jiang. Compact 100 mw fiber laser with 2 khz linewidth. In *OFC 2003 Optical Fiber Communications Conference, 2003.*, 2003.

[130] Daniel A. Steck. *Quantum and Atom Optics*. 0.10.1 edition, April 2015. revision 0.10.1.

[131] P. G. Suchoski, T. K. Findakly, and F. J. Leonberger. Low-loss high-extinction polarizers fabricated in $LiNbO_3$ by proton exchange. *Optics Letters*, 13(2):172–174, February 1988.

[132] D. B. Sullivan. Time and frequency measurement at NIST: The first 100 years. In *2001 IFFF International Frequency Control Symposium*, pages 4–17, 2001.

[133] D. E. Swets, R. W. Lee, and R. C. Frank. Diffusion coefficients of helium in fused quartz. *The journal of chemical physics*, 34(1), 1961.

[134] G. W. Swift. Thermoacoustic engines and refrigerators: A short course. In *Joint 137th Meeting of Acoustical Societies of America and Europe*, 1999.

[135] B. Taylor and A. Thompson. *NIST Special Publication 330*. NIST, 2008.

[136] D. Tregubov, S. Snigirev, A. Golovizin, S. Pyatchenkov, D. Sukachev, A. Akimov, V. Sorokin, and N. Kolachevskyv. Measurement of the 5D level polarizabilities in laser cooled Rb atoms. *Journal of Physics : Conference Series*, 635(9), 2015.

[137] T. Udem, A. Huber, B. Gross, J. Reichert, M. Prevedelli, M. Weitz, and T. W. Hänsch. Phase-coherent measurement of the hydrogen $1S - 2S$ transition frequency with an optical frequency interval divider chain. *Phys. Rev. Lett.*, 79:2646–2649, Oct 1997.

[138] S. Uetake, K. Hayasaka, and M. Watanabe. Saturation spectroscopy of potassium for frequency stabilization of violet diode lasers. *Japanese Journal of Applied Physics*, 42(3B):L332, 2003.

[139] U. Volz and H. Schmoranzer. Precision lifetime measurements on alkali atoms and on helium by beam-gas-laser spectroscopy. *Physica Scripta*, T65:48, 1996.

[140] N. Vorobiev, L. Glebov, and V. Smirnov. Single-frequency-mode q-switched nd:yag and er:glass lasers controlled by volume bragg gratings. *Opt. Express*, 16(12):9199–9204, Jun 2008.

[141] N. C. Wong and J. L. Hall. Servo control of amplitude modulation in frequency-modulation spectroscopy demonstration of shot-noise-limited detection. *J. Opt. Soc. Am. B*, 1985.

[142] R. Wynands and S. Weyers. Atomic fountain clocks. *Metrologia*, 42:S64, 2005.

[143] D. C. Yost, A. Matveev, E. Peters, A. Beyer, T. W. Hänsch, and Th. Udem. Quantum interference in two-photon frequency-comb spectroscopy. *Phys. Rev. A*, 90:012512, Jul 2014.

[144] A. T. Young. Temperature effects in photomultipliers and astronomical photometry. *Applied Optics*, 2:51, 1963.

[145] Y. Yu, Y. Wang, and J. R. Pratt. Active cancellation of residual amplitude modulation in a frequency-modulation based fabry-perot interferometer. *Review of Scientific Instruments*, 87(3):033101, 2016.

[146] N. D. Zameroski, G. D. Hager, C. J. Erickson, and J. H. Burke. Pressure broadening and frequency shift of the $5S_{1/2} \rightarrow 5D_{5/2}$ and $5S_{1/2} \rightarrow 7S_{1/2}$ two photon transitions in ^{85}Rb by the noble gases and n_2. *Journal of Physics B: Atomic, Molecular and Optical Physics*, 47(22):225205, 2014.

[147] W. Zhang, M. J. Martin, C. Benko, J. L. Hall, J. Ye, C. Hagemann, T. Legero, U. Sterr, F. Riehle, G. D. Cole, and M. Aspelmeyer. Reduction of residual amplitude modulation to 1×10^{-6} for frequency modulation and laser stabilization. *Opt. Lett.*, 39(7):1980–1983, Apr 2014.